Molecular Regulatory Mechanism of Human Myosin-7a

Doctoral (PhD) Dissertation

Alexandra Holló

Supervisors:

András M. Kengyel

James R. Sellers

University of Pécs
Medical School
Department of Biophysics

Pécs

2024

Interdisciplinary Medical Sciences: D93
The Leader of the Doctoral School: Dr. Ferenc Gallyas

Doctoral Program: B-130
Investigating functional protein dynamics using biophysical methods
Program leader: Dr. Miklós Nyitrai

Supervisors: Dr. András M. Kengyel
Dr. James R. Sellers

Table of Contents

List of abbreviations

ADP	Adenosine Diphosphate
ATP	Adenosine Triphosphate
BSA	Bovine Serum Albumin
CALML4	Calmodulin-Like 4 Protein
CaM	Calmodulin
CLP	Calmodulin-like protein
CMV	Cytomegalovirus
DNA	Deoxy Ribonucleic Acid
DTT	Dithiothreitol
EGTA	Egtazic Acid
ELC	Essential Light Chain
FBS	Fetal Bovine Serum
FERM	band 4.1, ezrin, radexin, moesin
GFP	Green Fluorescent Protein
HMM	Heavy Meromyosin
HSP90	Heat Shock Protein 90
IAD	Iodoacetamide
IHC	Inner Hair Cell
IMAC	Intermicrovillar Adhesion Complex
ITC	Isothermal Titration Calorimetry
IVMA	*In Vitro* Motility Assay
LC-MS/MS	Liquid Chromatography with tandem Mass Spectrometry
M7a	Myosin-7a
M7b	Myosin-7b
MET	Mechanoelectrical Transduction
MP	Mass Photometry
MST	MicroScale Thermophoresis

MyBD	Myosin-Binding Domain
MyRIP	Myosin and Rab Interacting Protein
MyTH4	Myosin Tail Homology 4
NADH	Nicotinamide Adenine Dinucleotide
NC	Nitrocellulose
OHC	Outer Hair Cell
PAGE	Polyacrylamide Gel Electrophoresis
PBS	Phosphate-Buffered Saline
PEG	Polyethylene Glycol
RLC	Regulatory Light Chain
S1	Subfragment 1
SAH	Single Alfa Helix
SDS	Sodium Dodecyl Sulfate
SH3	Src-Homology
TEV	Tobacco Etch Virus
TIRFM	Total Internal Reflection Fluorescence Microscopy

1 Abstract

Human myosin-7a is an actin-based motor protein essential for vision and hearing. It plays a vital role in the development and functionality of actin-rich stereocilia. Previous studies using the *Drosophila* homolog demonstrated that myosin-7a is a monomeric, high duty ratio motor, capable of processive movement upon dimerization. However, the characterization of full-length mammalian myosin-7a has been challenging due to difficulties in expressing and purifying a stable, intact protein.

Here, we report the production of a full-length human myosin-7a holoenzyme in insect cells and study its regulation by intra- and intermolecular mechanisms. Human myosin-7a was found to utilize the regulatory light chain, calmodulin, and calmodulin like protein 4 (CALML4) as light chain subunits. CALML4 was recently discovered to be highly enriched in stereocilia and identified as a candidate gene for deafness. Our research indicates that CALML4 is a crucial factor in regulating the dynamic binding of calmodulin to myosin-7a in response to Ca^{2+} signaling. In the cochlea, there are two splicing isoforms of myosin-7a that are differing by a short N-terminal extension only. Using *in vitro* motility assays and biochemistry, we demonstrate that the N-terminal extension has significant effects on the mechanical and enzymatic behaviors of mammalian myosin-7a. The regulation of mechanosensitivity in hair cells is proposed to be achieved through the adjustment of expression levels of the two isoforms of myosin-7a. Our experiments using single molecule motility assays show that *in vitro*, full-length myosin-7a does not display processive movements on actin alone. However, in the presence of MyRIP (a known myosin-7a binding protein in the neuroretina), it exhibits processive movements. The motor-adaptor complex moves slowly along actin filaments and has a prolonged actin attachment time.

Our results suggests that there is a complex network of regulatory mechanisms that are working in synchrony to fine-tune the activity, structure, localization, oligomeric state, and function of myosin-7a. Our work also contributes to the understanding of retinal cell and inner hair cell function at the molecular level.

2 Introduction

Life is based on movement. In living organisms most forms of cellular movement are driven by molecular motors called motor proteins. Motor proteins are involved in various cellular functions, including powering cell division, facilitating cell locomotion and transporting cargo. Eukaryotic cells contain many distinct types of cytoplasmic motor proteins, such as myosins, dyneins, and kinesins, performing critical tasks that are essential to the organism's proper functioning [1].

These motor proteins exhibit variability in the type of filament they can bind to, which may either be actin or microtubule, their direction of movement, and the cargo they can transport. However, they employ the same mechanisms to convert chemical energy into mechanical work through ATP hydrolysis [1, 2].

2.1 Myosins

Myosins constitute a large superfamily of actin-based motor proteins (**Figure 1**). They are essential to various types of cellular movement, such as cytokinesis, phagocytosis, organelle trafficking, and maintaining cell shape. Additionally, they also play a vital role in signal transduction, cell polarization, and transcriptional regulation [3, 4]. In humans, 39 myosin genes have been identified which are classified into 12 classes based on their motor and tail conformation [4, 5].

Members of the myosin superfamily comprise multiple subunits, including heavy chains and light chains. The heavy chains are usually made up of three functional domains (**Figure 2**). The holoenzyme forms when the light chains non-covalently bind to the heavy chain.

The *motor* or *head* domain interacts with the actin filament and binds and hydrolyzes ATP. The motor region's central sequence is conserved in all myosin classes but has some surface loops with varying amino acid sequences and lengths. The

N-terminal extensions also vary in length and provide the foundation for class-specific properties like membrane binding or kinase activity [4].

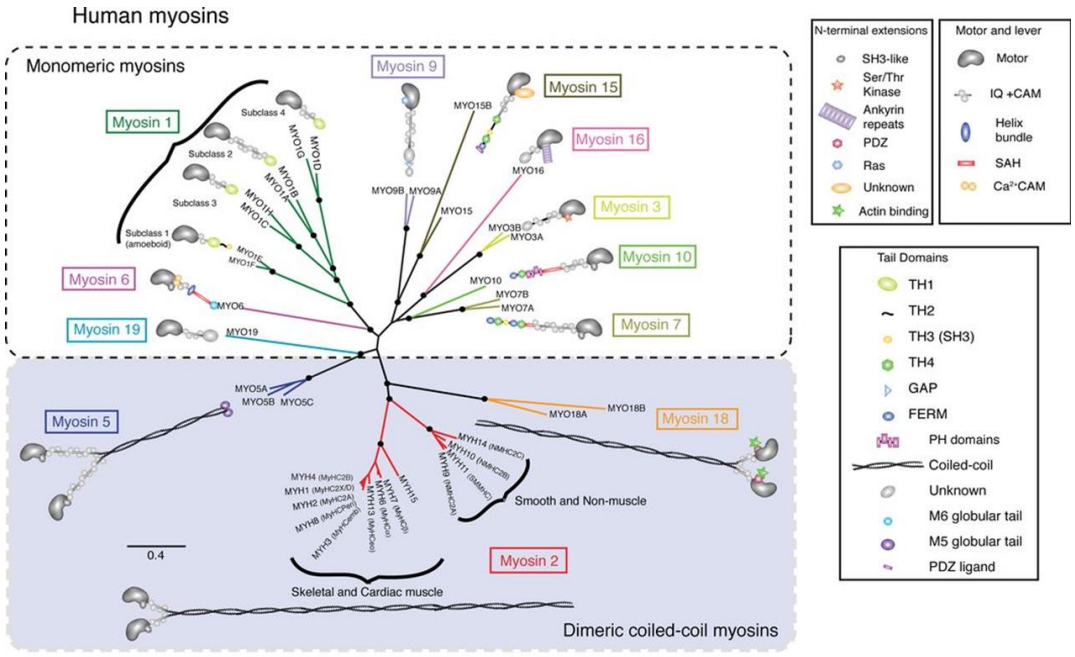

Figure 1. *Family tree of human myosins. Modified from [5].*

The *neck* domain usually contains one or more IQ motifs, which have a consensus sequence (IQxxxRGxxxR) and is responsible for binding to the light chain. The length of the neck region correlates with the number of light chains attached to the heavy chain and together serve as a stiff lever arm that propels actin during the powerstroke. The number of IQ motifs determines the length of the lever arm and consequently the myosin step size. The various myosin classes exhibit varying quantities of IQ motifs, with some myosin classes displaying no IQ motifs at all [4, 6].

Figure 2. *Basic structure of the myosin heavy chain: a motor domain which comprises the ATP binding site and an actin binding region, a light chain binding neck region containing multiple IQ-motifs, and a tail region.*

The *tail* domains exhibit the greatest diversity amongst the myosin domains. They may manifest distinct sequence and length characteristics across different myosin families.

Tail domains of certain myosin classes contain coiled-coil-forming sequences, which are essential for dimerization of two heavy chains in a myosin molecule. Myosins that can dimerize and form filaments through their coiled coil region are called conventional myosins. The first motor protein to be identified was skeletal muscle myosin, later denoted as myosin-2. Subsequently, several other class 2 myosins were identified in heart and smooth muscle as well as in non-muscle cells [2, 7]. Although Myosin-5 has a short coiled-coil region and can dimerize, it is incapable of forming filaments.

Unconventional myosins, in contrast to conventional myosins, cannot form filaments, and instead are functional as monomers or dimers. Unconventional myosins move towards the (+) end of actin filaments similar to conventional myosins, with the exception of myosin VI, which moves towards the (-) end [8]. The tail domains of unconventional myosins anchor and position the motor domain to enable interaction with actin filaments. Specific tail domains are also involved in cargo binding. The most common interaction motifs found in unconventional myosins are SH3-like-, PDZ-, PH-, GAP-, and FERM-domains [6, 9, 10].

The stability of the myosin holoenzyme relies on myosin light chains, which stabilize the neck domain and enable it to serve as a stiff lever arm essential for powerstroke generation. These light chains may also have a regulatory impact on the mechanoenzymatic activity of myosin [11, 12]. Early studies of myosin suggested that conventional myosins bind essential light chain (ELC) and regulatory light chain (RLC), while unconventional myosins bind calmodulin (CaM) as a light chain subunit. However, more recent research has disproved this view. Various studies have shown that multiple light chain types can co-purify with a given heavy chain, but the native composition of light chains may differ. Aside from these examples, other proteins with the EF hand motif – a common calcium-binding pattern – could serve as myosin light chains. This includes calmodulin-like proteins [11, 12].

Although the myosin isoforms have distinct structural differences, they still share a common ATPase mechanism (**Figure 3**) [13]. Nevertheless, kinetic analyses revealed differences in the rates and equilibrium constants of the kinetic steps among each myosin (**Table 1**) [14]. Additionally, it is worth mentioning that some myosins, specifically those in class 18 and 20, are pseudo enzymes and lack ATPase activity [13, 15, 16].

In the absence of ATP, the myosin head tightly binds to the actin filament in a rigor state where the lever arm is in the post-powerstroke position. Subsequently, the presence of ATP disrupts the actin binding site, reducing the bond strength between the myosin head and the actin filament and thereby causing detachment of the myosin head from the actin. The myosin head hydrolyzes ATP into ADP and inorganic phosphate, resulting in a conformational change positioning the lever arm into the pre-powerstroke state, allowing for the rebind of the actin filament. The release of the inorganic phosphate from the ATP binding pocket facilitates the formation of the strong binding state between actin and myosin. The release of ADP causes the lever arm to perform its powerstroke, leading to the forward movement of the tightly bound actin filament. The rigor state is restored and the cycle continues through the binding of another ATP molecule to the nucleotide binding domain [13, 17, 18].

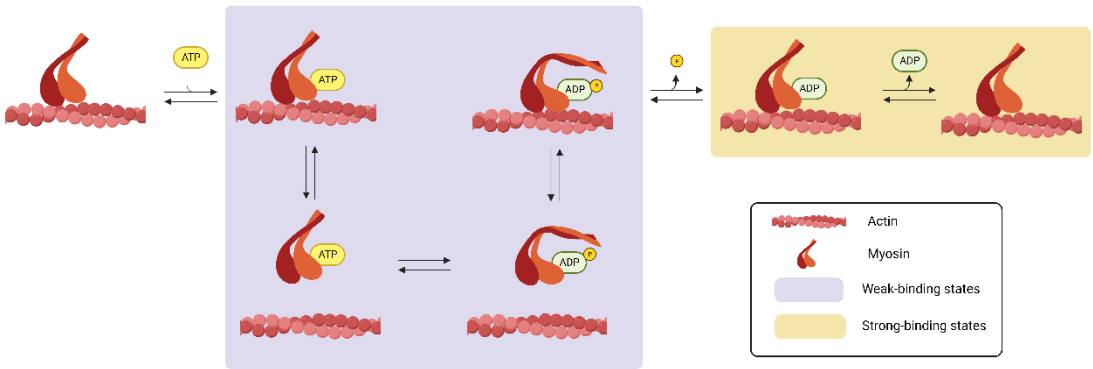

***Figure 3**. The actomyosin ATPase cycle. Different myosin motors spend different amount of time in the weak and strong binding states. Figure based on [13]. Made with BioRender.*

The slowest step in a reaction, known as the rate-limiting step, determines the overall reaction rate. Several steps in the actomyosin ATPase cycle can be rate-limiting,

including ATP binding, ADP and Pi dissociation, ATP hydrolysis, or myosin head dissociation from the actin filament [19].

Class		**Duty ratio**	**Rate limiting step**	**Velocity (µm/s)**	**Directionality**
I	Myosin-1a	0.05	P_i release	0.05 , 0.1	Plus
II	Skeletal muscle	0.038 0.05	P_i release	6.6, 6.9	Plus
	Smooth muscle	0.04	P_i release	0.58	Plus
	Non-muscle myosin-2a	0.05	P_i release	0.3	Plus
	Non-muscle myosin-2b	0.4	ADP release , P_i release	0.092	Plus
III	Myosin-3	N/A	N/A	0.11	Plus
V	Myosin-5a	0.7	ADP release	0.311	Plus
	Myosin-5b	0.79	ADP release	0.22	Plus
VI	Myosin-6 (monomer)	0.8	ADP release	0.058, 0.131	Minus
	Myosin-6 (dimer)		ADP release	0.4, 0.307	
VII	Myosin-7a	0.9	ADP release	0.16, 0.19	Plus
	Myosin-7b	0.8	ADP release		
IX	Myosin-9b	1	ATP hydrolysis	0.015, 0.038, 0.08, 1.1	Plus
X	Myosin-10	0.16, 0.6	N/A	0.3	Plus

Table 1*. The mechanochemical characteristics of myosin classes differ substantially. N/A not available. Table is based on [14].*

The duty ratio of a myosin describes the duration of time that the motor domain tightly binds actin during the ATPase cycle. It can be determined by calculating the rate and equilibrium constants of the individual steps and their percentages in the kinetic cycle. In its weakly bound conformation, myosin is attached to ATP or ADP-P_i, while ADP or nucleotide free states enable a strong attachment to actin. Duty ratio varies greatly

among myosins and significantly affects their cellular function (**Table 1**) [14]. Dimeric myosins having a duty ratio over 0.5 (i.e., the myosin head spends more than 50% of its kinetic cycle in the strong actin binding state) are called processive motors. Such motors can remain bound to actin with at least one head for multiple cycles and are primarily employed in cargo transportation (e.g., myosin-5).

The velocity of actin filament translocation or the speed of a single myosin traveling along a fixed actin filament can be measured through the use of motility assays. For long distance transportation of cytoplasmic cargo, a fast and highly processive motor is the most suitable. Conversely, slow myosins can serve as cellular anchors to tether components in place and provide substructure [14].

Actin filaments are inherently polarized, with a barbed (plus) end that grows rapidly and a pointed (minus) end that grows slowly. Accordingly, the direction of myosin motion on actin has significant functional implications. To date, the majority of identified myosins are motors directed towards the plus end (**Table 1**) [14].

2.1.1 Regulation of myosins

Myosins require stringent control due to their vast diversity and the multitude of cell types where they are expressed. To regulate its activity, conformation, intercellular localization, oligomeric state, and overall function, various mechanisms are employed [11, 20].

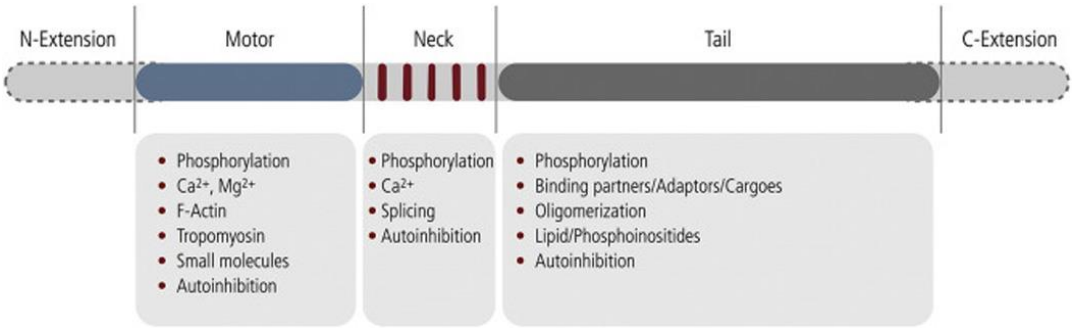

***Figure 4**. Different regulatory mechanism targeting all three domains of the myosin heavy chain. Figure is from [11].*

Myosins are regulated at several levels (**Figure 4**). At the transcriptional level, alternative splicing produces a variety of spliced variants that possess distinct characteristics, intracellular localizations, and cell/tissue-specific functions.

At the post-translational level, kinases and phosphatases perform phosphorylation and dephosphorylation, which are allosteric regulatory mechanisms. Both heavy chains and associated light chains can undergo reversible modifications, with several phosphorylation sites [11, 12, 20].

In many myosins, isoform splicing controls the presence or absence of an N-terminal extension. These extensions vary in size and functions. Some contain certain distinct motifs like PDZ-domain, kinase-domain, ankyrin-motifs or ATP-insensitive actin-binding sites. The extension could influence actin or nucleotide binding, protein-protein interactions, hydrolytic product dissociation, or lever arm movement/rotation [11, 12, 20].

Many monomeric myosins adopt a tightly folded conformation, leading to low actin-activated ATPase activity and affinity. This autoinhibitory state can be relieved e.g., by binding partners, phosphorylation, or cations. Divalent cations, such as Ca^{2+} and Mg^{2+}, affect myosin function in several ways, including conformational changes in the holoenzyme and alterations in motor activity. Myosin light chains have different EF hand domains that can bind cations, and regulation of the holoenzyme is achieved through specific binding of light chains [11, 12, 20].

Many unconventional myosins function as important cargo transporters. Adaptor proteins link the cargo to the cargo-binding domain of the molecular motor, mediating and specifying cargo tethering to the myosin. Myosin-cargo interactions govern the motor complex's mechanochemistry, oligomerization, and localization. Binding cargo can alleviate autoinhibition leading to the dimerization or oligomerization of the myosin's heavy chains and promote myosin processivity [11, 12, 20]. The different regulatory mechanisms do not function individually; rather, they exhibit significant interaction among themselves.

2.1.2 MyTH4-FERM myosins

Unconventional myosins have diverse functions and are involved in multiple cellular processes. Their diversity can be observed through variations in their structure and motor properties [14, 21].

Myosins can be classified into subfamilies based on their characteristics. Myosins that possess MyTH4-FERM domains, which refer to myosin tail homology and band 4.1/ezrin/radexin/moesin homology, are located in different membrane protrusions filled with actin and serve critical functions in their development and activities. MyTH4-FERM myosins are present in a range of organisms, from simple amoeboid species to humans [22, 23].

Examples of MyTH4-FERM myosins in the human genome include myosin-10 (M10) which contains one, while myosin-7 (M7) and 15 (M15) have two MyTH4-FERM domains in their C-terminal region.

The MyTH4-FERM family of myosin motors has retained a fundamental set of functions that can be observed across multiple cell types and evolutionarily distinct species. Both the *Dictyostelium* myosin-7 and mammalian myosin-10 are required for the extension of filopodia. Additionally, mammalian myosin-15, myosin-7a, and myosin-7b play a part in how stereocilia and microvilli extend or are organized [22, 23].

Structural studies indicate that MyTH4 and FERM domains comprise a supramodular organization while preserving the individual motifs` functions [22, 23]. The FERM motif serves as a protein interaction platform, binding to adhesion or signaling receptors, and various actin-binding proteins. Additionally, it plays an important role in autoregulation by binding to the myosin motor domain and thereby auto-inhibiting it. Since the MyTH4 motif has been demonstrated to interact with microtubules, cross-linking of different cytoskeletal filaments is possible [22, 23].

2.2 Human myosin-7a

A prominent member of the MyTH4-FERM subfamily is myosin-7. Myosin-7a (M7a) is essential for vision and hearing, while myosin-7b (M7b) is crucial for microvilli in the intestinal system [24-27].

Myosin-7a is expressed in various mammalian tissues, such as the testes, kidneys, and lungs. However, it is particularly prevalent in the inner ear and retina, specifically in the hair bundles and synapses of inner ear hair cells (IHC), photoreceptors, and the retinal pigment epithelium. Mutations in myosin-7a lead to deafness, vestibular dysfunction, and retinal degeneration [26, 28].

The full length myosin-7a is comprised of a motor domain followed by a short neck region containing 5 IQ motifs and a tail domain which has two MyTH4-FERM motifs separated by an SH3 (Src-homology) motif (**Figure 5**) [29].

***Figure 5**. Graphical representation of domain organizations of human myosin-7a. (Schematics are in scale with the length of their primary sequences).*

Previous research using the *Drosophila* homolog expressed in Sf9 cells has demonstrated that myosin-7a is a high duty ratio, monomeric motor that does not move processively on actin filaments [30, 31]. Furthermore, tail-truncated and motor-hybrid constructs have been utilized to investigate the motor functions of myosin-7a [32, 33]. However, the characterization of full-length mammalian myosin-7a has been challenging due to difficulties in expressing and purifying stable, intact protein.

The motor domain of myosin-7a is almost identical among primates and highly conserved among mammals, implying that this protein has gone through evolutionary adaptations to carry out essential functions in an organism's life cycle. Prior research has revealed that the myosin-7a motor possesses a high duty ratio (0.9), denoting that it is primarily bound to actin during its enzymatic cycle and is therefore suitable for transporting cargos [14]. Initial findings reveal that human myosin-7a glides actin at a

velocity ranging between 160 to 190 nanometers per second. However, these velocities surpass the recent *Drosophila* and human *in vitro* data by 10 to 20 times [33-36].

A recent study discovered that the cochlea produces two myosin-7a isoforms through alternative splicing, which differ by a short N-terminal extension. The canonical long isoform (M7a-L), with an 11-amino acid extension (MVILQQGDHVW), is expressed uniformly in the inner hair cells but tonotopically in the outer hair cells (OHC). Its level increases from the base to the apex of the cochlea. The pattern of expression for the truncated isoform (M7a-S), which does not have the 11-amino acid N-terminal extension, is predicted to have an inverse correlation with the canonical myosin-7a (**Figure 6**) [37, 38].

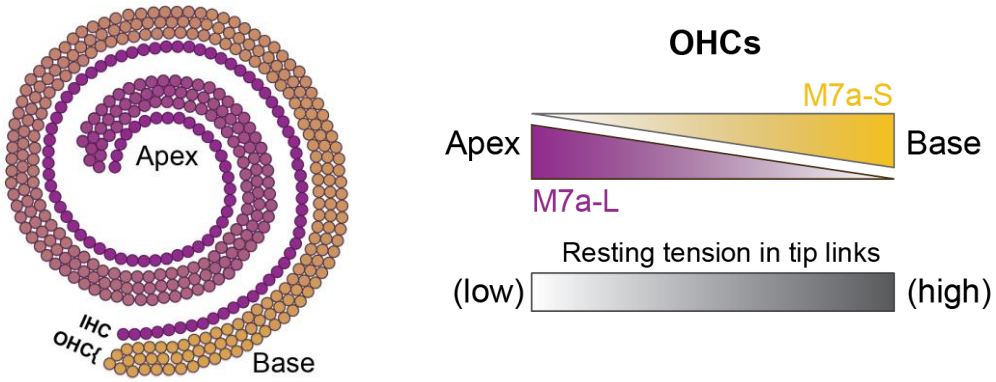

***Figure 6**. Expression pattern on the two myosin-7a isoforms in the cochlea. The IHCs express the long isoform uniformly, while in OHCs the expression pattern of the two isoforms is expected to be inversely correlated. The resting tension in tip links also follows a similar pattern to the short isoform. Figure is based on [37, 39].*

The N terminal extension is exclusive to mammals. Its unique pattern of expression indicates its possible involvement in mechanosensing, though no direct investigations have been conducted to confirm its exact role. The sequence is composed of 11 amino acids, predominantly hydrophobic, with the inclusion of neutral, basic, acidic, and aromatic amino acids.

The neck domain comprises 5 IQ domains in a tandem manner. Historically, only calmodulin has been co-expressed with myosin-7a [33, 35]. Previous studies have indicated that the IQ motifs of human myosin-7a have the capability to bind RLC and

ELC. However, a thorough analysis to precisely determine the endogenous light chain composition and characterize the native light chains has not been conducted. [40].

Previous studies have observed that the neck region of myosin-7a, as visualized through electron microscopy images, is comparatively shorter than other myosins that possess five IQ motifs [40]. Since myosin-7a has only been co-expressed with calmodulin in the past, it suggests that there may be alternative light chains binding to the IQ motifs, which would mean that the observed myosin was not fully decorated [40]. When comparing the IQ motifs of myosin-7a and myosin-7b, a high amino acid similarity (70%) is found, suggesting that both isoforms may potentially bind similar light chains. The identification of calmodulin-like protein 4 (CALML4) as the endogenous light chain for myosin-7b has raised the possibility of it binding to myosin-7a [41, 42]. CALML4 is highly enriched in stereocilia, implying its potential role as an endogenous light chain for myosin-7a (**Figure 7**) [43].

Consensus sequence	**IQxxxRGxxxR**
M7a-IQ1	TDRVILLQKVIRGFKDRSNFL
M7b-IQ1	DRAALSIQKVLRGYRYRKEFL
M7a-IQ2	KNAATLIQRHWRGHNCRKNYG
M7b-IQ2	RRAAVTLQAWWRGYCNRRNFK
M7a-IQ3	RLGFLRLQALHRSRKLHQQYR
M7b-IQ3	LVGFERLQAIARSQPLARQYQ
M7a-IQ4	RQRIIQFQARCRAYLVRKAFR
M7b-IQ4	RQRTVQLQALCRGYLVRQQVQ
M7a-IQ5	LWAVLTVQAYARGMIARRLHQ
M7b-IQ5	RRAVVVIQAHARGMAARRNFQ

***Figure 7**. IQ motifs of myosin-7a and myosin-7b compared to the consensus sequence[1]. The 3rd IQ motif of both M7a and M7b lacks glycine and second arginine in their consensus sequence.*

[1] Sequences from UniProt database:
M7a: https://www.uniprot.org/uniprotkb/Q13402/entry
M7b: https://www.uniprot.org/uniprotkb/Q6PIF6/entry

Several studies have shown that the short predicted coiled-coil sequence is insufficient to form a dimer [44]. Instead, it forms a single stable alpha-helix known as the SAH domain that acts as an extension of the lever arm. Artificial dimer forming motifs such as FK506 binding protein and Leucine Zipper have been successfully used to induce dimer formation and enable processivity in order to study its intrinsic motility in the dimeric state. The tail truncated recombinant proteins have exhibited similar characteristics both *in vivo* and *in vitro* [44, 45].

Myosin-7a's MyTH4 FERM motifs have the ability to interact with a broad spectrum of proteins. Both motifs are targeted by binding partners. Mutations in either of these genes disrupt normal hearing [46-48].

2.2.1 Physiological importance of human myosin-7a

Even though myosin-7a is expressed in a variety of tissues, in this dissertation we were only focusing on the inner ear and the neuroretina.

Hair cells are sensory cells in the inner ear that are essential for detecting sound and maintaining balance. Stereocilia are membrane protrusions filled with actin, located on the apical surface of hair cells. A "hair bundle" comprises about 100 stereocilia, arranged in a staircase-like pattern. Stereocilia are not independent, as they are connected by multiple linkers, including ankle links, side links, and tip links (**Figure 8**) [49, 50]. The process of mechanoelectrical transduction (MET) converts mechanical signals to chemical responses within the inner ear. This process requires proper organization of the stereocilia rows [50].

Myosin-7a is present in hair cells and localizes throughout the stereocilia. It is hypothesized to regulate mechanoelectrical transduction (MET) by tethering and generating tension. The presence of myosin-7a has been detected at both the upper tip link region and the base of the stereocilia [37, 46, 51]. According to a widely accepted model, mechanotransduction involves the opening of mechanically gated ion channels due to excitation of the hair bundle. The influx of ions generates an action potential, and the channels close via two independent mechanisms. The rapid response arises due to

direct feedback from the influx, as the ions bind to the channel causing it to close. The secondary response is a gradual adaptive process that includes a mechanism aimed at sustaining a suitable tension level to allow channels to react promptly [49, 50].

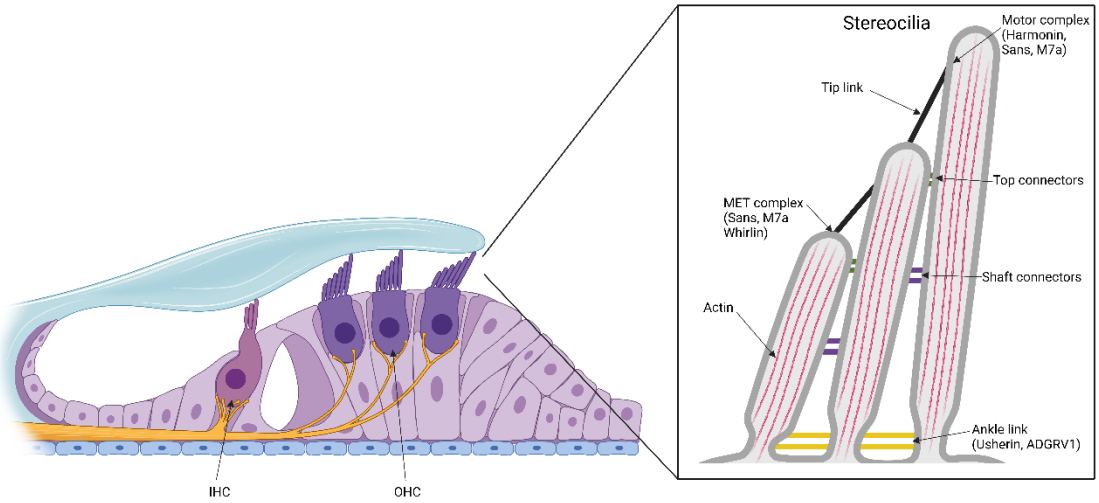

***Figure 8**. Graphical illustration of stereocilia noting the locations of various M7a binding proteins. On the apical side of the cell, the actin-filled stereocilia bundles organized into a staircase-like structure. Each stereocilium is linked to the next row via several linkers on their side and a tiplink on the top. Figure is based on [48]. Made with BioRender.*

There are two potential candidates as the adaptation motor: myosin-1c and myosin-7a [52]. Myosin 1-c is abundant in stereocilia tips, cycles between a rigid and a flexible lever arm conformation in a calcium-dependent manner. Furthermore, myosin-1c possesses slow transporter properties and is capable of sensing load [53-56]. However, a slow myosin, such as myosin-7a, is an also an excellent candidate as it is able to exert force on the links connecting stereocilia whilst translocating along the actin core. Its localization properties make it an ideal candidate for fulfilling this role [52, 57].

In the neuroretina, myosin-7a is localized in the retinal pigment epithelium (RPE) and in the connecting cilium and pericilium of the photoreceptors [58, 59]. It is most likely involved in opsin transport in the photoreceptors [60, 61] and in complex with MyRIP (Myosin and Rab Interacting Protein, also known as exophilin-8/Slac-2c) and Rab27a, it facilitates melanosome transport in RPE [58, 62].

Myosin-7a is involved in a variety of functions in the inner ear and the neuroretina, which requires complex regulatory processes. Our goal in this study is to investigate specific mechanisms responsible for these regulations.

2.2.2 MyRIP

MyRIP was identified as a Rab27a effector protein [47, 63]. MyRIP (Slac-2c) is closely related to melanophilin (Slac-2a) that is involved in skin melanosome transport serving as a linker between myosin-5a and Rab27a [64]. Functional studies suggest that MyRIP binds to both myosin-5a and myosin-7a, with a stronger affinity for myosin-7a [65-67].

Sequence analysis has identified three functional domains of MyRIP (**Figure 9**). These domains include: the N-terminal Rab27a-binding domain (RabBD, also known as Slp homology domain or FYVE), the myosin-binding domain (MyBD) in the middle, that interacts with the tail domain of myosin-5a and myosin-7a, and the C-terminal actin binding motif [47, 68, 69].

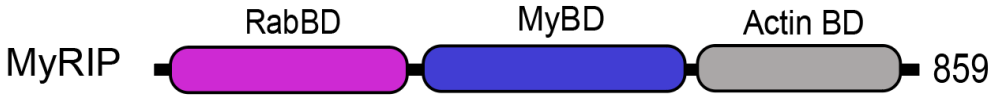

Figure 9*. Graphical representation of domain organizations of human MyRIP. (Schematics are in scale with the length of their primary sequences).*

Several studies have shown that MyRIP plays a role in transporting melanosomes within the RPE [58, 62, 68, 69]. In the absence of MyRIP, myosin-7a cannot be recruited to the melanosomes, resulting in their defective distribution [65, 67]. Importantly, MyRIP has also been shown to promote processive movement of myosin-7a within a cellular environment as well [45, 58, 68]. However, no thorough investigation has been done to reveal the molecular details of this induced processivity.

The presence of MyRIP was also detected in the synaptic region and along the hair cell bundles of cochlear and vestibular hair cells, co-localizing with myosin-7a [65]. MIR-96, a known neurosensory microRNA that plays a role in the development and upkeep of inner ear cells, has been demonstrated to regulate MyRIP at transcriptional

level [70, 71]. However, a comprehensive evaluation of MyRIP expression to explore its potential association with hearing loss has not been performed.

Whole sequence searches led to the discovery of homology between MyRIP and M7BP, a recently discovered binding partner of *Drosophila* myosin-7a [30]. Based on the organization of domains, MyRIP and M7BP share a domain that binds to myosin. Additionally, M7BP contains a putative Rab-binding domain at its N-terminus. Recent research indicates that this new binding partner induces processivity and dimerization of *Drosophila* myosin-7a, both *in vitro* and *in vivo*. Additionally, M7BP is suspected to bind and tether actin filaments in the presence of myosin-7a [30].

The similarities between MyRIP and M7BP prompted our investigation of MyRIP as a binding partner for human myosin-7a. The *Drosophila* myosin-7a data served as a comparison for our findings.

2.2.3 Usher syndrome

Usher Syndrome is a recessive genetic disorder that causes damage to the visual and auditory vestibular systems. It has a prevalence rate of 1-4 per 25,000 individuals, thus making it the primary cause of combined deafness-blindness. Usher syndrome is classified into three categories based on its severity. The USH1 phenotype is characterized by prenatal hearing loss, retinitis pigmentosa, which develops before puberty, and profound peripheral vestibular hypofunction. The USH2 phenotype features a severe congenital hearing loss accompanied by retinitis pigmentosa onset occurring post-pubertally and normal peripheral vestibular function. The USH3 phenotype shows progressive hearing loss combined with diverse vestibular dysfunction and retinitis pigmentosa which varies in onset [26, 48, 72].

Since the identification of MYO7A as the gene responsible for USH1B in 1995 [73], over a dozen genes have been discovered as causes of the disease [26, 48]. While the underlying mutations are widely researched, there are still unknown genes responsible for the disease. Additionally, MYO7A is associated with two forms of non-syndromic deafness, DFNB2 and DFNA11 [73].

Defects in myosin-7a can result in hair bundle disorganization, as well as changes to transduction and adaptation processes. Additionally, transportation of other stereocilia proteins may become compromised [74].

USH Type	Locus	Gene name	Protein name	Predicted function
USH1	USH1B	*MYO7A*	myosin-7a	Actin-based motor protein
	USH1C	*USH1C*	harmonin	PDZ scaffold protein
	USH1D	*CDH23*	cadherin 23	Cell adhesion
	USH1E	*N/A*	N/A	Unknown
	USH1F	*PCDH15*	protocadherin 15	Cell adhesion
	USH1G	*USH1G*	SANS	Scaffold protein
	USH1H	*N/A*	N/A	Unknown
	USH1J	*CIB2*	CIB2	Ca^{2+} and integrin binding
	USH1K	*N/A*	N/A	Unknown
USH2	USH2A	*USH2A*	usherin	Cell adhesion
	USH2C	*GPR98*	VLGR1	G-protein-coupled receptor
	USH2D	*DFNB31*	whirlin	PDZ scaffold protein
USH3	USH3A	*CLRN1*	clarin-1	Auxiliary subunit of ion channels
	PDZD7	*PDZD7*	PDZD7	PDZ scaffold protein

***Table 2**. The Usher proteins and their genes with their predicted function. Table is based on [26].*

The Usher proteins are all associated with Usher-syndrome and form a complex network. They are involved in actin-based intracellular trafficking, cell adhesion, scaffold function in multiprotein complexes, and are crucial for G protein-coupled or calcium-

based signaling) [75, 76]. Most of the Usher proteins are known or predicted to interact with myosin-7a [75, 76].

The Usher proteins exact cellular distribution in the retina remains unclear. Usher-associated proteins are primarily involved in transporting proteins and organelles within RPE cells and photoreceptors. However, certain subcellular structures, such as the calyceal process, are not uniformly found in mammals. These structures are present in primates but missing in rodents. Therefore, not every animal model is suitable for studying retina degeneration related to Usher syndrome [77].

2.2.4 Disease models

Multiple animal models are currently used in the study of Usher-syndrome. The below listed models are myosin-7a mutants.

The fly myosin-7a in *Drosophila* is encoded by the so-called *crinkled* locus. The crinkled mutation itself causes the fly to develop deformed bristles and deafness, but since the original discovery of this specific phenotype causing mutation, many other alleles have been identified in the *crinkled* locus. While some of these mutations are semi-lethal, a small percentage survives into adulthood but develops defects in their actin bundles [78-80]. Even though the fruit fly is a popular and convenient model organism, significant molecular evolutionary differences exist between the human and *Drosophila* myosin-7a ortholog.

Zebrafish that have a mutation in their myosin-7a ortholog are called *mariners*. They exhibit vestibular dysfunction and have disorganized stereocilia. *Mariner* was the first fish model established for the study of human hereditary deafness [81]. As a lower vertebrate, zebrafish offer many advantages to study hair cell function, but unfortunately no further studies had been conducted.

The *shaker-1* mouse mutant was first described more than 100 years ago. The Arg-502 residue of the myosin-7a heavy chain, which has a role in the segment interacting with actin, is replaced to a proline residue. The mutant mice have progressive hair bundle disorganization and abnormal auditory responses, which later develops into

hearing loss [82, 83]. Ever since the initial discovery of the shaker mutant, many other Usher protein mice mutants have been established. However, as mentioned above certain structures are missing in rodents, and therefore mice are not an appropriate model to study myosin-7a mutation induced retina degeneration.

3 Aims

For human myosin-7a to fulfill its physiological roles, multiple regulatory mechanisms are employed. These mechanisms, both intra- and intermolecular, adjust the myosin's localization, conformation, oligomeric state, and overall activity. The objective of this dissertation is to gain understanding of certain selected mechanisms. I wished to answer the following questions:

1. **How to express and purify full-length human myosin-7a?** Only tail-truncated and motor-hybrid constructs have been utilized to investigate the motor functions of human myosin-7a due to the difficulty of expressing and purifying stable, intact full-length protein. We aimed to develop an optimize a protocol to purify full-length myosin-7a.

2. **What are the molecular details of human myosin-7a`s light chain composition?** Although human myosin-7a has so far been co-expressed and purified with calmodulin, it has been demonstrated that other light chains can also bind to myosin-7a's IQ motifs. Our aim is to determine the accurate light chain composition of myosin-7a.

3. **What effect does calcium exert on the structure and function of myosin-7a?** Calcium is a crucial regulatory cation in the inner ear. During MET, myosin-7a is exposed to an influx of calcium ions. Our aim was to uncover the potential effect of calcium on the structure and enzymatic function of the myosin.

4. **What is the role of the N-terminal extension?** Myosins frequently possess an N-terminal extension that modifies motor function. Following the identification of a brief N-terminal extension of myosin-7a, our research aims to examine its impact on the motor function.

5. **What are the motile properties of myosin-7a?** Monomeric myosins can be activated and dimerized through binding partners. In this study, we investigated how MyRIP, a known binding partner of myosin-7a, induces the processivity of the motor protein. In addition, we assessed the intrinsic motility of myosin-7a in the dimer state by using an artificial dimer.

4 Materials and Methods

4.1 Molecular biology methods

4.1.1 Bioinformatic methods

All DNA constructs were designed using SnapGene 6.1.2. **Tables 3** and **4** list the DNA constructs. PCR primers were ordered from Integrated DNA Technologies or Eurofin Genetics and were made to optimize InFusion cloning by Takara Bio. Melting temperatures were determined using the New England Biolabs online T_m calculator (https://tmcalculator.neb.com/). The molar weight of the purified proteins was determined using Expasy ProtParam (http://web.expasy.org/protparam/).

	GeneID (#)	*NCBI Reference Sequence*
Myosin-7a	4647	NM_000260.4
MyRIP	25924	NM_001284423.2
CaM	380558	NM_001329922.1
CALML4	91860	NM_033429.3
RLC (MYL12B)	103910	NM_001144944.1

***Table 3**. GeneIDs of the proteins used in this dissertation.*

4.1.2 Cloning templates and materials

The reference sequences used in this work are summarized in **Table 3**. Human myosin-7a-FLAG, MyRIP-FLAG, RLC and CaM in pFastBac1 were provided[2]. The MultiBac kits were ordered from Geneva Biotech. The restriction enzymes and homing endonuclease were acquired from New England Biolabs. pCMV-GFP (Plasmid #11153) and pET15b-MHL (Plasmid #26092) were purchased from Addgene. CALML4 in

[2] The constructs were previously made by András M. Kengyel, Rong Liu and Neil Billington, LMP, NHLBI, NIH.

pFastBac1 was designed and ordered from GenScript. For all our constructs, we amplified DNA using Q5® High-Fidelity DNA Polymerase from New England Biolabs. All of our assembled vectors were created through implementation of InFusion cloning. The PCR products were amplified with 15 base pairs homology to the vector backbone and the InFusion enzyme recognizes these overlaps at their ends, subsequently merging the PCR product and the linearized vector together.

4.1.3 Cloning of myosin-7a into baculovirus

The baculovirus/*Sf9* expression system allows for efficient recombinant protein production in insect cells. The pFastBac1 vector recombines with the parent bacmid in DH10Bac *E. coli* competent cells to create an expression bacmid. After that, the bacmid gets transfected into insect cells for producing recombinant baculovirus particles [84].

In our attempt to express and purify full-length human myosin-7a, we used pFastBac1 to create an expression bacmid. However, in expressions where multiple bacmids (heavy chain, three different light chains) were co-transfected, the purification yield was very low.

4.1.4 Cloning of myosin-7a into MultiBac system

Since the production of the myosin holoenzyme requires the expression of several proteins encoded by separate viruses, we utilized the MultiBac system – an advanced Baculovirus system designed for producing large, multimeric protein complexes in insect cells [85].

The full-length heavy chain of myosin-7a (M7a-FL) was amplified with 15-base pair homology for both EcoRI cloning sites on the pACEBac1 vector. The PCR product and the EcoRI-digested pACEBac1 vector backbone were fused using InFusion (TakaraBio). The overhangs of the 15 base pairs were planned according to the correct insertion orientation. The gene cassette in the pACEBac1 vector includes an I-Ceu recognition site (homing endonuclease) ahead of the polyhedrin promoter and a BstXI recognition site subsequent to the SV40 terminator. The homing endonucleases produce

cohesive ends, which complement those generated by the BstXI digestion. The entire expression cassette is removed and inserted into another pACEBac1 vector digested with only BstXI and linked with T4 DNA ligase (**Figure 10**). The process eliminates all restriction sites, except for the BstXI site located at the end of the insertion. This allows for the insertion to be repeated with another gene cassette.

The sequences for RLC, calmodulin, and CALML4 were inserted into the pACEBac1 vector following the procedure for myosin-7a heavy chain insertion. The light chain gene cassette insertions were performed consecutively. The resulting constructs contained multiple gene cassettes and were designated as "MULTI" (**Figure 11**, **Table 5**.)

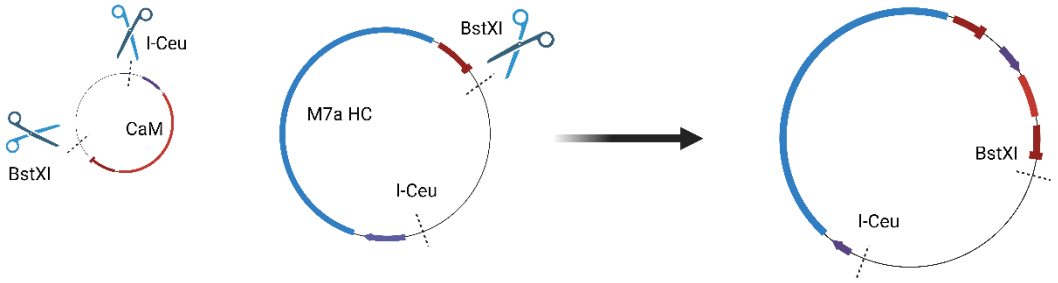

***Figure 10**. Graphical representation of MultiBac cloning. CaM gene cassette is digested with I-Ceu and BstXI. CaM gene cassette is then inserted into M7a HC gene containing pACEBac1 digested with BstXI.*

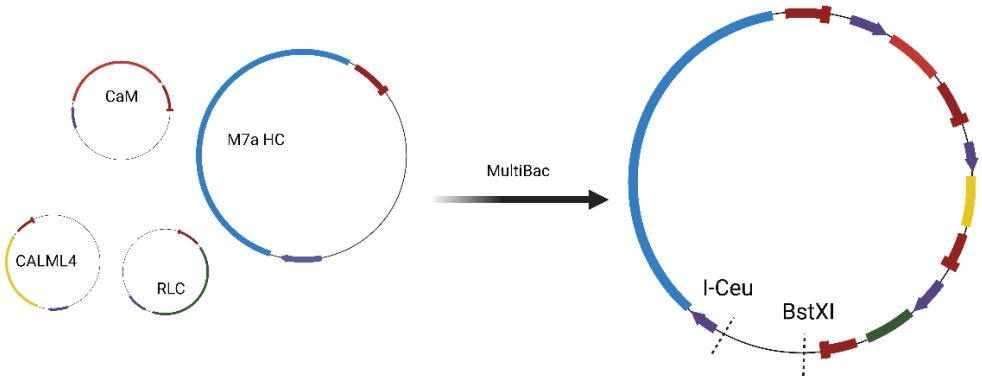

***Figure 11**. Graphical representation of the MultiBac vector. Each gene cassette has its own polyhedrin promoter (purple) and SV40 terminator (red) region.*

4.1.5 Site directed mutagenesis

The MultiBac assembly employs BstXI digestion sites, but the myosin-7a sequence and CALML4 each contain two recognition sites (CCANNNNNNTGG) susceptible to restriction digestion. To prevent this issue, we utilized the Q5 Site Directed Mutagenesis kit (New England Biolabs) to mutate the CCANNNNNNTGG sites to CCANNNNNNTAG and CAANNNNNNTGG. These mutations did not result in any changes to the translated amino acid sequence (**Table 4**).

Protein	Position	DNA sequence	Amino acid sequence
M7a	5`–298 … 312 –3`	TCCATCCTGGT**G**GCT	Ser-Ile-Leu-**Val**-Ala
mutated		TCCATCCTGGT**A**GCT	Ser-Ile-Leu-**Val**-Ala
M7a	5`– 3790 … 3744 –3`	CCCAGCTGGCT**G**GAG	Pro-Ser-Trp-**Leu**-Glu
mutated		CCCAGCTGGCT**A**GAG	Pro-Ser-Trp-**Leu**-Glu
CALML4	5`– 265 ... 279 –3`	GC**C**ATGTTGATGGTG	**Ala**-Met-Leu-Met-Val
mutated		GC**A**ATGTTGATGGTG	**Ala**-Met-Leu-Met-Val

Table 4. *Site-directed mutagenesis of BstXI recognition sites. DNA bases in bold indicates the mutation sites.*

4.1.6 Cloning of other constructs in this work

To visualize MyRIP, we created a fluorescent protein containing an mCherry-tag on its C-terminal, followed by a FLAG-tag. However, the recombinant protein showed propensity for fragmentation during expression and purification, as indicated by the results. Consequently, we opted to place the mCherry fluorescent-tag at the N-terminus of the protein. We cloned the myosin-binding domain (MyBD) of MyRIP to evaluate its ability to bind to myosin-7a and promote processivity.

The CALML4 sequence was designed and ordered from GenScript in the pFastBac1 vector. In order to produce and purify the light chain, we cloned the sequence into the pET15-MHL bacterial expression vector, which is suitable for T7 promoter-

driven expression of recombinant proteins with the addition of an 18 amino acid N-terminal fusion tag containing 6X His followed by a TEV cleavage site.

To examine the intrinsic and MyRIP-induced processivity of myosin-7a in a cellular setting, we employed the CMV vector. We cloned GFP-tagged full-length myosin-7a, GFP-tagged S1-SAH-Zipper-myosin-7a, and mCherry-tagged MyRIP into pCMV separately.

4.1.7 Summary of cloning

Over the course of this work, several different vectors containing DNA constructs were created. The summary of them can be found in **Table 5**. We engineered multiple different length myosin-7a constructs (**Figure 12**). Full-length (FL) myosin-7a refers to the 2215 amino acid long canonical myosin. Subfragment 1 (S1) refers to the motor domain and the first IQ motif, while 5IQ refers to the motor domain and all five IQ motifs. S1-SAH-Zipper designation is for the artificial dimer construct containing the motor domain, the five IQ motifs, and the SAH domain followed by a leucine zipper. If not mentioned separately, the heavy chain includes the canonical N-terminal extension. If the GFP component is mentioned, it is located at the N-terminus of the motor domain. In all of the constructs we utilized, the FLAG affinity tag was situated at the C-terminus of protein.

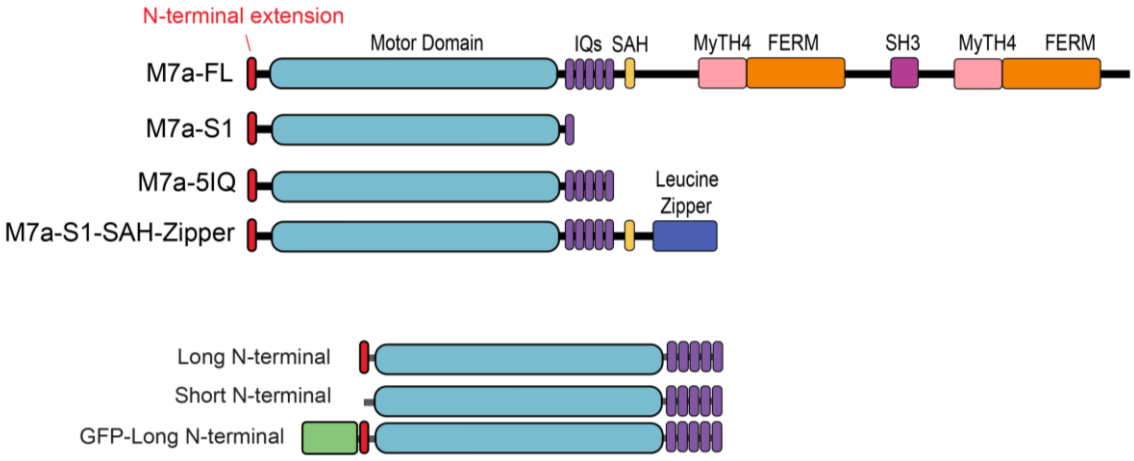

***Figure 12**. Graphical representation of human myosin-7a constructs used in this dissertation.*

	Recombinant protein	Vectors	*Host*
Myosin-7a heavy chain constructs	○ M7a-FL-FLAG ○ GFP-M7a-FL-FLAG ○ M7a-S1-FLAG ○ M7a-5IQ-FLAG ○ SHORT-M7a-5IQ-FLAG ○ GFP-M7a-5IQ-FLAG ○ GFP-M7a-S1SAH-Zipper-FLAG	pFastBac1	*Sf9*
	○ M7a-FL-FLAG ○ SHORT-M7a-FL-FLAG ○ GFP-M7a-FL-FLAG ○ GFP-M7a-S1SAH-Zipper-FLAG	pACEBac1	*Sf9*
Light chains constructs	○ CaM ○ CALML4 ○ RLC	pFastBac1	*Sf9*
	○ CaM ○ CALML4 ○ RLC ○ Light Chain-MULTI	pACEBac1	*Sf9*
	○ CALML4	pET-MHL	*E. coli*
Myosin-7a MULTI constructs (heavy chain plus light chains)	○ M7a-FL-FLAG-MULTI ○ SHORT-M7a-FL-FLAG-MULTI ○ GFP-M7a-FL-FLAG-MULTI ○ GFP-M7a-S1SAH-Zipper-FLAG-MULTI	pACEBac1	*Sf9*
MyRIP constructs	○ MyRIP-FLAG ○ mCherry-MyRIP-FLAG ○ MyRIP- mCherry-FLAG ○ MyBD-FLAG	pFastBac1	*Sf9*
Mammalian transfection constructs	○ GFP-M7a-FL ○ mCherry-MyRIP ○ GFP-M7a-S1SAH-Zipper	pCMV	*ARPE19*

Table 5. *Summary of vectors and recombinant constructs used in this dissertation.*

4.2 Protein expression and purification

4.2.1 Purification of myosin-7a

FLAG-tagged myosin-7a recombinant protein was expressed in *Sf9* insect cells, which were previously infected with pACEBac1-Multi plasmid or co-infected with different pFastBac plasmids containing the heavy chain and light chains. The cells were centrifuged after 72-hour expression and the pellet was frozen in liquid nitrogen and stored at –80 °C until further use. Every process of the purification was performed at 4 °C. The frozen pellet was thawed on ice, washed, and homogenized in a buffer containing: 10 mM MOPS (3-(N-morpholino)propane sulfonic acid), 500 mM NaCl, 10 mM $MgCl_2$, 1 mM EGTA, 0.3 mM NaN_3, 1 mM DTT, 0.1 mM PMSF (phenylmethylsulphonyl fluoride), 4 μg Leupeptin, 5 mM ATP, Pierce protease inhibitor tablet (pH 7.4). After sonication (5 min, 5 s impulses with 3 s pauses, 60 % amplitude), the cellular debris was removed by ultracentrifugation (48000 g, 30 min). Monoclonal anti FLAG M2 resin (2 ml) (Sigma) was added to the supernatant and incubated for 1 hour at 4 °C while shaking. After 1 hour of gentle shaking the resin was loaded into a column. The resin was then washed with a buffer containing: 500 mM NaCl, 10 mM MOPS, 0.1 mM EGTA, 3 mM NaN_3, 0.1 mM DTT, 0.1 mM PMSF, 10 mM $MgCl_2$, 5 mM ATP, 4 μg Leupeptin (pH 7.4) to dissociate actin from myosin-7a and to remove unspecific bound proteins from the resin, then washed again with a buffer containing: 500 mM NaCl, 10 mM MOPS, 0.1 mM EGTA, 3 mM NaN_3, 0.1 mM PMSF, 4 μg Leupeptin, (pH 7.4). Myosin-7a was eluted with a FLAG protein containing buffer (500 mM NaCl, 2.5 mM MOPS, 25 μM EGTA, 0.75 mM NaN_3, 50 mg/ml FLAG peptide, (pH 7.4)). 300 μl fractions were collected, pooled and dialyzed against a buffer containing 500 mM NaCl, 2 mM $MgCl_2$, 0.1 mM EGTA, 10 mM MOPS, 1 mM DTT (pH 7.4). The purified protein was frozen in liquid nitrogen and stored at -80 °C.

4.2.2 Purification of MyRIP

MyRIP construct with a C-terminal mCherry-tag followed by a FLAG-tag were cloned into pFastBac1. *Sf9* insect cells were infected with the respective plasmids, then

centrifuged after 72-hour expression and the pellet was frozen in liquid nitrogen and stored at –80 °C until further use. The purification process was similar as described for myosin-7a.

4.2.3 CALML4 protein expression and purification

CALML4 in pFastBac1 was purchased from GeneScript. The coding sequence was cloned into pET15b-MHL vector using BseRI and then KRX cells (Promega) were transformed with the light chain-containing plasmid. The transformed and IPTG induced cells were centrifuged after overnight expression at 25°C and the pellet was frozen in liquid nitrogen and stored at –80 °C until further use. Every process of the purification was performed at 4 °C. The frozen pellet was thawed on ice, washed, and homogenized with 2X PBS buffer (pH 7.4). After sonication (5 min, 5 s impulses with 3 s pause, 60 % amplitude), the cellular debris was removed by ultracentrifugation (48000 g, 30 min). NEBExpress® Ni resin was added to the supernatant and the samples were gently shaken on the rotorack at 4°C. After 1 hour shaking, the resin was loaded on column and sedimented. It was washed with a 2X PBS buffer containing 5 mM imidazole (pH 7.4). CALML4-His was eluted with a 2X PBS buffer (pH 7.4) containing 500 mM imidazole and dialyzed against a buffer containing: 25 mM Tris-HCl, 150 mM NaCl, 14 mM MEA (pH 8). His-tag was cleaved with 1 unit to 2 μg CALML4-His TEV protease (Sigma) added to the dialysis buffer. The digested protein was loaded again on NEBExpress® Ni resin, incubated for 30 minutes and the flow through was collected and dialyzed in the dialysis buffer. The purified protein was frozen in liquid nitrogen and stored at –80 °C.

4.2.4 Expression and purification of other proteins used in this work

Actin was purified from Rabbit Muscle Acetone Powder (Pel-Freeze Biologicals) and prepared[3] according to standard protocol based on [86]. Calmodulin was purified[3] according to previously published protocols [87].

[3] The actin and calmodulin were prepared by Zhang Fang, LMP, NHLBI, NIH.

GFP-RLC was cloned into pFastBac1 plasmid and expressed in *Sf*9 insect cells. The cells were centrifuged after 72-hour expression and the pellet was frozen in liquid nitrogen and stored at –80 °C until further use. Every process of the purification was performed at 4 °C. The frozen pellet was thawed on ice, washed, and homogenized with a buffer containing: 2 M Urea, 25 mM Tris HCl, 0.1 mM PMSF, 1 mM DTT, 0.001% NaN_3, (pH 7.5). In the rest of this paragraph, we refer to this as RLC buffer. The cellular debris was removed by ultracentrifugation (48000 g, 1 h). The supernatant was applied to Q Sepharose anion-exchange column, washed with RLC buffer containing 200 mM NaCl and eluted with RLC buffer containing 300 mM NaCl. The eluant was diluted 4-fold into RLC buffer to reduce the ionic strength and applied to a DEAE–Sepharose column (Sigma). After washing with RLC buffer, protein was eluted using a salt gradient from 0 to 300 mM NaCl. The eluant was precipitated using ammonium sulfate in 5% increments and precipitates were resuspended in PBS, followed by dialysis against PBS completed with 5 mM DTT. The fractions were assessed by SDS-PAGE and the purest was applied to a Superdex® 200 Increase 10/300 GL gel filtration column (Sigma). Fractions were collected and according to an SDS PAGE the purest fractions were frozen in liquid nitrogen.

4.3 Electrophoretic methods

4.3.1 Gel electrophoresis

The effectiveness of the purifications was assessed through SDS-PAGE according to Laemmli's method. NuPage™ 4-12% Bis-Tris and Novex™ WedgeWell™ 16% Tris-Glycine gels were utilized. Subsequently, the gels were stained with Acquablue stain and then analyzed by using Azure 600 (Azure Biosystems).

4.3.2 Immunoblot

Two different techniques were employed to transfer proteins from polyacrylamide gel to nitrocellulose. The first method, a wet transfer, used Tris-Glycine SDS running buffer with 20% methanol and was carried out on ice for 2 hours. The second methods, a

semi-dry transfer, used a Bio-Rad Turbo-blot device with provided Transfer Buffer. The summary of antibodies used in this dissertation can be found in **Table 6.**

After the blotting process, the membrane was blocked for an hour at room temperature using Bio-Rad Blocking Buffer. The primary antibody was then incubated overnight at 4 °C. Following thorough washing, the membrane was further incubated with the secondary antibody at room temperature for an hour. The imaging procedure was then carried out using Azure Biosystems 600.

Antibody	*Host*	*Dilution*	*Catalog number*	*Manufacturer*
CALML4	*Rabbit*	1:5000	15894-1-AP	ProteinTech
M7a	*Mouse*	1:1000	Sc-74516	Santa Cruz Biotechnology
FLAG	*Rabbit*	1:1000	PA1-984B	Invitrogen
GFP	*Mouse*	1:500	11814460001	Roche
HSP90	*Rabbit*	1:1000	4874	Cell Signaling Technology
UNC45B	*Rabbit*	1:1000	PA5-114191	Invitrogen
MyRIP	*Rabbit*	1:1000	BS-11038R	Bioss
mCherry	*Rabbit*	1:1000	PA5-34974	Invitrogen
Anti-Rabbit 800CW	*Goat*	1:10000	D11103-01	LICOR
Anti-Mouse 680RD	*Goat*	1:10000	D10901-11	LICOR

***Table 6**. Summary of antibodies used in the dissertation.*

4.3.3 Electrophoretic mobility shift assay

A Ca^{2+}- dependent electrophoretic shift assay was conducted with modifications to the previously described method [88]. Purified calmodulin (1 μM) and CALML4 (1 μM)

were incubated for 20 minutes at room temperature with 5 μM $CaCl_2$ or 1 μM EGTA. The resulting samples were then subjected to 16% SDS–PAGE, which ran with a constant current of 30 mA in Tris Glycine buffer for 2 hours at room temperature.

4.4 Biophysical methods

4.4.1 Total internal reflection fluorescence microscopy

Total internal reflection fluorescence microscopy (TIRFM) is able to provide the excitation of fluorophores in an extremely thin optical section (~200 nm). TIRFM uses an evanescent field to illuminate and excite fluorophores. The evanescent field is generated when the excitation light is totally internally reflected at the solid-liquid interface, in our case at the border between the glass coverslip and the protein solution. Only the fluorescent molecules in the evanescent field within a few hundred nanometers of the interface will be excited, since the intensity of this evanescent wave decays exponentially with distance from the surface. Every other fluorescent molecule outside of the evanescent field remains in a dark, unexcited state. This improves the signal-to-noise ratio, which allows the visualization even of a single fluorophore.

4.4.2 Actin gliding assay

Flow chambers were prepared using No. 1.5 thickness 22 mm square glass coverslips and microscope glass slides (**Figure 13**). The coverslips were covered with 1% nitrocellulose dissolved in amyl acetate and then fixed on a cleaned glass slide with double sided tape. Full-length myosin-7a was bound to the coverslip in low salt conditions (~ 0.2 mg/ml myosin in 150 mM NaCl, 20 mM MOPS, 5 mM $MgCl_2$, 0.1 mM EGTA, pH 7.4). After thorough washing steps, rhodamine phalloidin labeled actin (20 nM) was flushed in the chamber. The actin motility was observed in the final assay buffer (150 mM NaCl, 20 mM MOPS, 5 mM $MgCl_2$, 0.1 mM EGTA, 50 mM DTT, 5 mM ATP, 2.5 mg/ml glucose, 100 μg/ml glucose oxidase, 2 μM GFP-RLC, 2 μM CaM, 2 μM CALML4; 200 μM $CaCl_2$).

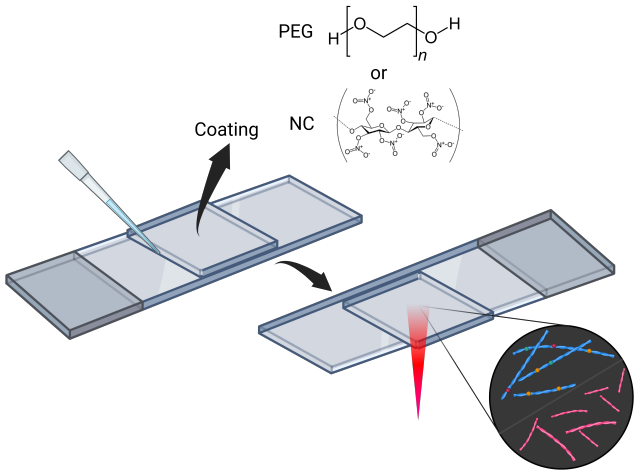

***Figure 13**. Graphical representation of a flow chamber. Coating on the coverslip: PEG (polyethylene glycol) – for single molecule assay or NC (nitrocellulose) – for actin gliding assay. The coverslips were attached to clean slides using double sided tape.*

The observation was performed at 24 °C. Movies were collected on an inverted Nikon Eclipse Ti-E microscope with an H-TIRF module attachment, a CFI60 Apochromat TIRF 100x Oil Immersion Objective Lens (N.A. 1.49, W.D. 0.12 mm, F.O.V 22 mm) and an EMCCD camera (Andor iXon Ultra 888 EMCCD, 1024x1024 array, 13 um pixel). The excitation light source was a Nikon LU-N4 Laser Unit equipped with four lasers (405, 488, 561, 640 nm).

Where required, movies were drift corrected using the ImageJ/FIJI plugin Image Stabilizer. Actin filament centroid positions were determined using a FIJI macro which is based on the ridge detector plugin. Detected centroid positions were converted to a new image with a circle representing each centroid and the movement of these circles was then analyzed using the TrackMate plugin for ImageJ. TrackMate settings were: LoG detector (estimated blob diameter 1 μm, threshold: not set), initial threshold: not set, view: HyperStack Displayer, filters on spots: not set, tracker: Simple LAP tracker (Linking max distance: 0.2 μm, gap-closing max distance: 0.2 μm, gap-closing max frame gap: 2), filters on tracks: Number of spots in track (above 5). Raw data were obtained from the Analysis tab of the TrackMate plugin and imported into GraphPad Prism 7 for analysis.

Track mean line speed was used as the output velocity. Gaussian fits of the velocity histograms were used to determine average velocity.

$$Y = Amplitude \times e^{(-0.5\times(X-mean/SD)^2)}$$

4.4.3 Single molecule motility assay

Flow chambers were prepared using No. 1.5 glass coverslips and glass slides. The coverslips were repeatedly washed with 100% ethanol and distilled water, and then thoroughly dried with a stream of filtered air and plasma cleaned for 10 min in argon. Biotin-PEG mixture was added to the surface of the coverslip. After a 20 min incubation at 70 °C the coverslips were rinsed thoroughly with distilled water and then fixed on a cleaned slide with double-sided tape. Biotin phalloidin (ThermoFisher Scientific) actin (200 nM) was bound to the surface of the coverslip via NeutrAvidin (Fisher Scientific, 2 mg/ml). Myosin (~0.01 mg/ml in 150 mM NaCl, 20 mM MOPS, 5 mM $MgCl_2$, 0.1 mM EGTA, pH 7.4) was added. The motility was observed in the final assay buffer (150 mM NaCl, 20 mM MOPS, 5 mM $MgCl_2$, 0.1 mM EGTA, 50 mM DTT, 5 mM ATP, 2.5 mg/ml glucose, 100 μg/ml glucose oxidase, 2 μM GFP-RLC, 2 μM CaM, 2 μM CALML4). Movies were collected as mentioned before.

Processive runs were analyzed using the TrackMate plugin for ImageJ. TrackMate settings were: LoG detector (estimated blob diameter 0.5–0.7 μm, threshold: 40–100), initial threshold: not set, view: HyperStack Displayer, filters on spots: not set, tracker: Simple LAP tracker (Linking max distance: 0.2 μm, gap-closing max distance: 0.2 μm, gap-closing max frame gap: 2), filters on tracks: duration of track (above 30 s), track displacement (above 0.39 μm), velocity standard deviation (below 0.3). Raw data were obtained from the Analysis tab of the TrackMate plugin and imported into Prism 7 for analysis.

Track mean line speed was used as the output velocity. Histograms were created using GraphPad Prism 7 software. Gaussian fits of the velocity histograms were used to determine average velocity. Characteristic run lengths and run durations were determined via exponential fits of the corresponding histograms.

$$(Y = (Y_0 - Plateau) \times e^{(-K \times X)} + Plateau),$$

where X is time or distance and K is a rate constant equal to the reciprocal of the X axis units. The reciprocal of K (Tau) was used as the characteristic length or duration of runs.

4.4.4 Steady-state ATPase activity

Steady-state ATPase activities at different F-actin concentrations were measured in SpectraMax ID3 microplate reader at 37°C in buffers containing 10 mM MOPS, 1 mM ATP, 50 mM NaCl, 2 mM $MgCl_2$, 0.1 mM EGTA (pH 7.2). Data were collected with Softmax Pro 7.1 software and plotted by Graphpad Prism 7.0. The buffers also contained a NADH-coupled ATP-regenerating system including 40 units/ml lactate dehydrogenase, 200 units/ml pyruvate kinase, 200 µM NADH and 1 mM phosphoenolpyruvate. The rate of ATP hydrolysis was calculated from the decrease of absorbance at 340 nm caused by the oxidation of NADH based on Michaelis-Menten kinetics and normalized to the myosin concentration. To get the kinetic parameters the ATPase rates were plotted against the F-actin concentration and a Michaelis-Menten curve was fitted on the data points.

$$Y = v_{max} \times \frac{X}{(K_M + X)},$$

where v_{max} is the maximum enzyme velocity; K_M is the Michaelis-Menten constant which is the substrate concentration (X) needed to get a half-maximum enzyme velocity.

4.4.5 Negative stain electron microscopy and image processing

Proteins were diluted in a buffer containing 150 mM NaCl (or 500 mM NaCl, where stated in the text), 10 mM MOPS, 2 mM $MgCl_2$, 0.1 mM EGTA. Dilution buffer for myosin also contained 100 µM ATP (pH 7.0). Samples were applied to UV-treated, carbon coated EM grids and stained immediately using 1% uranyl acetate. Micrographs were recorded on a JEOL 1200EX microscope using an AMT XR-60 CCD camera at a nominal magnification of 60,000x. Reference-free image alignments and K-means classification were conducted using SPIDER software.

4.4.6 Single molecule mass photometry

Mass photometry (MP) is a novel bioanalytical technique that enables measurement of the molecular mass of biomolecules at the individual level [89]. A contrast signal is produced through the interference between light scattered by the biomolecule and reflected light from the glass surface it is on, and this signal is directly proportional to the biomolecule's mass. With a calibration reference, it is possible to ascertain the molecular mass of each individual biomolecule with high accuracy (**Figure 14**).

The Refeyn One MP mass photometer was utilized to obtain data on single molecule landing. The cleaning protocol for microscope slides involved consecutive washes with water, ethanol, and isopropanol, followed by drying with nitrogen. A silicone gasket was also cleaned with water and nitrogen, then positioned onto a cleaned microscope slide. Afterward, 20 nM of each sample or mixture was loaded into a single gasket. The data collection lasted for a duration of 1 minute.

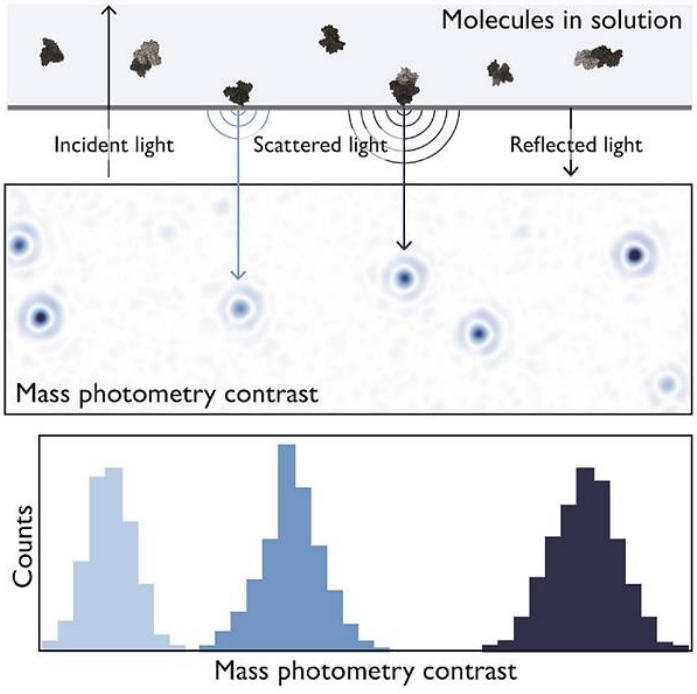

Figure 14. *Graphical visualization of single molecule mass photometry* [4]

[4] https://www.refeyn.com/about-mass-photometry

Measurements were conducted at room temperature (~24 °C), and images were processed using the manufacturer-supplied software (Refeyn, UK). The calibration between molecular mass and contrast was established using protein standards of known molecular weight [90]. For each sample, a Gaussian fit was applied to a histogram.

4.4.7 Isothermal Titration Calorimetry

Isothermal Titration Calorimetry (ITC) experiments were performed using MicroCal ITC-200 instrument (Malvern). Measurements were carried out in a buffer containing 20 mM HEPES (pH 7.4). 260 µM CALML4 was placed in the reaction cell, 8 mM Ca^{2+} was loaded into the ITC syringe. Titration consisted of 20 injections, 0.4 µl for the first injection and 2 µl for all following injections at 2 min intervals. Data analysis was performed with built-in software using calcium-to-buffer as a control.

4.4.8 MicroScale Thermophoresis

Microscale Thermophoresis (MST) is a technique that allows for the measurement of biomolecular interactions without requiring immobilization. By utilizing MST, changes in the size, charge, and hydration shell of fluorescent molecules can be detected as they move through a small temperature gradient (**Figure 15**).

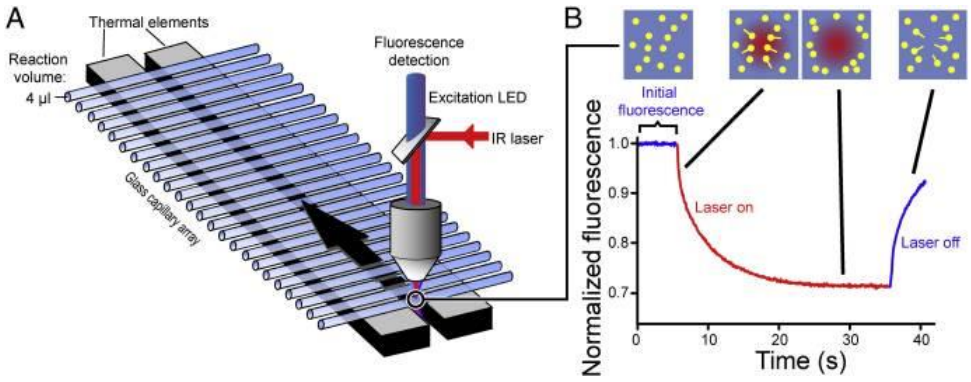

Figure 15. *Graphical representation of microscale thermophoresis instrument and measurement principles [91].*

MST measurements were conducted using a Monolith NT.115 device with the laser power set to 60%. The subsequent analysis of the MST traces was carried out employing MO.Affinity Analysis software (Nanotemper) [92].

The Monolith NT^{TM} His-Tag labelling kit was used for labelling His-CALML4 and His-calmodulin with RED-tris-NTA dye. The previously diluted dye was added to the target protein in molar ratio 1:2 (100 nM dye:200 nM protein), followed by incubation for 30 minutes at room temperature. The sample was centrifuged for 10 minutes at 4°C at 15000g. The final protein concentration in a reaction was 50 nM.

Binding affinity assays were carried out using a 16-concentration dilution series of calcium (calmodulin: 5 mM – 150 nM, CALML4: 2 M – 60 μM). Each dilution was loaded into Monolith^{TM} capillaries (~5-7 μl). Data fitting were calculated using the built MO.Affinity Analysis based on the K_D model:

$$f(c) = \frac{c + c_T + K_D - \sqrt{(c + c_T + K_D)^2 + 4 \times c \times c_T}}{2 \times c_T},$$

where f(c) is the fraction bound at a given ligand concentration (c), K_D is the dissociation constant or binding affinity and c_T is the final concentration of target in the assay.

4.4.9 Mass Spectrometry

Samples were separated on NuPage^{TM} 4-12% Bis-Tris gel, stained with Coomassie Blue and then rinsed with distilled water. To prepare it for reduction and alkylation with DTT and IAD, the gel was destained and dehydrated using a bi-carbonate and methanol solution. Peptides were extracted with 5% formic acid and 50% acetonitrile after an overnight trypsin digestion. They were then purified with C_{18} resin containing ZipTips. Using LC-MS/MS, the peptides were concentrated and analyzed.

4.4.10 Airyscan microscopy

Airyscan imaging was performed on a Zeiss LSM 880 Airyscan microscope equipped with a 63 × 1.4 NA objective. Raw data was processed using Airyscan processing in "auto strength" mode (mean strength ± S.D. = 5.5 ± 1.3) with Zen Black software version 2.3.

4.5 Cell culture methods

4.5.1 ARPE19 transfection

ARPE-19, a spontaneously arising human retinal pigment epithelia (RPE) cell line, was acquired from ATCC (CRL-2302™). The cells were cultured in DMEM:F12 medium with 10% FBS in 25 cm^2 culture flasks at 37 °C and 5% CO_2.

Prior to transfection, cells with a low passage number were seeded in chambered coverglass (*In vitro* Scientific). Transfection reagent Avalanche (EZ-Biosystems) and CMV plasmid DNA were diluted in Opti-MEM I Reduced Serum Medium (Gibco™), then carefully added dropwise to each well. The transfection solution was removed following a 5-hours of incubation period at 37 °C in a CO_2 incubator. Cellular observations were conducted 48 hours post-incubation.

5 Results

5.1 *In vitro* characteristics of purified myosin-7a

5.1.1 Optimization of myosin-7a expression

To optimize the purification process of full-length human myosin-7a, we initially designed and cloned a tail truncated myosin-7a construct (M7a-5IQ). Subsequently, the heavy chain with a C-terminal FLAG purification tag was inserted into the pFastBac1 vector and co-expressed with human RLC, calmodulin, and CALML4 in the baculovirus/Sf9 system. The purification outcomes showed that all three light chains co-purified through anti-FLAG affinity resin (**Figure 16**). We have not detected any low molecular weight band on the SDS-PAGE in the absence of any added light chain virus. Additionally, we observed a significant increase in solubility and final concentration of the heavy chain upon the addition of appropriate light chains. Co-expression of a shorter construct that includes the motor and first IQ domains (M7a-S1) with RLC, calmodulin, and CALML4 demonstrated that only RLC co-purified with the heavy chain, indicating a preference of the first IQ motif for RLC (**Figure 17**).

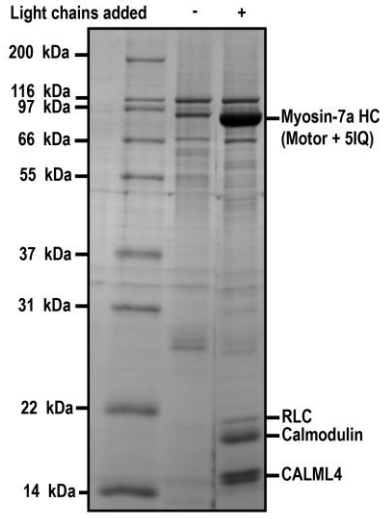

***Figure 16**. SDS-PAGE analysis of purified M7a-5IQ constructs in the absence and presence of additional light chains in the expression.*

Muscle chaperone UNC45b and HSP90 chaperones were additionally included in the expression to enhance solubility of the heavy chain. Previous studies have indicated that these chaperones can assist in the folding of myosin-15, which is a closely related member of myosin-7a and is present in hair cell stereocilia. [93, 94]. The presence of chaperons increased the final protein concentration.

5.1.2 Successful expression and purification of full-length myosin-7a

Our initial efforts to recombinantly produce human myosin-7a from baculovirus infected *Sf*9 cells did not result in soluble, intact protein, and instead we observed the presence of many proteolytic fragments following chromatography over a FLAG affinity column. Co-expressing truncated myosin-7a constructs (M7a-5IQ) with different light chains, we were able to identify multiple light chains co-purifying with myosin-7a heavy chain, hence we engineered a construct using the MultiBac system containing the full-length myosin-7a heavy chain, calmodulin, CALML4 and RLC. This approach ultimately resulted in high yield, purified myosin-7a holoenzyme, with the heavy chain and three types of light chains clearly visible on the gel. The concentrated and dialyzed protein is shown in **Figure 17**.

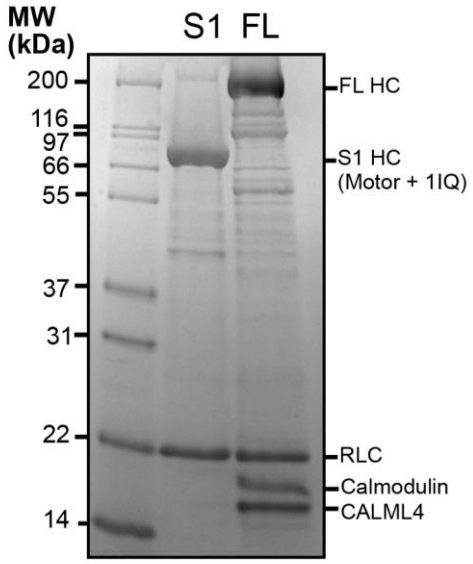

***Figure 17**. SDS-PAGE analysis of purified human myosin-7a-S1 and full-length myosin-7a separated on Novex™ WedgeWell™ 16% Tris-Glycine gel.*

5.1.3 The motor function is regulated by the C-terminal FERM domain

Using negative staining electron microscopy[5], we observed a bent conformation of human myosin-7a at low ionic strength, in which the tail region folds back to contact the motor domain. Previous research on myosin-7a has shown that the last FERM domain is responsible for myosin autoregulation [95]. Increasing the salt concentration resulted in an open conformation, revealing the tail domain's high flexibility (**Figure 18**).

The contour from the probable motor domain-lever junction to the bend point measures 20.7 ± 1.9 nm. This is consistent with the expected length of the lever with 5IQ motifs (~19 nm) [44]. Since the SAH domain is expected to add an additional ~ 9 nm to the lever arm, we speculate that the SAH domain does not contribute to the length of the structure leading up to the bend but rather forms part of the return leg, along with the rest of the tail domain motifs (**Figure 19**).

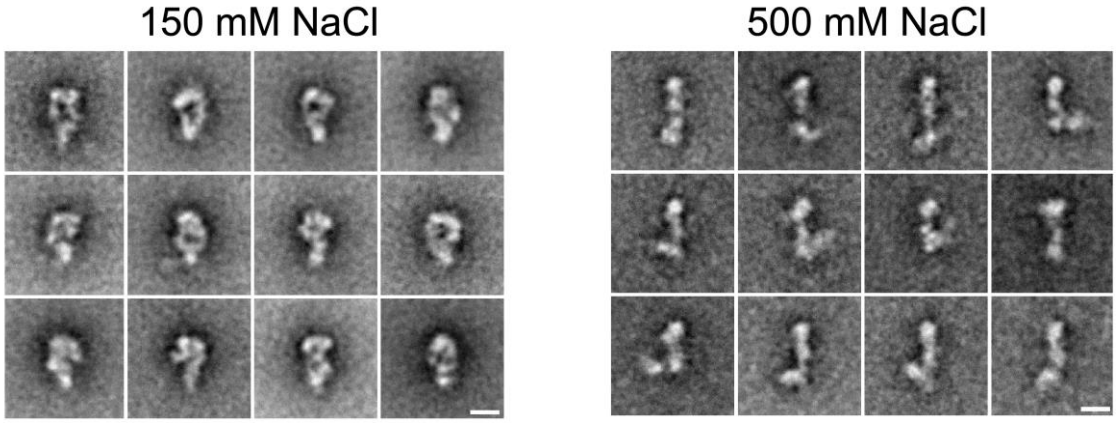

Figure 18*. Class averages of human myosin-7a in electron microscopy in the presence of ATP. We observed the bent conformation of the myosin in low salt condition (left panel). The myosin was forced to open up by increasing the salt concentration (right panel). Scale bar = 5 nm.*

[5] EM imaging and analysis was done by Neil Billington (LMP, NHLBI, NIH) in the NHLBI Electron microscopy Core

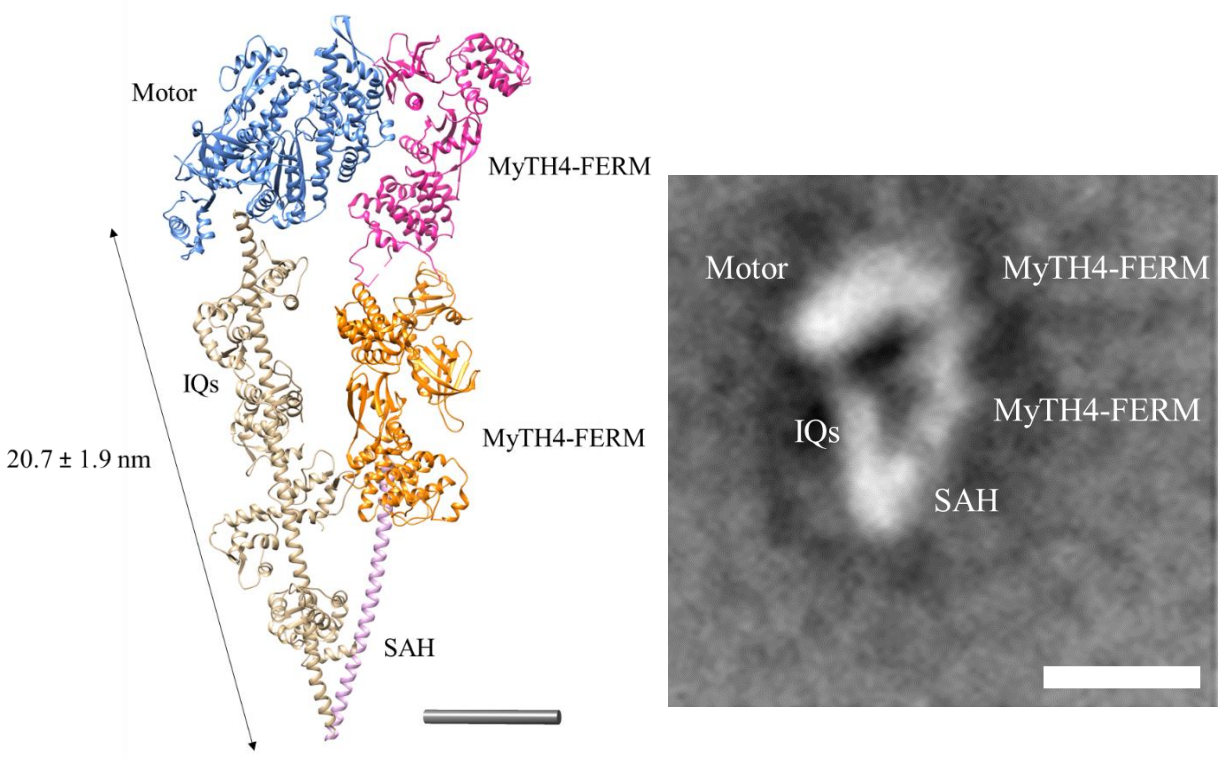

Figure 19. *Left panel: model of myosin-7a autoinhibited structure. This model is for illustrative purpose only, in order to show the relative size of domains within the overall structure. The model is constructed from an AlphaFold structure of the myosin-7a motor domain (blue), a five-IQ lever arm with four light chains bound (1 RLC, 1 CALML4, 2 CaM) on the myosin-5a structure (2DFS.pdb, beige), the myosin-7a SAH domain (5WST.pdb, pink), the myosin-7a first MyTH4-FERM-SH3 module (3PVL.pdb, orange), and the myosin-7a second MyTH4-FERM domain (5MV9.pdb, magenta). Scale bar = 5 nm. Right panel: class average of a full-length myosin-7a in low salt condition. Scale bar = 5 nm.*

The interaction of the tail with the motor domain results in suppression of the enzymatic function. Actin-activated steady-state ATPase activity of myosin-7a-FL was measured by NADH-coupled assay. The maximum extrapolated ATPase rate (v_{max}) was 0.2 s^{-1} with K_{ATPase} of 54 µM. K_{ATPase} approximates the actin affinity to myosin. In contrast, myosin-7a-S1 containing only the motor domain and first IQ domain measured a ~7.5-fold higher maximum ATPase rate at 1.5 s^{-1} and ~5 fold lower at K_{ATPase} 11 µM (**Figure 20**, **Table 7**). The lower K_{ATPase} represents a higher affinity to actin.

In case of *Drosophila* myosin-7a, the v_{max} of both S1 and full-length myosin are very similar at ~ 1 s^{-1}, however the motor and 1Q containing myosin-7a construct has ~40 fold higher affinity to actin [95].

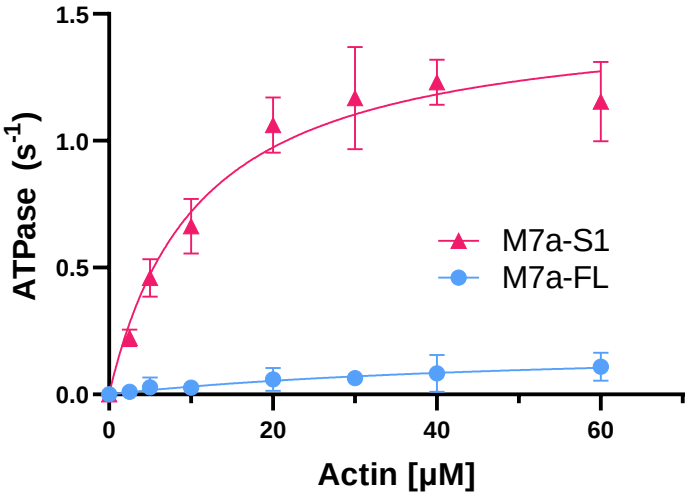

***Figure 20**. Steady-state actin-activated ATPase activity of myosin-7-FL (full-length) and myosin-7a-S1 (motor and first IQ). The autoinhibited full-length myosin-7a has lower ATPase activity and lower actin affinity compared to M7-S1. Mean ± SD, n=4.*

Parameter	*Hs* FL[a]	*Hs* S1[a]	*Dm* FL[b][95]	*Dm* S1[b][95]
v_{max}	0.2 ± 0.11 s^{-1}	1.5 ± 0.1 s^{-1}	1.2 ± 0.4 s^{-1}	1.0 ± 0.1 s^{-1}
K_{ATPase}	54 µM	11 µM	40 µM	1.1 µM

***Table 7**. Summary of steady-state actin-activated ATPase activity results of human myosin-7a based on Michaelis-Menten kinetics, compared with the kinetic parameters of Drosophila myosin-7a.*
a: at 37°C
b: at 25°C

5.1.4 Human myosin-7a is a predominantly expressed as a monomer

Previous studies have shown that the predicted coiled-coil region of myosin-7a is insufficient to form a dimer [33]. To gain insight into the oligomeric state of the myosin-7a holoenzyme, we utilized mass photometry.

Our recombinantly expressed myosin-7a-S1 forms a major mass species of approximately 103 kDa in single molecule mass photometry experiments, most closely matching the sum of one heavy chain (~89 kDa) plus one light chain (RLC, ~20 kDa) (**Figure 21**).

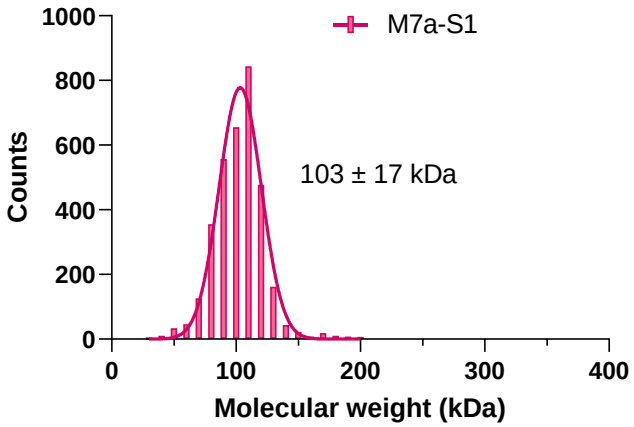

***Figure 21**. Single-molecule mass photometry reading of myosin-7a-S1. The holoenzyme forms a monomer peak at 103 ± 17 kDa consisting of a heavy chain and single light chain.*

Full-length myosin-7a forms a 325 kDa major mass species, matching the sum of one heavy chain (~255 kDa) plus four of the three types of light chains (RLC: ~20 kDa, calmodulin and CALML4: ~17 kDa) indicating that the full-length myosin is a monomer with respect to heavy chains (**Figure 22**). No distinct peak was observed at a position that would correspond to dimer (or other multimer).

In contrast, artificially dimerized myosin-7a-S1SAH (myosin-7a motor and neck domain followed by a Leucine Zipper motif) formed a major mass species of approximately 406 kDa, matching the sum of two heavy chains (~141 kDa) plus six to eight light chains (**Figure 23**). The resolution of mass photometry does not allow us to provide an exact number of light chains.

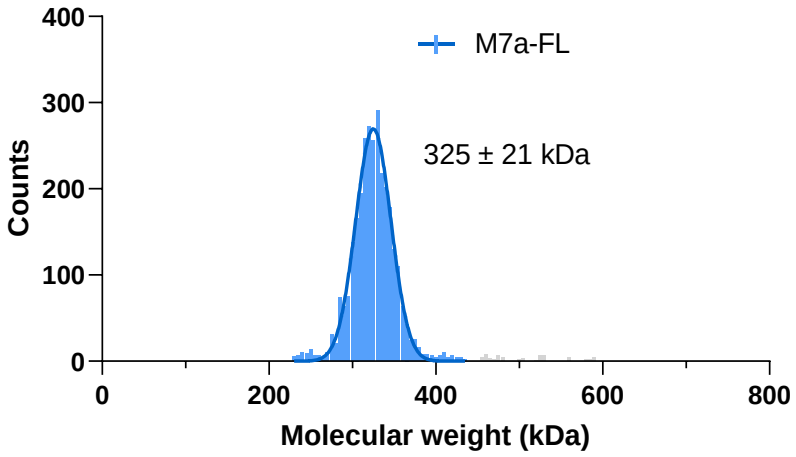

Figure 22. *Single-molecule mass photometry reading of full-length myosin-7a. The holoenzyme forms a monomer peak at 325 ± 21 kDa consisting of a heavy chain and multiple light chains.*

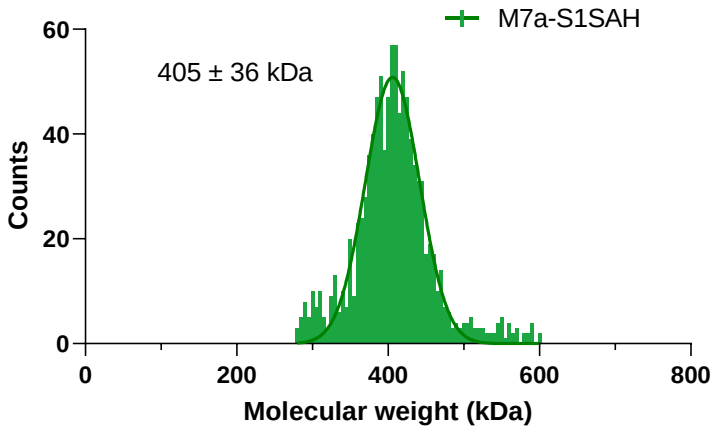

Figure 23*. Single-molecule mass photometry reading of myosin-7a-S1SAH Zipper. The holoenzyme forms a dimer peak at 405 ± 36 kDa consisting of two heavy chains and six to eight light chains.*

5.2 Molecular details of light chain composition of myosin-7a

5.2.1 CALML4 is a critical light chain for myosin-7a

CALML4 was recently identified as an endogenous light chain for myosin-7b and a putative light chain for myosin-7a [41]. The initial quality of protein expressed in *Sf9* cells was significantly improved by co-expressing CALML4 with full length human myosin-7a heavy chain. The increased yield and decreased fragmentation by proteolysis suggested that CALML4 binds to myosin-7a and potentially protects the previously exposed neck region. Anti-CALML4 antibody and mass spectrometry were used to confirm the presence of CALML4 in purified myosin-7a samples (**Figure 24**).

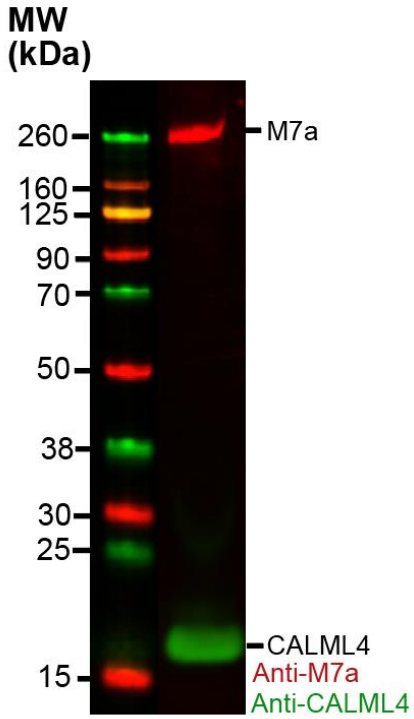

***Figure 24**. Immuno-blot analysis of purified myosin-7a-FL with anti-M7a (red) and anti-CALML4 (green) antibodies.*

We also discovered that calmodulin co-purified with our 5IQ constructs only when CALML4 was present, implying that CALML4 recruits calmodulin binding to an adjacent IQ. This hypothesis is supported by the recruitment of endogenous *Sf9* calmodulin by CALML4 as detected on SDS-PAGE after purification from experiments

where no exogenous calmodulin was either co-expressed or added to the cell lysate (**Figure 25**).

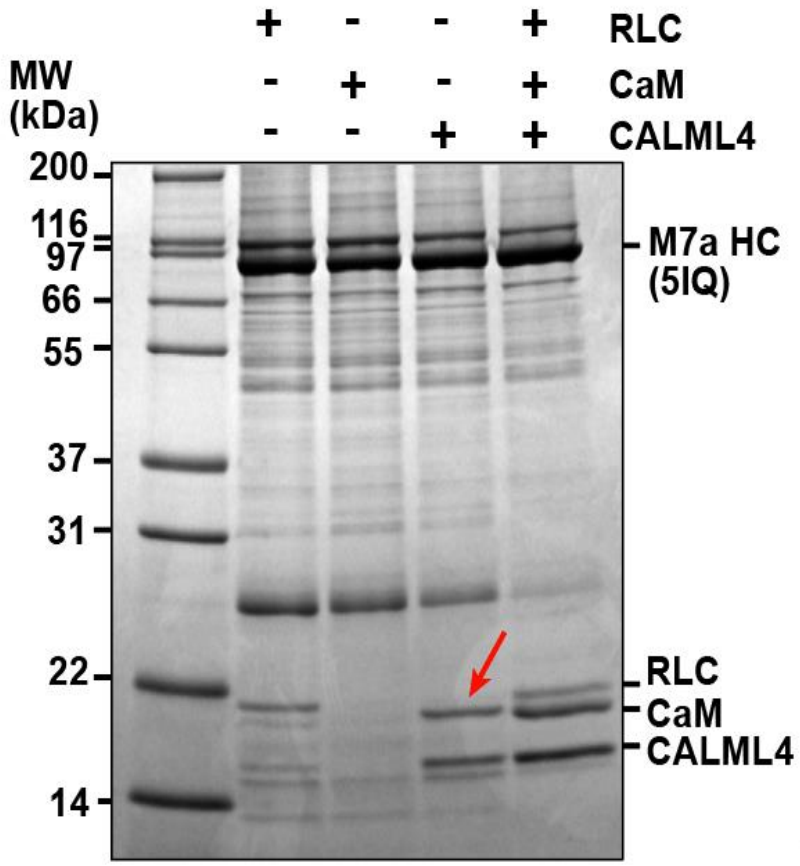

***Figure 25**. SDS-PAGE analysis of myosin-7a-5IQ constructs co-expressed with different light chain candidates. The red arrow indicates endogenous Sf9 Calmodulin.*

5.3 Calcium regulation of myosin-7a

5.3.1 CALML4 does not demonstrate a calcium-dependent shift

Calmodulin and certain calmodulin-like proteins are able to bind calcium through their EF-hand motifs [96]. Calmodulin and CALML4 are 44% identical. When the amino acid sequence of CALML4 is compared to that of human calmodulin, crucial amino acids required for Ca^{2+} chelation are absent in each of the EF-hands of CALML4 (**Figure 26**).

***Figure 26**. Amino acid sequence of human Calmodulin and CALML4. The blue brackets and underscored amino acids indicate the EF hands motifs, the red amino acids are identical, while the yellowed amino acids are crucial for cation binding.*

The presence of some conserved amino acids in the 4th EF of CALML4 hand suggests it might retain the ability to bind calcium. Therefore, we performed an electrophoretic mobility shift assay using purified calmodulin and CALML4 to directly investigate CALML4's calcium binding capability. Calmodulin exhibited altered electrophoretic mobility upon incubation with Ca^{2+}, as it undergoes calcium dependent conformational changes that are known to be detectable in SDS PAGE as an increase in mobility [88]. However, under the same conditions, the mobility of the CALML4 samples remained unchanged following addition of calcium (**Figure 27**).

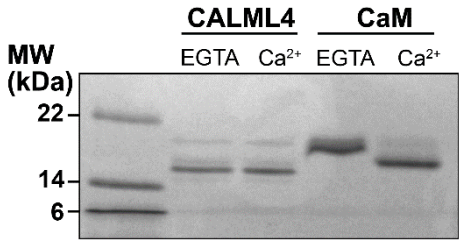

***Figure 27**. SDS-PAGE analysis of electrophoretic mobility shift assay of purified CALML4 and Calmodulin samples. The individual samples were incubated in the presence of 1 µM EGTA or 1 µM $CaCl_2$ then run on Novex™ WedgeWell™ 16% Tris-Glycine gel.*

5.3.2 CALML4 binds calcium with low affinity

To investigate calcium-induced changes, we conducted ITC experiments targeting CALML4 using 8 mM Ca^{2+} (**Figure 28**). The data fitting pointed out a potential binding (K_A = 700 ± 1730 M^{-1}). Nevertheless, the abnormally high standard deviation and an unrealistic binding stoichiometry ($N_{CALML4\text{-}Calcium}$ = 5.56 ± 3.23; while $N_{CaM\text{-}Calcium}$ = 4) raise doubts about the binding event's veracity.

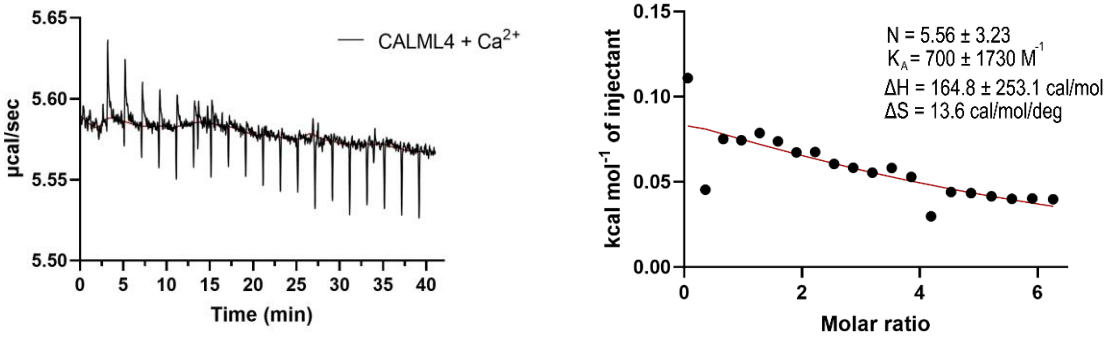

***Figure 28**. Left panel: calorimetric titration affinity measurement of CALML4 for calcium. Right panel: isotherm of calcium-CALML4 binding that were fit to a single binding site model*

MicroScale Thermophoresis (MST) was used to monitor calcium induced changes in CALML4 molecular hydration shell, charge, or size. In the range of 10^{-2} M (10 mM) to 10^{-5} M (10 µM) calcium, CALML4 samples displayed less binding affinity binding to calcium when compared to calmodulin (**Figure 29, Figure 30**). By using 1 M calcium concentration, CALML4 calcium affinity was estimated at K_D = ~ 350 mM through sigmoidal fitting. These findings result that CALML4 is an EF-hand protein that has lost its capacity to bind to Ca^{2+} under physiologically relevant conditions.

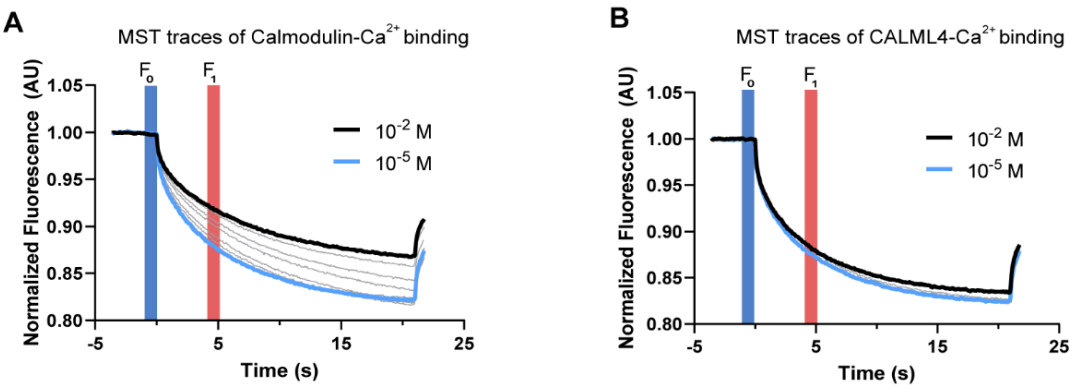

***Figure 29**. MST traces of calmodulin (left) and CALML4 (right) calcium titration binding assay. The black line is 10^{-2} M while the blue line is 10^{-5} M calcium concentration. F_0 indicates the fluorescence in the cold state prior to IR laser activation and F_1 is the fluorescence value measured in the heated state.*

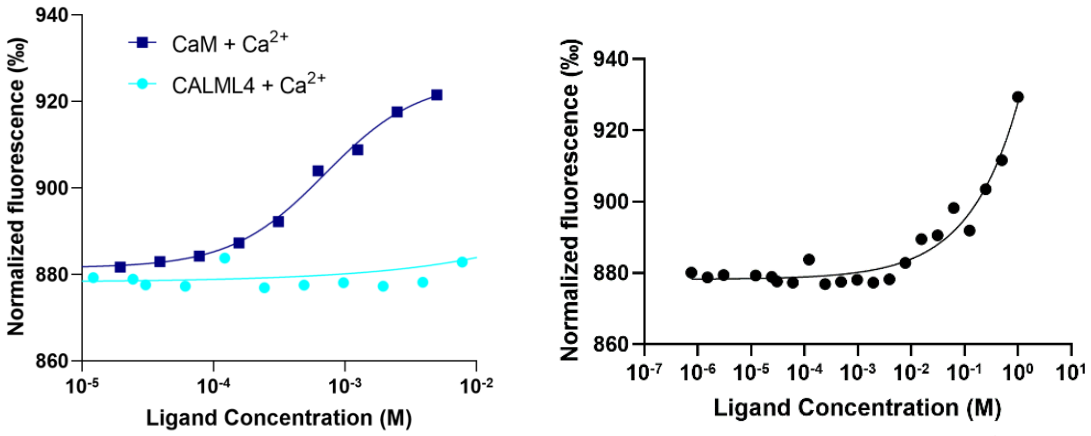

***Figure 30.** Left panel: sigmoidal binding affinity fit of calmodulin (dark blue squares) and CALML4 (light blue circles) in physiological calcium concentrations. Right panel: sigmoidal binding affinity fit of CALML4 calcium titration.*

5.3.3 Light chain binding of full-length myosin-7a is calcium-dependent

Using mass photometry, we were also able to visualize changes within the holoenzyme. In 1 µM EGTA conditions, full-length myosin-7a construct exhibited a major mass of 325 kDa, corresponding to one heavy chain and four light chains (**Figure 22**). Upon the addition of calcium, we observed a shift towards a smaller mass peak at 293 ± 25 kDa, which corresponds to one heavy chain plus an extra 38 kDa (**Figure 31**). Given that RLC

and CALML4 are inert to calcium, we attribute this 38 kDa mass to the combined presence of one RLC and one CALM4. The mass photometer does not detect proteins less than 25 kDa and thus any dissociated, free light chains in this experiment are not detected.

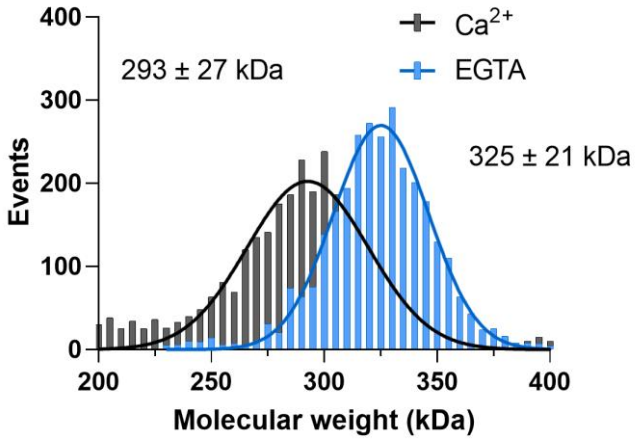

Figure 31. *Single molecule mass photometry readings of light chain dissociation. Samples were incubated in the presence of 1 µM EGTA and 1 µM calcium, respectively.*

5.3.4 Calcium influences ATPase activity and actin affinity of myosin-7a

Since calcium binding seems to promote light chain dissociation from the holoenzyme, we investigated its effect on the enzymatic activity. NADH-coupled ATPase assay was repeated with 500 nM Ca^{2+} in the reaction. Following the addition of calcium, the maximum extrapolated ATPase rate of myosin-7a-FL increased to 0.98 ± 0.27 s^{-1} (**Figure 32**, **Table 8**). A similar increase has been described for *Drosophila* full length myosin-7a as well [97].

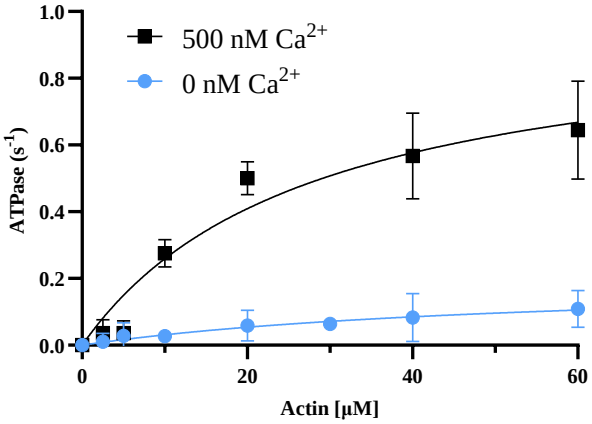

***Figure 32**. Steady-state actin-activated ATPase activity of full-length myosin-7a. The autoinhibited conformation of myosin-7a-FL is alleviated by the addition of calcium. Mean± SD, n=4.*

Human full-length myosin-7a		
Parameter	- Ca^{2+}	+ Ca^{2+}
$\mathbf{v_{max}}$	0.2 ± 0.11 s^{-1}	0.98 ± 0.27 s^{-1}
$\mathbf{K_{ATPase}}$	55 µM	27 µM

***Table 8**. Summary of steady-state actin-activated ATPase activity results of human myosin-7a in the absence and presence of calcium based on Michaelis-Menten kinetics.*

5.3.5 Actin gliding velocity decreases in the presence of calcium

We carried out an *in vitro* actin gliding assay using TIRF microscopy to examine the impact of calcium on the myosin's motor activity. The surface-bound myosin molecules moved the fluorescently labeled actin at ~ 22 nm/s. However, in the presence of calcium the gliding velocity decreased to ~ 7 nm/s (**Figure 33**), suggesting that the myosin's motility is compromised as a result of calmodulin dissociation from the holoenzyme even though free calmodulin was present in the assay.

We hypothesize that light chain dissociation occurs because the calcium-binding calmodulin light chains disassociate from the heavy chain since we have seen mass reduction upon calcium addition in mass photometry. The myosin's neck region, and

therefore its lever arm rigidity, is altered, and the motor is unable to drive actin filaments as effectively as it would if its neck region was fully decorated with light chains.

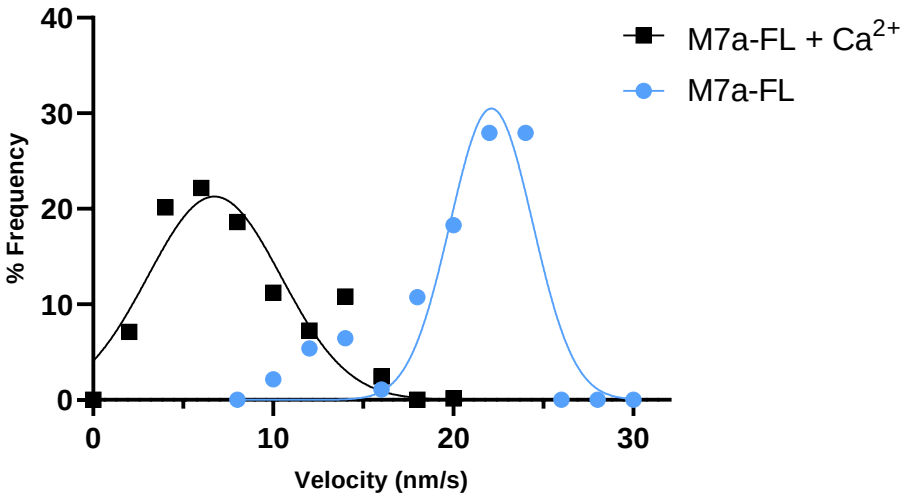

***Figure 33**. In vitro actin gliding assay of myosin-7a-FL in the presence or absence of Ca^{2+}.*

5.4 N-terminal extension regulates the location and activity of myosin-7a

The cochlea expresses two isoforms of the myosin-7a heavy chain, differing by eleven amino acids at the N-terminus. The canonical long-N-terminal isoform contains these amino acids which are not found in the short N-terminal isoform [37].

To explore this hypothesis further, we purified the two isoforms and examined the role of the N-terminal extension in myosin-7a's function. We engineered constructs containing the motor domain and the 5IQ motifs (M7a-5IQ), but no tail to avoid the complication of tail-dependent autoinhibition. Additionally, the common use of an N-terminal GFP-tag on myosin-7a [40, 45, 51, 98] raises questions about its potential impact on the regulation by the N-terminal extension. We therefore also engineered a long N-terminal construct that includes a GFP moiety before the N-terminal (**Figure 34**), in addition to the full-length proteins.

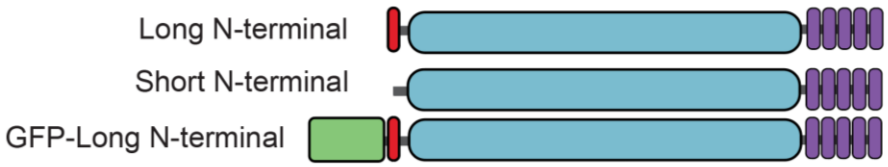

Figure 34*. Graphical representation of myosin-7a-5IQ constructs with differing N-terminals.*

In an *in vitro* actin gliding assay, the canonical long isoform displayed higher gliding velocity (3 ± 1.6 nm/s) compared to the short isoform (1.3 ± 0.95 nm/s) (**Figure 35**). Similar results were noted in a steady state ATPase assay, where the actin-activated ATPase activity of the longer isoform was determined to be higher (0.84 ± 0.14 s^{-1}) than the shorter isoform (0.24 ± 0.06 s^{-1}) (**Figure 36**). The kinetic parameters are summarized in **Table 9**. Interestingly, the presence of an N-terminal GFP moiety on the long isoform also resulted in lower velocity values (1.6 ± 0.9 nm/s) and lower ATPase activity (0.11 ± 0.07 s^{-1}) compared to the untagged long N-terminal isoform.

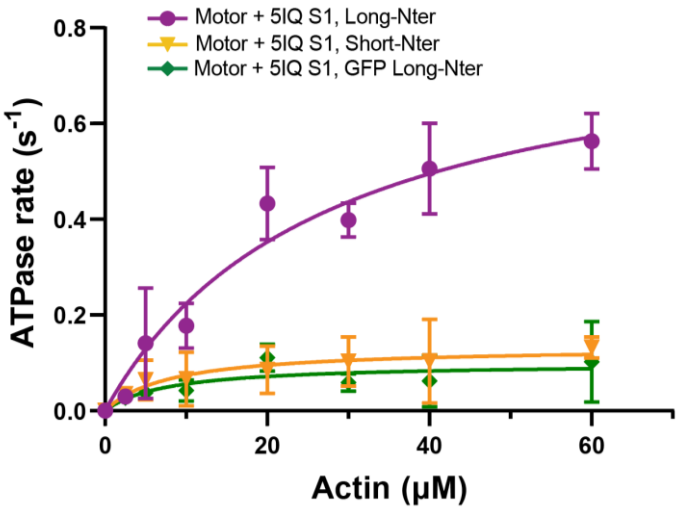

***Figure 35**. Steady-state actin-activated ATPase activity of different myosin-7a-5IQ constructs. Mean ± SD, n=4. The kinetic parameters are summarized below in Table 9.*

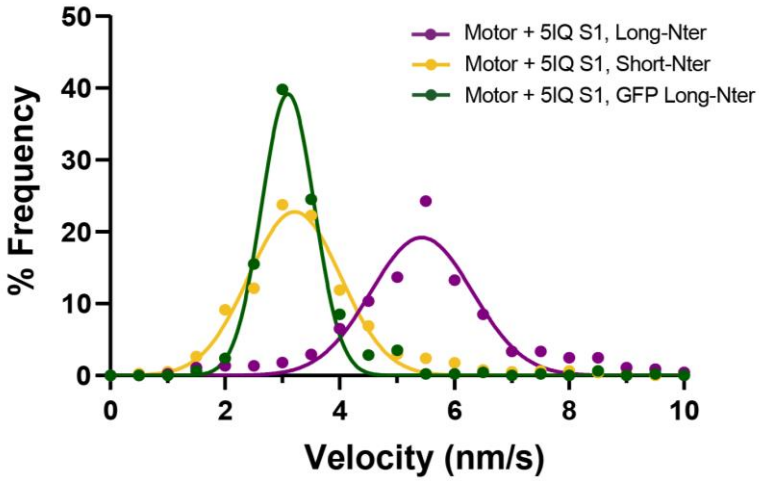

***Figure 36**. In vitro actin gliding assay of different myosin-7a-5IQ constructs. The kinetic parameters are summarized below in Table 9.*

	Long N-terminal	**Short N-terminal**	**GFP-Long N-terminal**
$\mathbf{v_{max}}$	0.83 ± 0.14 s^{-1}	0.13 ± 0.06 s^{-1}	0.1 ± 0.07 s^{-1}
$\mathbf{K_m}$	27 µM	8 µM	8 µM
Velocity	3 ± 1.6 nm/s	1.3 ± 0.95 nm/s	1.6 ± 0.9 nm/s

***Table 9**. Summary of the kinetic parameters of the long and the short N-terminal isoforms. Steady-state actin-activated ATPase activity results based on Michaelis-Menten kinetics. All measurements were carried out at 37°C.*

5.5 Motile properties of human myosin-7a

5.5.1 Artificially dimerized tail-less myosin-7a moves processively

The predicted coiled-coil region in myosin-7a forms a stable single alpha helix motif that acts as an extension of the lever arm. We introduced a leucine zipper motif after the SAH motif and omitted the tail domains making a tail-truncated but stable dimerized motor. This construct also contained a GFP-moiety at the N-terminal. As shown in **Figure 23**, GFP-myosin-7a-S1SAH-Zipper in mass photometry reading forms a major mass peak that is consistent with a dimer.

In order to study the mechanistic details of the myosins intrinsic processivity, we utilized single molecule *in vitro* motility assay, in which we were able to observe the processivity of individual myosin molecules using TIRF microscopy (**Figure 37**). The rhodamine phalloidin labelled actin filaments were immobilized on the surface. GFP-myosin-7a-S1SAH-Zipper was washed into the chamber then the motility of the motor proteins was initiated by adding ATP. In the presence of 150 mM NaCl and 5 mM ATP, dimerized myosin-7a moved along the surface-bound actin filaments. Using FiJi TrackMate, detailed motility characterization revealed that myosin-7a moves slowly on actin filaments (~ 4.2 nm/s) while maintaining attachment for a long duration (136 s) and traveling a long distance (379 nm) (**Figure 38**).

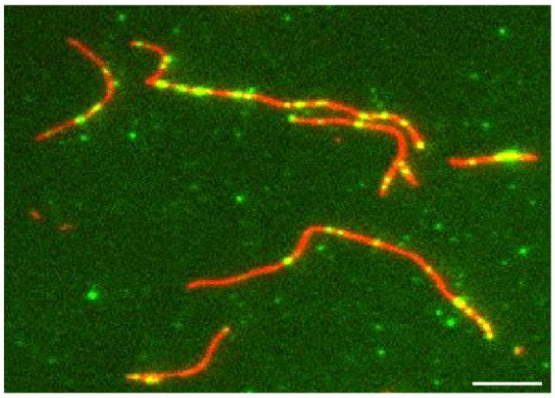

Figure 37. *Single frame of TIRF view of GFP-myosin-7a-S1SAH-Zipper (green) in single molecule in vitro motility assay. Actin is labeled with rhodamine phalloidin (red). Scale bar = 10 µm.*

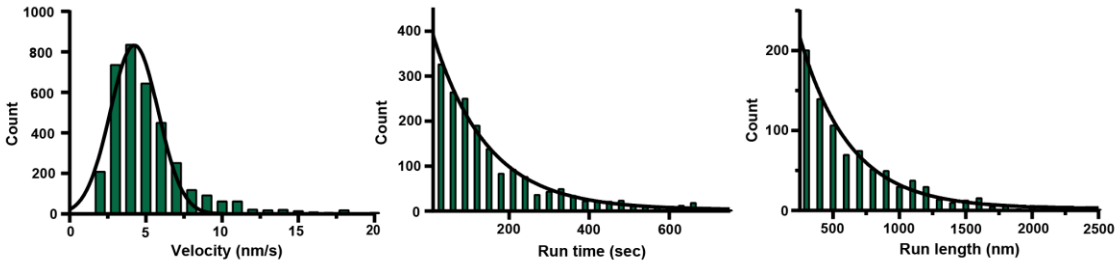

***Figure 38**. Frequency distribution histogram of velocity (4.2 ± 1.5 nm/s), characteristic run time (136 s) and run length (379 nm) of GFP-myosin-7a-S1SAH-Zipper on a surface bound actin filament in single molecule motility assay.*

Previous studies have investigated the processivity of dimerized myosin-7a in cell cultures, but not in ARPE19 cells, which are a human retinal pigment epithelium (RPE) cell line [36]. Following transient transfection of ARPE19 cells with the dimerized construct, we observed abundant filopodia formation, the GFP-tagged motor moved along the filopodia and accumulated at the tips (**Figure 39**, **Figure 40**).

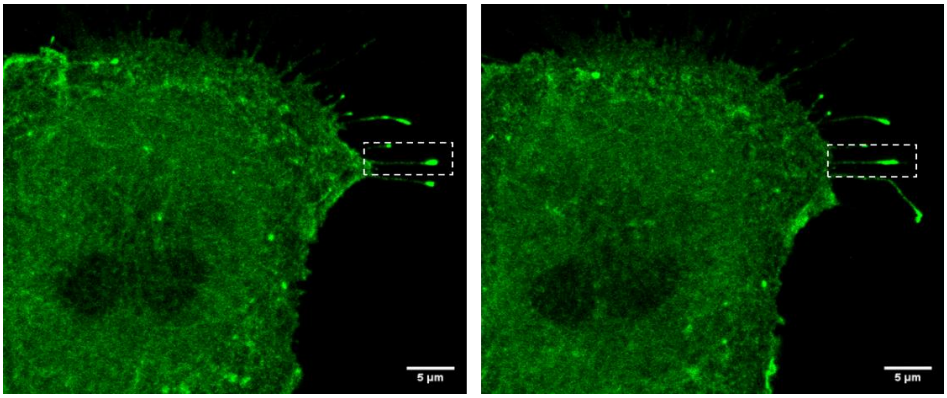

***Figure 39**. Airyscan live-cell imaging of ARPE-19 cells transfected with GFP-tagged myosin-7a-S1SAH-Zipper. The white boxed regions show a single filopodium in which the GFP-tagged motor moves backwards toward the cell body. The cells were observed 48 hours after transfection.*

By manual tracking the moving molecules using FiJi, we were able to measure the velocity of the dimerized constructs. The average speed (n = 5) of the moving GFP-myosin-7a-S1SAH-Zipper was 10 nm/s.

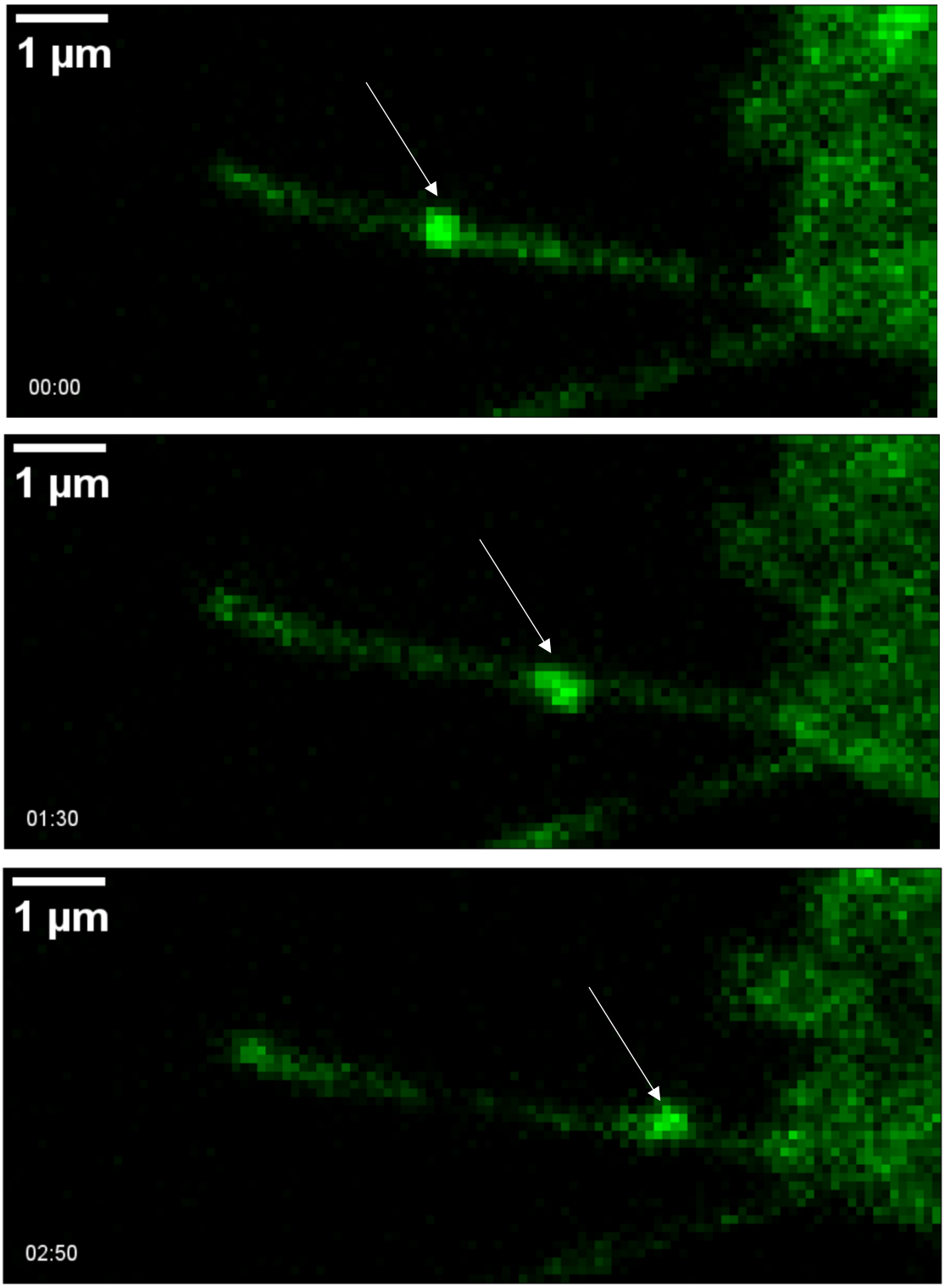

***Figure 40**. Timeframes from an Airyscan live-cell image recording of ARPE-19 cells transfected with GFP-tagged myosin-7a-S1SAH-Zipper. The white arrow indicates the moving motor proteins.*

5.5.2 Recombinant MyRIP is a monomeric, globular protein

MyRIP has been shown to promote processivity of myosin-7a in cellular environment [45, 58, 68]. As our recombinant myosin-7a is in a monomeric, autoinhibited state *in vitro* (**Figure 18**, **Figure 22**), a binding partner might be able to activate the motor. In order to study their molecular interaction, we expressed and purified recombinant mCherry-tagged MyRIP.

Full-length MyRIP with an N-terminal mCherry-tag and C-terminal FLAG purification tag (mCherry-MyRIP) was cloned into pFastBac vector and expressed in the baculovirus/*Sf9* system, and then anti-FLAG affinity purified. The concentrated and dialyzed protein is shown in **Figure 41**. We observed a secondary stronger band at ~70 kDa height, which we hypothesize as HSP70 chaperone protein.

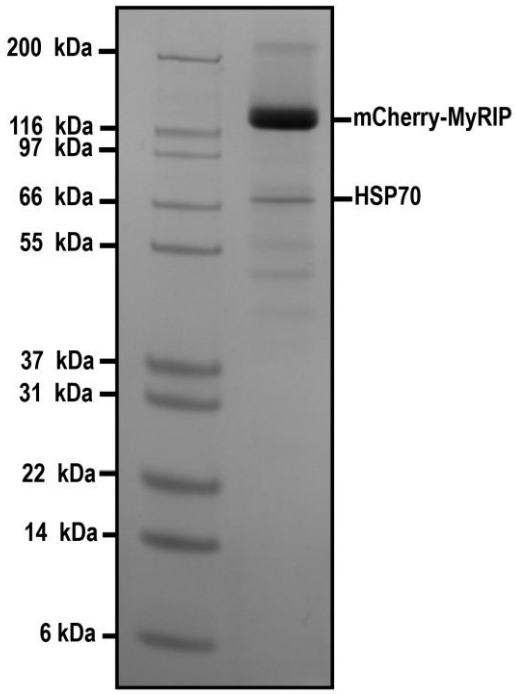

***Figure 41**. SDS-PAGE analysis of mCherry-MyRIP purification from Sf9 cells using FLAG affinity chromatography.*

Electron microscopy images[6] revealed MyRIP as a monomeric globular protein (**Figure 42**), which was further confirmed in mass photometry readings. The major mass peak at 117 kDa most closely matches an mCherry-tagged MyRIP monomer (~120 kDa) (**Figure 43**).

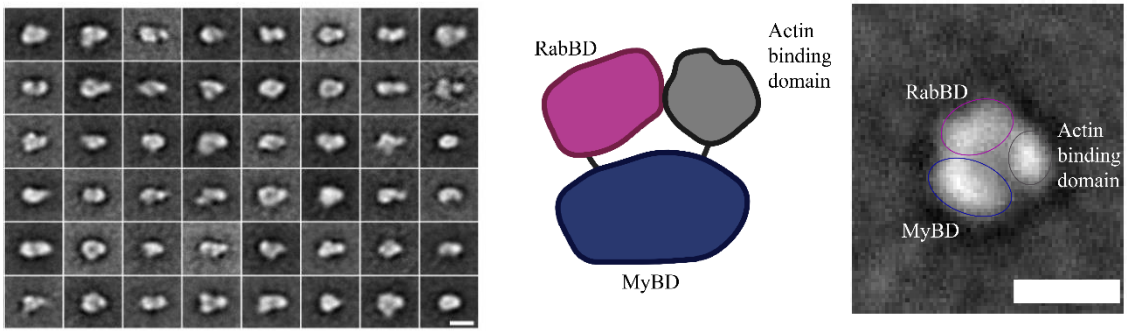

***Figure 42**. Left panel: class averages of mCherry-MyRIP in electron microscopy, scale bar = 5 nm. Right panel: comparison of MyRIP structure to class averages of electron microscopy, scale bar = 5 nm.*

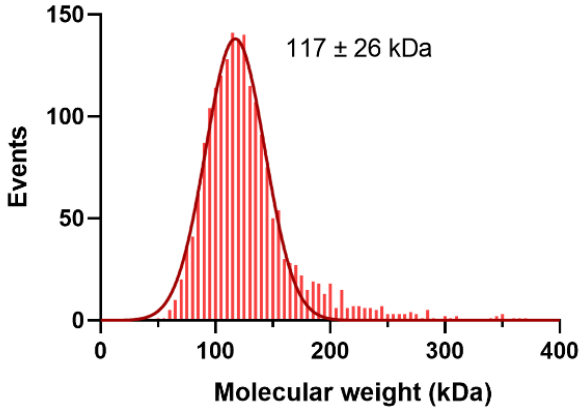

***Figure 43**. Left panel: single molecule mass photometry readings of mCherry-MyRIP.*

5.5.3 MyRIP binding enables myosin-7a processivity

Similarly to *Drosophila* myosin-7a [30], cell culture data indicated that human myosin-7a becomes processive in the presence of dimerizing binding partner. MyRIP-induced activation of myosin-7a in ARPE19 cells has been observed before [45].

[6] EM imaging and analysis was done by Neil Billington at the NHLBI Electron microscopy Core, NIH

Using a single molecule *in vitro* motility assay in TIRF microscopy to investigate the mechanistic details of myosin-7a processivity, we found that full-length myosin-7a alone is not processive; however, it becomes processive in the presence of MyRIP. mCherry tagged MyRIP co-localized with full-length myosin-7a and traveled together along the actin-filament network (**Figure 44**).

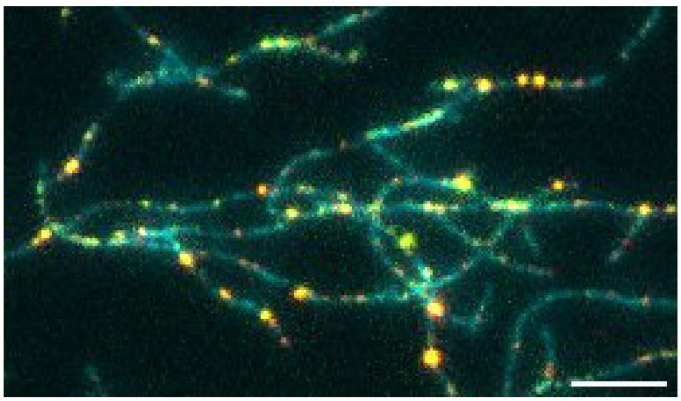

Figure 44. *Single frame of TIRF view of myosin-7a-FL (green) and mCherry-MyRIP (red) in single molecule in vitro motility assay. Actin is labeled with Alexa-Fluor 647 (blue). Scale bar = 10 µm.*

Detailed motility characterization shows that the motor-adaptor complex moves on actin slowly at approx. 7.8 nm/s. The characteristic run length was 552 nm and the actin attachment time was around 156 s (**Figure 45**). At higher concentrations (~ 1 µM myosin-7a and ~ 1 µM MyRIP), we observed the clustering of moving molecules. Several fluorescent molecules were traveling together, indicating the formation complexes containing a higher number of molecules (**Figure 46**).

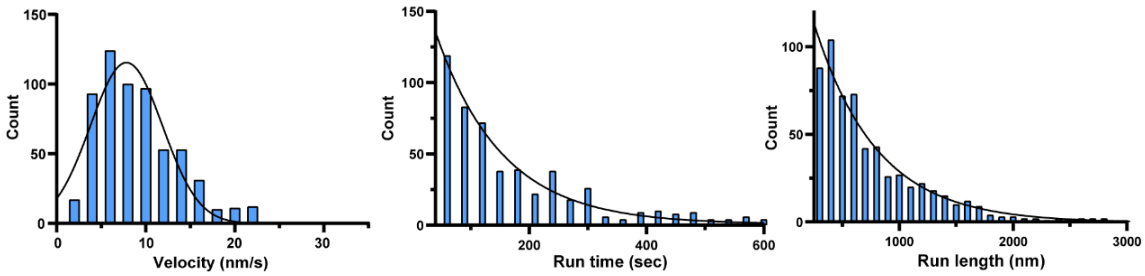

Figure 45. *Frequency distribution histogram of velocity (7.8 ± 4 nm/s), characteristic duration time (156 s) and run length (552 nm) of myosin-7a and MyRIP on a surface bound actin filament in single molecule motility assay.*

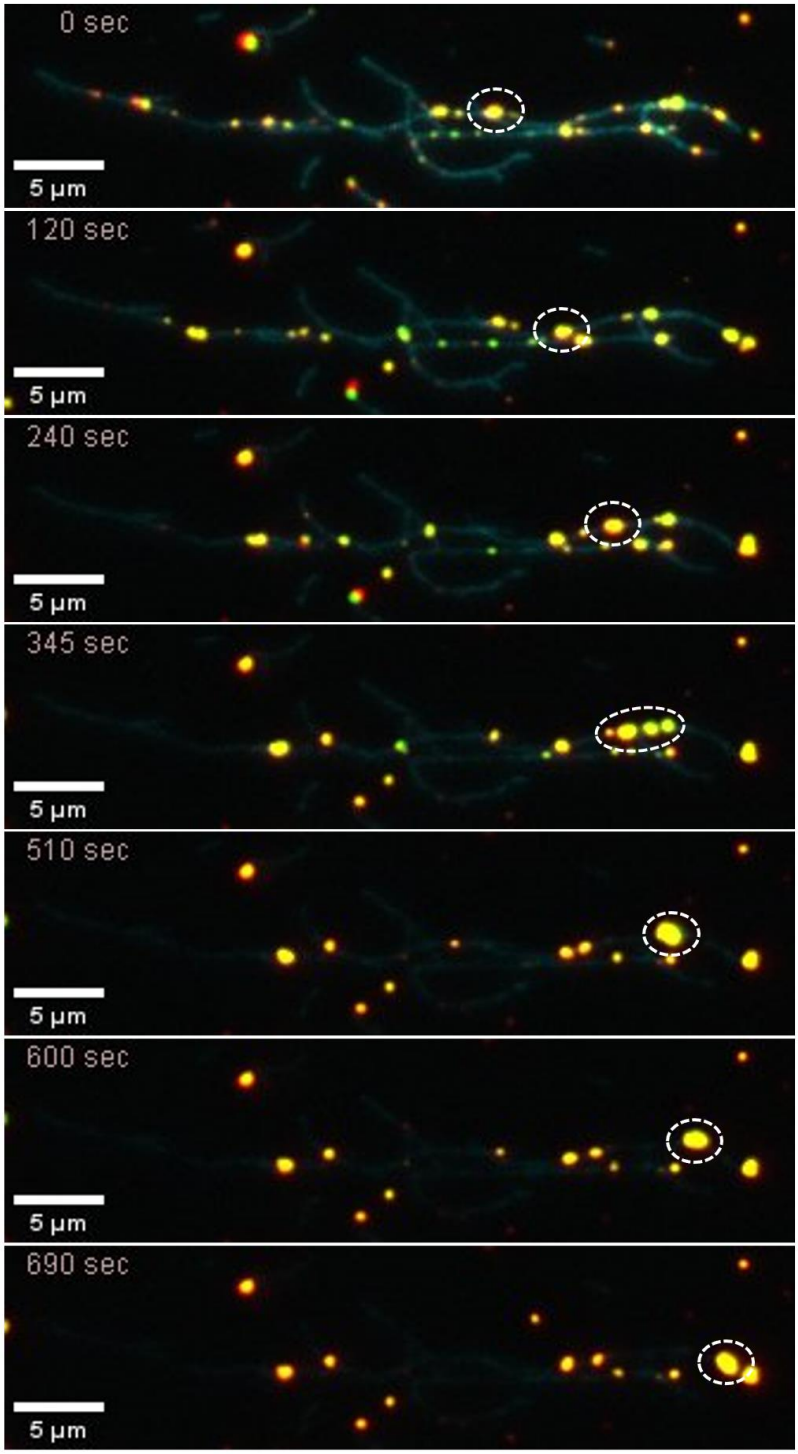

***Figure 46**. Single frames of TIRF recording of myosin-7a-FL (green) and mCherry-MyRIP (red) in single molecule in vitro motility assay. The circled dot seems to contain multiple myosin-7a and MyRIP. The motor-cargo complex moves together along the actin filament then merges with several other complexes. The newly formed super-complex moves further along the actin filament.*

Our observations are also in good correlation with previously reported *Drosophila* data [30]. The kinetic parameters of our constructs and previously recoded processivity is summarized in **Table 10**.

Parameter	Human full-length M7a with MyRIP	*Drosophila* full-length M7a with M7BP[a]	Human S1SAH-Zipper M7a	Human S1SAH-Zipper M7a[b]
Velocity	7.8 ± 4.2 nm/s	7.7 ± 4.4 nm/s	4.3 ± 1.5 nm/s	11 ± 0.6 nm/s
Characteristic run length	552 nm	350 nm	378 nm	710 nm

Table 10*. Comparison of human and Drosophila myosin 7a single molecule motility. a: [30], b: [36]*

To further study this interaction, ARPE19 cells were transiently transfected with GFP-tagged full-length myosin-7a. The GFP signal showed diffuse localization of the myosin throughout the cells (**Figure 47**). The diffused localization of the full-length protein indicates that the motor is in an auto-inhibited state as opposed to the case of the artificially dimerized myosin-7a, when the motor was observed to move to the tips of the filopodia without the presence of a binding partner. Transfecting the cells with mCherry-MyRIP, MyRIP localizes along the actin cytoskeleton and we also observed red coloration on small moving vesicles (**Figure 47**). Immuno-blot analysis revealed that ARPE19 cells do not express endogenous myosin-7a or MyRIP at a detectable level. When mCherry-MyRIP and GFP-tagged full-length myosin-7a were co-transfected in ARPE19 cells, abundant filopodia formation was observed and the motor-adaptor complex moved to the tips of the filopodia (**Figure 48).**

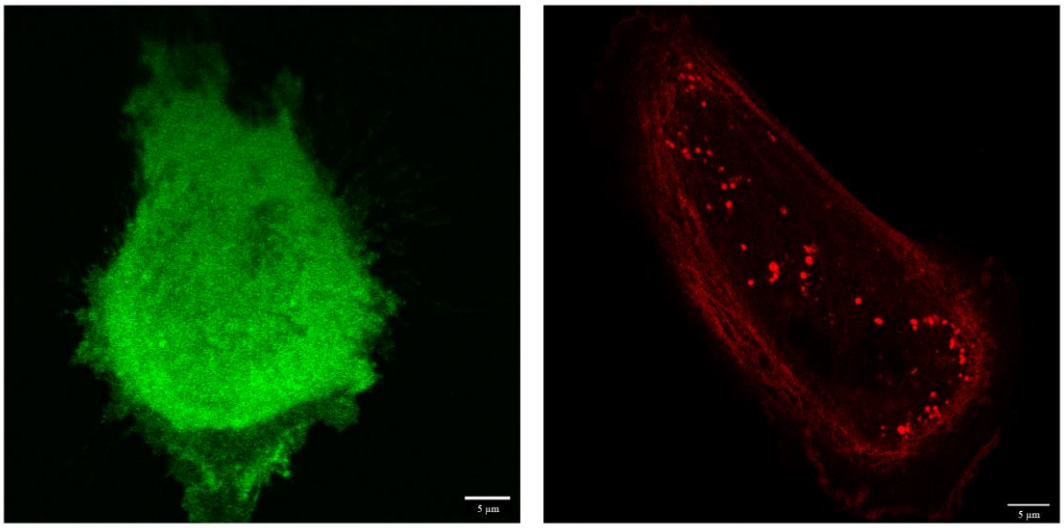

***Figure 47**. Airyscan live-cell imaging of ARPE-19 cells transfected with GFP-tagged full-length myosin-7a (left) alone or together with mCherry-MyRIP (right). The cells were observed 48 hours after transfection.*

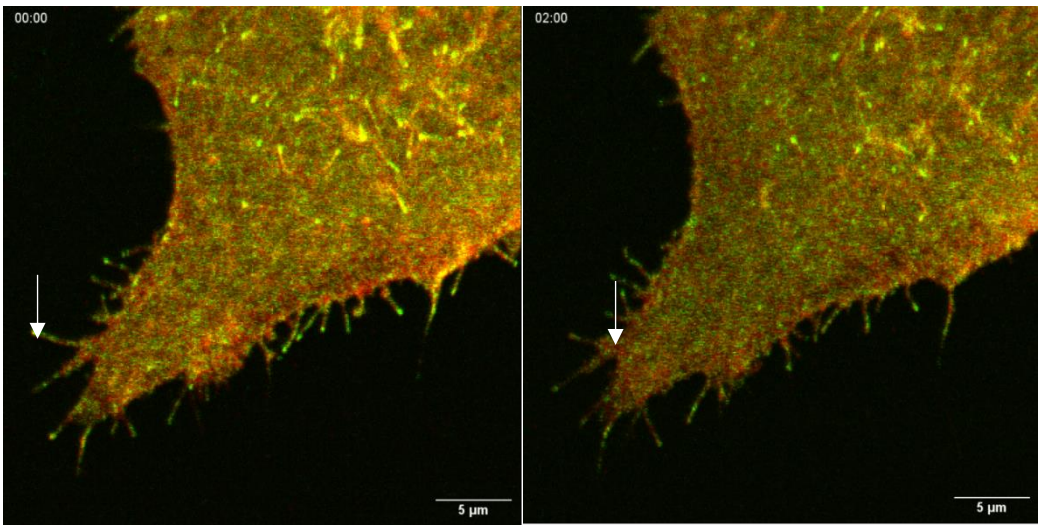

***Figure 48.** Timeframes of Airyscan live-cell imaging of ARPE-19 cells co-transfected with GFP-tagged full-length myosin-7a and mCherry-MyRIP. The white arrow indicates the moving motor-adaptor complex.*

5.5.4 MyBD is not sufficient to promote myosin-7a processivity

The myosin-binding domain (MyBD) with C-terminal FLAG purification tag was cloned into pFastBac vector and expressed in the baculovirus/*Sf9* system, and then anti-FLAG

affinity purified. The concentrated and dialyzed protein is shown in **Figure 49**.

In our investigation of whether MyBD can induce myosin-7a processivity, we utilized a single molecule in vitro motility assay in TIRF microscopy. Our findings indicate that full-length myosin-7a is not processive in the presence of MyBD alone.

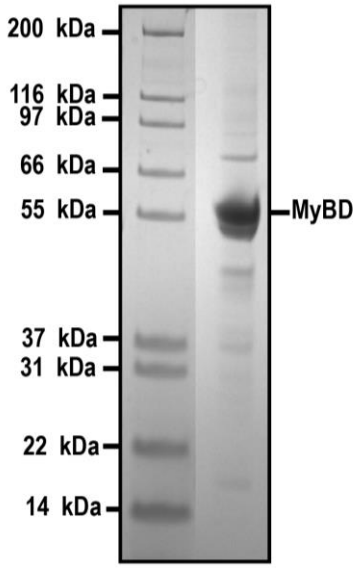

***Figure 49**. SDS PAGE analysis of MyBD purification from Sf9 cells using FLAG affinity chromatography*

6 Discussion

In order to function efficiently, a motor protein requires multiple regulatory mechanisms. Human myosin-7a has been the subject of research for many years, but several questions remain unanswered due to the complexities associated with obtaining a high-quality holoenzyme. In this study, we aimed to examine the intra- and intermolecular regulations that adjust the activity, conformation, oligomeric state, intracellular localization, and overall function of human myosin-7a.

6.1 Molecular details of light chain composition of myosin-7a

Recombinant human myosin-7a was expressed in a baculovirus/*Sf9* system and purified via FLAG affinity. By expressing constructs containing varied numbers of IQ motifs with different light chains, we successfully unveiled the light chain composition of the myosin-7a complex. Human myosin-7a prefers calmodulin and calmodulin-like protein *in vitro*, while it also binds to regulatory light chains. The exact endogenous light chain composition, as well the order of light chains along the neck region of myosin-7a, however require further elucidation. Nevertheless, the recent discovery of CALML4 as an endogenous light chain for myosin-7b, as well as its presence in the inner ear, implies that it may also function as an endogenous light chain for myosin-7a. Endogenous calmodulin was picked up from the *Sf9* cells during expression, which strengthens the possibility of being a natural light chain in the human cells as well, because the human and the *Spodoptera frugiperda* calmodulin has 98% identity.

Structural analysis of myosin showed that it is predominantly monomeric *in vitro*, and under low ion conditions, EM images showed a bent structure. Similarly to *Drosophila* myosin-7a, the tail folds back onto the motor domain, creating a compact, autoinhibited structure [30]. Truncation of the tail domain at specific motifs leads to elevated ATPase activity, and deletion of the second evolutionarily conserved FERM domain is sufficient to diminish autoinhibition [95].

In accordance with the EM images, mass photometry measurements also proves that the full-length myosin is a monomer with respect to heavy chains. The peak of the distribution corresponds best to a lever with four light chains bound. It should be noted that the mass photometry is unable to resolve multiple populations differing by the mass of one or two light chains. In scenarios where myosin has a mixture of light chain occupancies (e.g., 4 and 5 light chains), it is not possible to determine the exact proportion of each using mass photometry. The autoinhibited conformation, in which the fifth IQ motif may be compromised and unable to bind a light chain, results in the mass photometry histogram showing a holoenzyme with four light chains bound, as indicated by the Gaussian fit.

Myosin-7a-S1 displayed a distinct peak at 103 kDa, which corresponds most closely to a truncated heavy chain consisting of the motor domain and first IQ motif, along with a regulatory light chain. Co-expression experiments demonstrated a strong preference for RLC of the first IQ motif, as it was the only light chain purified alongside the S1 heavy chain, even if co-expressed with multiple light chains. Myosin-7a-S1 had the highest actin activated ATPase activity among our recombinant myosin-7a constructs.

In contrast to the monomeric full-length myosin-7a, the Leucine Zipper motif containing construct formed a major mass peak in mass photometry readings that was consistent with a dimer. Based on the mass photometry histograms, several light chains are binding to the dimerized motor domains. The exact number of light chains cannot be determined due to the resolution limitations of mass photometry.

6.2 Calcium regulation of myosin-7a

Calcium plays a crucial regulatory role within the inner ear. Hair cells must tightly control the levels of calcium as it controls channel adaptation during MET [99, 100]. Calmodulin is a well-known calcium binding protein. As part of the myosin-7a holoenzyme it suggests that the myosin may be influenced by calcium through calmodulin light chains. To investigate the potential effects of calcium, we performed a steady-state ATPase assay

in the presence of calcium, which revealed increased ATPase activity of myosin. However, calcium addition reduced the motor`s actin gliding abilities.

Calmodulin and certain calmodulin-like proteins, such as CLP, exhibit a significant change in electrophoretic mobility in the presence of free calcium [96, 101]. Calcium binding causes a conformational change in human calmodulin, resulting in a shift from an apparent molecular mass of 17 kDa to 14 kDa. In the case of purified CALML4 samples, this mobility shift was not observed. Calmodulin dissociation in calcium conditions may alter the flexibility of the lever arm and thus the mechanical properties of the myosin, allowing for calcium-sensitive regulation. Although the competition or interaction between the two calmodulin proteins are unknown, the presence of a calcium-dependent calmodulin and a calcium-independent calmodulin-like protein suggests a complex regulatory mechanism.

Although the existence of a myosin-7a binding, calcium insensitive calmodulin-like protein initially raised the possibility of myosin-7a being free from calmodulin entirely and unaffected by calcium, our experiments show that myosin-7a requires the presence of multiple light chains, including calmodulin in order to be stable and resistant to proteolysis. Experiments examining the effect of calcium on mechanical activity show that myosin-7a retains calcium sensitivity despite having the calcium insensitive CALML4. CALML4 has therefore not evolved as a replacement for calmodulin in the myosin-7a context and its role is not to remove calcium sensitivity. The apparent cooperativity of binding between CALML4 and calmodulin may suggest that CALML4 has a role in protecting the lever arm during calcium-induced detachment of calmodulin and allowing a rapid rebinding of calmodulin when calcium levels are sufficiently low. Similarly to myosin-1c, myosin-7a might undergo a calcium dependent cycling between a rigid and a flexible lever arm conformation, hence the load bearing capabilities are controlled by changes in calcium concentration (**Figure 50**) [54].

The exact role of calcium in regulating myosin-7a in hair cells is unclear and will require more precise understanding of the calcium concentrations in the regions to which myosin-7a is localized.

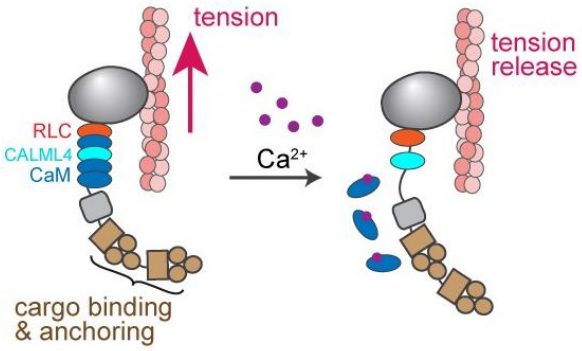

***Figure 50**. Hypothetical model of myosin-7a during mechanoelectrical transduction. The increase in intracellular calcium level initiates light chain dissociation from the heavy chain which results in releasing the tension as the rigidity of the neck region changes.*

6.3 Regulation of the mechano-enzymatic activity by the N-terminal extension

Alternative transcription and translation start sites generate multiple isoforms of myosin-7a in the cochlea. The hair cell types show different expression patterns of the isoforms. In OHCs the expression pattern of the two isoforms is inversely correlated, with the canonical long N-terminal myosin-7a expressed mostly at the apex, while the short N-terminal myosin-7a is expressed at the base of the cochlea. The IHCs are thought to only express the canonical long N-terminal isoform [37]. The two isoforms differ only in their N-terminal domain, with the canonical isoform having an 11-amino acid long extension preceding the motor domain.

In order to study the effect of this N-terminal extension, we have engineered and purified tail-truncated myosin-7a constructs. Through an *in vitro* actin gliding experiment, surface-bound myosin propelled fluorescently labeled actin filaments, revealing a significant difference between the canonical long isoform and the short isoform. The actin filaments moved ~2 times faster on the long N-terminal isoform. It is noteworthy that the GFP-tagged long isoform, where the GFP-tag was attached to the N-terminal of the myosin-7a, showed motile properties similar to the short isoform.

Compared to the full-length myosin-7a, the slower motility rates for the myosin-7a-5IQ fragment are likely due in part to its attachment to the nitrocellulose

surface which may compromise the length of its powerstroke. It has been well known that full-length myosin and longer myosin-2 fragments such as heavy meromyosin (HMM) move actin filaments faster than S1 [102]. The tail-truncated myosin is missing the SAH domain, which acts as an extension of the neck domain. During the gliding assay, some of the lever is bound to the surface, resulting in compromised power stroke sizes which would translate to slower motility rates.

By utilizing a steady-state ATPase assay to assess the activated ATPase activity of the myosin-7a isoform, we have observed that the canonical long isoform exhibits a greater ATPase activity as compared to the short isoform. Similarly to the gliding assay, the GFP-tagged long isoform exhibited a lower ATPase activity, closely matching the activity of the short isoform.

According to structural predictions, the N-terminal extension of myosin-7a is closely situated near the nucleotide binding pocket of the motor domain [38]. Our observations suggest that the extension may play a role in the allosteric regulation of ATP hydrolysis, most likely in ADP or phosphate release.

Fluorescent tags are commonly employed to label proteins. GFP-tags have been used to label myosin for more than two decades [103]. Similar to GFP, mCherry is a fluorescent tag that can be genetically encoded into the recombinant protein. In our assays investigating the effect of the N-terminal extension of myosin-7a, we found that the GFP-tag preceding the extension had a similar diminishing effect as the absence of the extension itself. We have taken this into account and analyzed our data for the potential inhibitory effect of the fluorescent labels on activity

Myosin-7a is believed to directly control the tip link resting tension and thereby regulate the open probability of the MET channel [37]. Intriguingly, recent studies on hair bundle mechanics have revealed a tonotopic variation in the tip-link tension of OHCs, wherein the tension gradually increases towards the base [104]. The short N-terminal isoform, which increases in concentration towards the base, exhibits lower ATPase activity with higher affinity to actin comparing to the long N-terminal isoform. These observations collectively suggest that the two myosin-7a isoforms may have

distinct mechanochemistry that contributes to the tonotopic gradients of the tip link tension.

Similarly, alternative splicing controls the presence or absence of an N-terminal extension for myosin-15, which directs the intracellular localization of the motor protein and maintains stereocilia structure [105, 106]. The N-terminal region of myosin-1 has a critical role in tuning mechanochemistry. Both myosin-1b and -1c have short N-terminal extensions, preceding their motor domain that influence their force-sensitivity. As a result of swapping the N-terminal extension on the two isoforms, the behavior and mechanosensing properties of the isoforms are also exchanged [55].

Based on the unique expression pattern and differing enzymatic activity we propose that the hair cell regulates its mechanosensitivity by adjusting the expression levels of the two myosin-7a isoforms. The significance of this N-terminal extension regarding deafness is still unknown.

6.4 Motile properties of myosin-7a

To study single molecule motile properties of myosin-7a and observe possible processivity, which is required for an efficient transport, we used single molecule motility assay methods *in vitro* and in ARPE19 cell cultures. ARPE19 cells produce filopodia, which are actin-filled plasma-membrane protrusions that can be found also on a variety of epithelial cells [107, 108]. Stereocilia are more complex membrane protrusions filled with parallel actin bundles. The actin core is held together by actin bundling proteins [109, 110]. Even though filopodia and stereocilia differ in their structure and function, the actin bundles inside them not only provide the structural core, but also provide a molecular highway for motors to transport their cargo.

Processivity usually requires a motor protein to dimerize or work in ensemble. However, the short alpha-helical motif is not able to dimerize myosin-7a and functions as a SAH domain and not as coiled-coil. Dimerization of monomeric motor proteins is also possible through the binding of partner proteins. Cell culture experiments demonstrated that human myosin-7a becomes processive with the presence of a

dimerizing binding partner, much like *Drosophila* myosin-7a, which is dimerized by M7BP [30, 45]. Prior studies have documented the activation of myosin-7a through MyRIP in ARPE19 cells.

Since both MyRIP and M7BP have an actin-binding domain that could interfere with the motor activity of myosin [30], we constructed a GFP-tagged myosin-7a Leucine Zipper dimer with a truncated tail to reveal its intrinsic motility in the dimeric state.

In order to study the kinetic details of the dimerized myosin, we performed single molecule *in vitro* motility assays using TIRF microscopy. The forced dimerized motor slowly moved (~ 4.4 nm/s) along single actin filaments, travelling long distance while staying attached for a prolonged time.

Following transient transfection of ARPE19 cells with the dimerized construct, we observed abundant filopodia formation with the GFP-tagged motor moving along the filopodia and accumulating at the tips. Given the high flexibility and mobility of the protrusions, only a small number of motor protein translocation have been observed and measured. However, our measurements (~ 10 nm/s) are in good agreement with previous observations [36]. It is plausible that the forced myosin-7a dimer has a more efficient processivity along actin bundles in the cellular environment rather than on single actin filaments in the *in vitro* assay, similar to myosin-5c [111]. The variation in velocity observed may be also attributed to the potential reduction in efficacy due to the GFP-tag on the recombinant protein and the temperature difference of the different experiments. The cellular observations were done at 37 °C while the *in vitro* assays were performed at 25 °C.

Since the C-terminal FERM domain of myosin-7a folds back to the motor, molecules targeting this area are predicted to be able to alleviate the inhibition. MyRIP, a known binding partner of myosin-7a and Rab27a has been shown to activate the myosin *in vivo* [45]. To study the kinetic details of full-length myosin-7a processivity, we utilized single molecule *in vitro* motility assays and TIRF microscopy. Myosin-7a alone did not exhibit processivity. The autoinhibited motor protein remained strongly attached to actin filaments. However, with the inclusion of MyRIP, myosin-7a began to exhibit processive behavior. The analysis of the motility assay of full-length myosin-7a and MyRIP shows

that the motor and binding partner move together at low speed (~ 7.8 nm/s) for the entire duration of the recorded movement. The kinetic data of the MyRIP-induced myosin-7a dimer are in good agreement with the results obtained with the artificially dimerized myosin-7a, validating the latter method as a useful tool to study dimerizable complexes. However, the effect of the fluorescent tag at the N-terminus should be taken into account, i.e. these values are probably closer to the parameters of the short N-terminal isoforms, than to those of the long isoform.

At higher concentrations, we observed larger fluorescent complexes. These multimers are likely composed of several myosin-7a and MyRIP molecules. Interestingly, the complex became part of other motor-adaptor clusters as it traveled along the actin filaments until it reached the end of the given filament. This observation suggests the potential for oligomerization of myosin-7a, although no additional evidence has been discovered to confirm the formation of large complexes by the myosin. Our findings also indicate that full-length myosin-7a is not processive in the presence of MyBD alone.

Following transient transfection of ARPE19 cells with full-length myosin-7a, we have observed the diffuse localization of the GFP-tagged motor protein. The lack of filopodia formation and no observed motility suggest that the myosin is in the autoinhibited conformation. After transiently transfecting MyRIP, the mCherry-tagged protein localized along the cytoskeleton and we also observed red coloration on small, moving vesicles. Previous studies did not observe this unique localization of MyRIP because the cell line they used expressed endogenous myosin-7a [45]. Through the use of immunoblotting, it has been confirmed that the ARPE19 cell line utilized in our study does not contain any detectable levels of myosin-7a or MyRIP. The observed localization of MyRIP is thought to be caused by its actin-binding domain. The small moving vesicles are believed to be melanosome vesicles, as previous studies have shown that MyRIP is known to associate with these organelles in the RPE [58, 62, 68, 69]. When co-transfecting mCherry MyRIP and GFP-tagged full-length myosin-7a into ARPE19 cells, we observed abundant formation of filopodia and subsequent translocation of the

motor-adaptor complex to the tips of the filopodia. The autoinhibition was alleviated through co-transfecting the binding partner.

Melanosomes play an important protecting role in the retina [112]. The distribution of melanosomes in the RPE changes throughout the light cycle [113, 114], therefore, proper trafficking of melanosomes is necessary for physiological function. The transfer of melanosomes requires a tripartite complex comprising Rab27a and myosin-7a on actin bound by the linker protein MyRIP, which is strikingly similar to the Rab27a-melanophilin-myosin-5 complex required for the interaction of melanosomes with the actin cytoskeleton in melanocytes [62].

In early studies, full-length mouse myosin-7a has been shown to move along actin filaments at a velocity of approximately 160-190 nm/s [33, 34]. However, more recent data from *Drosophila* indicates a significantly lower processivity, about 10-20 times lower [30]. Our experiments also reveal a slow-moving rate, but the processive motion and the long run length on the actin track indicate that the human isoform still may function as an effective transporter. Myosin-7b, the other isoform of the myosin-7 class facilitate the transportation of IMAC components in microvilli. Both myosin-7 isoforms possess two tandem MyTH4-FERM domains, that provide an interaction surface and transport multiple binding partners along the actin bundles. Multiple Usher proteins, including harmonin, cadherin 23, protocadherin 15, CIB2, SANS, clarin-1, whirlin, VLGR1, and usherin, directly interact with myosin-7a [75, 76]. Myosin-7a serves as a transporter, facilitating the trafficking of these Usher proteins and playing an essential role in their correct subcellular localization.

6.5 Myosin-7a is an excellent candidate as tension generating motor

Based on a generally accepted theory, a myosin motor is involved in adjusting tension through the tip-link between two stereocilia. A slow myosin, such as myosin-7a is an excellent candidate as it is able to exert force on the links connecting stereocilia whilst translocating along the actin core and it localizes at the appropriate position to fulfill this

role [52, 57]. Moreover, the tonotopic distribution of the myosin-7a isoforms along the basilar membrane of the cochlear duct helps to maintain the varying tension.

Myosin-1c is another potential candidate for the role of the tension generating motor in stereocilia as it is abundant in stereocilia tips [53], cycles between a rigid and a flexible lever arm conformation in a calcium-dependent manner [54] and it has the properties of a slow transporter while load-sensing [55]. However, based on previous results and our current finding, it raises the possibility of the two motor proteins and their isoforms working together in a tightly regulated manner to generate and adapt the resting tension in hair cells.

7 Conclusion

A motor protein requires a variety of regulatory mechanisms to function effectively. In this work we had set out to investigate certain intra- and inter-molecular regulations that are deployed to tune overall function of human myosin-7a.

In conclusion, we have purified full-length human myosin-7a and investigated its *in vitro* characteristics. Using electron microscopy and mass photometry we were able to observe the individual biomolecules, confirming that myosin-7a is predominantly a monomeric myosin and that it has an autoinhibitory state in physiological conditions. Using steady-state ATPase assay we showed that the autoinhibition of myosin can be alleviated by calcium. However, upon calcium addition, certain light chains dissociate from the myosin which impairs its lever rigidity, resulting in slower actin gliding velocities. The recent discovery of two isoforms in the cochlea differing only in their N-terminus prompted us to investigate how the extension alters the myosins function. We discovered that the canonical (longer) isoform has a higher ATPase activity and actin gliding capability than the short isoform. Also, blocking the N-terminal of the myosin resulted in similar lowered activity. Lastly, we also investigated the forced and cargo-induced dimerization of myosin-7a in single molecule *in vitro* motility assay using TIRF microscopy and live cell imaging in ARPE19 cells. We have found that myosin-7a is a very slow myosin, however, as it travels long distances while staying attached for a prolonged time. We also noted that full-length myosin-7a was able to form large complexes with its cargo and move processively.

The majority of the measurements were performed *in vitro* and, to a lesser extent, on model cells. The kinetics measurements aimed to simulate the processes occurring in the inner ear hair cells, while the processivity studies were primarily intended to model the transportation of retinal melanosomes. Naturally, the investigated systems cannot be equated to the complexity of human cells, where the function of myosin-7a may be affected by other factors beyond the scope of this thesis. We examined the roles of light chains, Ca^{2+}-regulation, isoform-related differences, and MyRIP binding, however

several other proteins in the Usher complex can also associate to and likely regulate myosin-7a.

Our results indicate that there is a complex network of regulatory mechanisms that are working in synchrony to fine-tune the activity, structure, localization, oligomeric state, and function of this unconventional myosin. While we gained some insight into these mechanisms', there is more to uncover. The successful production of intact and functional full-length human myosin-7a enables future studies to understand the molecular details of human vision and hearing loss caused by myosin-7a defects. Our results also contribute to the understanding of retinal cell and inner hair cell function at the molecular level, which may facilitate further cellular or *in vivo* studies.

8 Publications Related to the Dissertation

8.1 Journal article

Holló A, Billington N, Takagi Y, Kengyel A, Sellers JR, Liu R. Molecular regulatory mechanism of human myosin-7a. *J Biol Chem*. 2023 Oct;299(10):105243. doi: 10.1016/j.jbc.2023.105243. Epub 2023 Sep 9.
Impact Factor: 5.4

8.2 Conference abstracts and posters

1. **Holló, A.,** Billington N., Kengyel, A., Sellers, JR, Liu, R. (2021): Molecular Regulatory Mechanisms of Human Myosin-7a. *ASCB Cell Bio Virtual.* Virtual, USA, December 2021, Mol. Biol. Cell 28, page 546 (Abstract #P908)

2. **Holló, A.,** Billington N., Kengyel, A., Sellers, JR, Liu, R. (2022): Molecular Regulatory Mechanisms of Human Myosin-7a. *66th Annual Meeting of the Biophysical Society,* San Francisco, CA, USA, February 2022, 1406-Plat

3. **Holló, A.,** Billington N., Kengyel, A., Sellers, JR, Liu, R. (2022): Molecular Regulatory Mechanisms of Human Myosin-7a. Cytoskeletal Motors Gordon Research Seminar and Conference, Dover, VT, USA, July 2022.

4. **Holló, A.,** Billington N., Kengyel, A., Sellers, JR, Liu, R. (2022): Mechanistic Insight into the Regulation of Human Myosin-7a. ASCB Cell Bio. Washington DC, USA, December 2022, Mol. Biol. Cell 33, page 485 (Abstract #P1801)

5. **Holló, A.,** Billington N., Kengyel, A., Sellers, JR, Liu, R. (2023): Mechanistic Insight into the Regulation of Human Myosin-7a. *67th Annual Meeting of the Biophysical Society,* San Diego, CA, USA, February 2023, 1258-Pos

6. **Holló, A.,** Billington N., Kengyel, A., Sellers, JR, Liu, R. (2023): Human myosin-7a has multiple distinct regulatory mechanisms that makes it an excellent candidate as tension adaptation motor. ASCB Cell Bio. Boston, MA, USA, December 2023, Mol. Biol. Cell 35, page 518 (Abstract # P1833)

9 Other Conference Publications

1. **Holló, A.,** Vékony, Zs., Kengyel, A., Nyitrai, M. (2017): The effect of the myosin 16 ankyrin domain to the actomyosin system. In: XXVI. Congress of the Hungarian Biophysical Society, p83, ISBN: 978-963-12-9447-7.

2. Telek, E., **Holló, A.**, Bécsi, B., Kengyel, A., Erdődi, F., Nyitrai, M. (2018): Binding Properties of the Disordered Myosin 16 Tail Domain. In: Interdisciplinary Doctoral Conference, p100, ISBN: 978-963-429-210-4.

3. Kengyel, A., Telek, E., **Holló, A**., Nyitrai, M. (2018): Autoregulatory Functions of Myosin 16 Domains. Proceedings of the *47th European Muscle Conference*, Budapest, Hungary, August 2018, p96.

4. Kengyel, A., Telek, E., **Holló, A.,** Nyitrai, M. (2018): *Autoregulatory mechanisms during the function of Myosin 16 motorprotein*. Proceedings of the *48th Membrane-transport Conference*, Sümeg, Hungary, May 2018, p24.

5. Telek E., **Holló A.**, Bécsi B., Kengyel A., Erdődi F., Nyitrai, M. (2018): *Interactions of the disordered myosin 16 C-terminal domain*. Proceedings of the *48th Membrane-transport Conference*, Sümeg, Hungary, May 2018, p63.

6. **Holló, A.,** Vékony, Zs., Kengyel, A., Nyitrai, M. (2018): The effect of the myosin 16 ankyrin domain to the actomyosin system. Proceedings of the *48th Membrane-transport Conference*, Sümeg, Hungary, May 2018, p25.

7. Telek, E., **Holló, A**., Bécsi, B., Kengyel, A., Erdődi, F., Nyitrai, M. (2018): Binding properties of the Myosin 16 Tail domain. Proceedings of the *62nd Annual Meeting of the Biophysical Society*, San Francisco, CA, USA, February 2018, L3628-Pos.

8. **Holló, A.,** Vékony, Zs., Kengyel, A., Nyitrai, M. (2019): The effect of the myosin 16 ankyrin domain to the actomyosin system. *Proceedings of the 7th Hungarian Molecular Life Sciences Conference,* Eger, Hungary, March 2019, p209.

10 Scientific Activities

2018 Sümeg 48th Membrane-transport Conference

Poster presentation – A miozin 16 ankyrin domén hatása az aktomiozin rendszerre

2019 Eger 7th Hungarian Molecular Life Sciences Conference

Poster presentation – A miozin 16 ankyrin domén hatása az aktomiozin rendszerre

2021 ASCB Cell Bio Virtual Meeting

Poster presentation – Molecular Regulatory Mechanism of Human Myosin-7a

2022 66th Annual Biophysical Society Meeting

Platform oral presentation, session chair – Molecular Regulatory Mechanism of Human Myosin-7a

2022 Cytoskeletal Motors Gordon Research Seminar and Conference

GRS oral and GRC poster presentation – Mechanistic Insight into The Regulation of Human Myosin-7a

2022 11th Interdisciplinary Doctoral Conference

Oral presentation – Mechanistic Insight into The Regulation of Human Myosin-7a

2022 ASCB Cell Bio Meeting

Poster presentation – Mechanistic Insight into The Regulation of Human Myosin-7a

2023 67th Annual Biophysical Society Meeting

Poster presentation – Mechanistic Insight into The Regulation of Human Myosin-7a

2023 NHLBI Scientific Retreat

Oral presentation – Mechanistic Insight into The Regulation of Human Myosin-7a

2023 7th Chesapeake Bay Area Single Molecule Biology Meeting

Poster presentation – Mechanistic Insight into The Regulation of Human Myosin-7a

2023 ASCB Cell Bio Meeting

Poster presentation – Human myosin-7a has multiple distinct regulatory mechanisms that makes it an excellent candidate as tension adaptation motor

2023 NHLBI Fellow Advisory Committee

Member, FelCom liaison, Head of Visiting Fellow Sub-Committee

2024 Cytoskeletal Motors Gordon Research Seminar and Conference

Elected GRS co-chair

11 Acknowledgements

This dissertation would not have been completed without the support of my advisors and all the lab members who have helped me throughout my PhD journey.

First and foremost, I'd want to convey my heartfelt gratitude to my supervisors, Dr. András Kengyel and Dr. James Sellers, for their exceptional guidance during the entire process of obtaining this degree. András set me on this route, helped me lay the groundwork for a career as a scientist, and Jim, who has continued to support and advise me once I have joined the lab at the NIH. My heartfelt thanks to Dr. Rong Liu for her patience, enthusiasm, and direction, as well as the freedom to explore scientifically and learn to enjoy research.

I would like to thank to Prof. Miklós Nyitrai, Dean of the Medical School, and Dr. András Lukács, Head of the Department of Biophysics for allowing me to start my research in the facility. Furthermore, I would also like to thank my lab colleagues at the Department of Biophysics and at the Sellers Lab for the assistance and friendship.

Last but not least, I would like to thank my family and friends, their love, understanding and support.

12 Bibliography

1. Woehlke, M.S.G., *Molecular motors.* Nature 2003(422): p. 759–765.
2. Uzman, A., *Molecular biology of the cell (4th ed.): Alberts, B., Johnson, A., Lewis, J., Raff, M., Roberts, K., and Walter, P.* Biochemistry and Molecular Biology Education, 2003. **31**(4): p. 212-214.
3. Sebe-Pedros, A., et al., *Evolution and classification of myosins, a paneukaryotic whole-genome approach.* Genome Biol Evol, 2014. **6**(2): p. 290-305.
4. Berg, J.S., B.C. Powell, and R.E. Cheney, *A Millennial Myosin Census.* Molecular Biology of the Cell, 2001. **12**(4): p. 780-794.
5. Peckham, M. and P.J. Knight, *When a predicted coiled coil is really a single α-helix, in myosins and other proteins.* Soft Matter, 2009.
6. Odronitz, F. and M. Kollmar, *Drawing the tree of eukaryotic life based on the analysis of 2,269 manually annotated myosins from 328 species.* Genome Biol, 2007. **8**(9): p. R196.
7. Hartman, M.A. and J.A. Spudich, *The myosin superfamily at a glance.* J Cell Sci, 2012. **125**(Pt 7): p. 1627-32.
8. Wells, A.L., et al., *Myosin VI is an actin-based motor that moves backwards.* Nature, 1999. **401**(6752): p. 505-508.
9. Krendel, M. and M.S. Mooseker, *Myosins: Tails (and Heads) of Functional Diversity.* Physiology, 2005. **20**(4): p. 239-251.
10. Hartman, M.A., et al., *Principles of unconventional myosin function and targeting.* Annu Rev Cell Dev Biol, 2011. **27**: p. 133-55.
11. Heissler, S.M. and J.R. Sellers, *Various Themes of Myosin Regulation.* J Mol Biol, 2016. **428**(9 Pt B): p. 1927-46.
12. Heissler, S.M. and J.R. Sellers, *Myosin light chains: Teaching old dogs new tricks.* Bioarchitecture, 2014. **4**(6): p. 169-88.
13. De La Cruz, E.M. and E.M. Ostap, *Relating biochemistry and function in the myosin superfamily.* Current Opinion in Cell Biology, 2004. **16**(1): p. 61-67.
14. O'Connell, C.B., M.J. Tyska, and M.S. Mooseker, *Myosin at work: motor adaptations for a variety of cellular functions.* Biochim Biophys Acta, 2007. **1773**(5): p. 615-30.
15. Cao, Y., H.D. White, and X.-d. Li, *Drosophila Myosin-XX Functions as an Actin-Binding Protein To Facilitate the Interaction between Zyx102 and Actin.* Biochemistry, 2014. **53**(2): p. 350-360.
16. Heissler, S.M. and J.R. Sellers, *Myosins*, in *Encyclopedia of Cell Biology*, R.A. Bradshaw and P.D. Stahl, Editors. 2016, Academic Press: Waltham. p. 597-607.
17. Uzman, A., *Molecular Cell Biology, Sixth Edition.* Biochemistry and Molecular Biology Education, 2010. **38**(1): p. 60-61.
18. Maffei, M., et al., *Actomyosin interaction at low ATP concentrations.* European Biophysics Journal, 2017. **46**(2): p. 195-202.

19. Stein, L.A., P.B. Chock, and E. Eisenberg, *Rate-limiting step in the actomyosin adenosine triphosphatase cycle.* Biochemistry, 1984. **23**(7): p. 1555-1563.
20. Fili, N. and C.P. Toseland, *Unconventional Myosins: How Regulation Meets Function.* Int J Mol Sci, 2019. **21**(1).
21. Mermall, V., P.L. Post, and M.S. Mooseker, *Unconventional myosins in cell movement, membrane traffic, and signal transduction.* Science, 1998. **279**(5350): p. 527-33.
22. Planelles-Herrero, V.J., et al., *Myosin MyTH4-FERM structures highlight important principles of convergent evolution.* Proc Natl Acad Sci U S A, 2016. **113**(21): p. E2906-15.
23. Petersen, K.J., et al., *MyTH4-FERM myosins have an ancient and conserved role in filopod formation.* Proceedings of the National Academy of Sciences, 2016. **113**(50): p. E8059-E8068.
24. Hasson, T., *Molecular motors: Sensing a function for myosin-VIIa.* Current Biology, 1999. **9**(22): p. R838-R841.
25. Wolfrum, U., et al., *Myosin VIIa as a common component of cilia and microvilli.* Cell Motility, 1998. **40**(3): p. 261-271.
26. Mathur, P. and J. Yang, *Usher syndrome: Hearing loss, retinal degeneration and associated abnormalities.* Biochim Biophys Acta, 2015. **1852**(3): p. 406-20.
27. Chen, Z.-Y., et al., *Myosin-VIIb, a Novel Unconventional Myosin, Is a Constituent of Microvilli in Transporting Epithelia.* Genomics, 2001. **72**(3): p. 285-296.
28. Sahly, I., et al., *Expression of myosin VIIA during mouse embryogenesis.* Anatomy and Embryology, 1997. **196**(2): p. 159-170.
29. Chen, Z.-Y., et al., *Molecular Cloning and Domain Structure of Human Myosin-VIIa, the Gene Product Defective in Usher Syndrome 1B.* 1996. **36**: p. 440-448.
30. Liu, R., et al., *A binding protein regulates myosin-7a dimerization and actin bundle assembly.* Nature Communications, 2021. **12**(1): p. 563.
31. Watanabe, S., R. Ikebe, and M. Ikebe, *Drosophila myosin VIIA is a high duty ratio motor with a unique kinetic mechanism.* J Biol Chem, 2006. **281**(11): p. 7151-60.
32. Heissler, S.M. and D.J. Manstein, *Functional characterization of the human myosin-7a motor domain.* Cell Mol Life Sci, 2012. **69**(2): p. 299-311.
33. Inoue, A. and M. Ikebe, *Characterization of the motor activity of mammalian myosin VIIA.* J Biol Chem, 2003. **278**(7): p. 5478-87.
34. Udovichenko, I.P., D. Gibbs, and D.S. Williams, *Actin-based motor properties of native myosin VIIa.* Journal of Cell Science, 2002. **115**(2): p. 445-450.
35. Yang, Y., et al., *Dimerized Drosophila myosin VIIa: A processive motor.* Proceedings of the National Academy of Sciences, 2006. **103**(15): p. 5746-5751.
36. Sato, O., et al., *Human myosin VIIa is a very slow processive motor protein on various cellular actin structures.* J Biol Chem, 2017. **292**(26): p. 10950-10960.
37. Li, S., et al., *Myosin-VIIa is expressed in multiple isoforms and essential for tensioning the hair cell mechanotransduction complex.* Nat Commun, 2020. **11**(1): p. 2066.

38. Moreland, Z.G. and J.E. Bird, *Myosin motors in sensory hair bundle assembly.* Curr Opin Cell Biol, 2022. **79**: p. 102132.
39. Tobin, M., et al., *Stiffness and tension gradients of the hair cell's tip-link complex in the mammalian cochlea.* eLife, 2019. **8**: p. e43473.
40. Sakai, T., et al., *Structure and Regulation of the Movement of Human Myosin VIIA.* J Biol Chem, 2015. **290**(28): p. 17587-98.
41. Choi, M.S., et al., *The small EF-hand protein CALML4 functions as a critical myosin light chain within the intermicrovillar adhesion complex.* J Biol Chem, 2020. **295**(28): p. 9281-9296.
42. Kapustina, M. and R.E. Cheney, *A new light chain for myosin-7.* J Biol Chem, 2020. **295**(28): p. 9297-9298.
43. Morgan, C.P., et al., *PDZD7-MYO7A complex identified in enriched stereocilia membranes.* Elife, 2016. **5**.
44. Li, J., et al., *Ca(2+)-Induced Rigidity Change of the Myosin VIIa IQ Motif-Single alpha Helix Lever Arm Extension.* Structure, 2017. **25**(4): p. 579-591 e4.
45. Sakai, T., et al., *Cargo binding activates myosin VIIA motor function in cells.* Proc Natl Acad Sci U S A, 2011. **108**(17): p. 7028-33.
46. Yu, I.M., et al., *Myosin 7 and its adaptors link cadherins to actin.* Nat Commun, 2017. **8**: p. 15864.
47. Kuroda, T.S. and M. Fukuda, *Identification and Biochemical Analysis of Slac2-c/MyRIP as a Rab27A-, Myosin Va/VIIa-, and Actin-Binding Protein*, in *Methods in Enzymology*. 2005, Academic Press. p. 431-444.
48. Whatley, M., et al., *Usher Syndrome: Genetics and Molecular Links of Hearing Loss and Directions for Therapy.* Front Genet, 2020. **11**: p. 565216.
49. Krey, J.F. and P.G. Gillespie, *Chapter 53 - Molecular Biology of Hearing and Balance*, in *Basic Neurochemistry (Eighth Edition)*, S.T. Brady, et al., Editors. 2012, Academic Press: New York. p. 916-927.
50. D, O.M. and A.J. Ricci, *A Bundle of Mechanisms: Inner-Ear Hair-Cell Mechanotransduction.* Trends Neurosci, 2019. **42**(3): p. 221-236.
51. Grati, M. and B. Kachar, *Myosin VIIa and sans localization at stereocilia upper tip-link density implicates these Usher syndrome proteins in mechanotransduction.* Proc Natl Acad Sci U S A, 2011. **108**(28): p. 11476-81.
52. Gillespie, P.G., *Myosin-VIIa and transduction channel tension.* Nature Neuroscience, 2002. **5**(1): p. 3-4.
53. Dumont, R.A., et al., *Myosin-I Isozymes in Neonatal Rodent Auditory and Vestibular Epithelia.* Journal of the Association for Research in Otolaryngology, 2002. **3**(4): p. 375-389.
54. Lu, Q., et al., *Structure of myosin-1c tail bound to calmodulin provides insights into calcium-mediated conformational coupling.* Nat Struct Mol Biol, 2015. **22**(1): p. 81-8.
55. Greenberg, M.J., et al., *Mechanochemical tuning of myosin-I by the N-terminal region.* Proceedings of the National Academy of Sciences, 2015. **112**(26): p. E3337-E3344.

56. Gillespie, P.G. and J.L. Cyr, *Myosin-1c, the Hair Cell's Adaptation Motor*. Annual Review of Physiology, 2004. **66**(1): p. 521-545.
57. Kros, C.J., et al., *Reduced climbing and increased slipping adaptation in cochlear hair cells of mice with Myo7a mutations.* Nature Neuroscience, 2002. **5**(1): p. 41-47.
58. Klomp, A.E., et al., *Analysis of the linkage of MYRIP and MYO7A to melanosomes by RAB27A in retinal pigment epithelial cells.* Cell Motil Cytoskeleton, 2007. **64**(6): p. 474-87.
59. Williams, D.S., *Usher syndrome: Animal models, retinal function of Usher proteins, and prospects for gene therapy.* Vision Research, 2008. **48**(3): p. 433-441.
60. Williams, David S. and Vanda S. Lopes, *The many different cellular functions of MYO7A in the retina.* Biochemical Society Transactions, 2011. **39**(5): p. 1207-1210.
61. Liu, X., et al., *Myosin VIIa Participates in Opsin Transport through The Photoreceptor Cilium.* The Journal of Neuroscience, 1999. **19**(15): p. 6267-6274.
62. Lopes, V.S., et al., *The Ternary Rab27a–Myrip–Myosin VIIa Complex Regulates Melanosome Motility in the Retinal Pigment Epithelium.* Traffic (Copenhagen, Denmark), 2007. **8**: p. 486 - 499.
63. Fukuda, M. and T.S. Kuroda, *Slac2-c (Synaptotagmin-like Protein Homologue Lacking C2 Domains-c), a Novel Linker Protein that Interacts with Rab27, Myosin Va/VIIa, and Actin *.* Journal of Biological Chemistry, 2002. **277**(45): p. 43096-43103.
64. Fukuda, M., T.S. Kuroda, and K. Mikoshiba, *Slac2-a/Melanophilin, the Missing Link between Rab27 and Myosin Va: IMPLICATIONS OF A TRIPARTITE PROTEIN COMPLEX FOR MELANOSOME TRANSPORT**. Journal of Biological Chemistry, 2002. **277**(14): p. 12432-12436.
65. El-Amraoui, A., et al., *MyRIP, a novel Rab effector, enables myosin VIIa recruitment to retinal melanosomes.* EMBO reports, 2002. **3**(5): p. 463-470.
66. Waselle, L., et al., *Involvement of the Rab27 Binding Protein Slac2c/MyRIP in Insulin Exocytosis.* Molecular Biology of the Cell, 2003. **14**(10): p. 4103-4113.
67. Kuroda, T.S. and M. Fukuda, *Functional Analysis of Slac2-c/MyRIP as a Linker Protein between Melanosomes and Myosin VIIa *.* Journal of Biological Chemistry, 2005. **280**(30): p. 28015-28022.
68. Kuroda, T.S. and M. Fukuda, *Functional analysis of Slac2-c/MyRIP as a linker protein between melanosomes and myosin VIIa.* J Biol Chem, 2005. **280**(30): p. 28015-22.
69. Ramalho, J.S., et al., *Myrip uses distinct domains in the cellular activation of myosin VA and myosin VIIA in melanosome transport.* Pigment Cell & Melanoma Research, 2009. **22**(4): p. 461-473.
70. Lewis, M.A., et al., *An ENU-induced mutation of miR-96 associated with progressive hearing loss in mice.* Nature Genetics, 2009. **41**(5): p. 614-618.
71. Weston, M.D. and G.A. Soukup, *MicroRNAs sound off.* Genome Medicine, 2009. **1**(6): p. 59.

72. Friedman, T.B., J.R. Sellers, and K.B. Avraham, *Unconventional myosins and the genetics of hearing loss.* American Journal of Medical Genetics, 1999. **89**(3): p. 147-157.
73. Well, D., et al., *Defective myosin VIIA gene responsible for Usher syndrome type IB.* Nature, 1995. **374**(6517): p. 60-61.
74. Stauffer, E.A., A. Lelli, and J.R. Holt, *Hair Cell Transduction and Adaptation: Physiology and Molecular Mechanisms*, in *The Senses: A Comprehensive Reference*, R.H. Masland, et al., Editors. 2008, Academic Press: New York. p. 263-292.
75. Ahmed, Z.M., G.I. Frolenkov, and S. Riazuddin, *Usher proteins in inner ear structure and function.* Physiological Genomics, 2013. **45**(21): p. 987-989.
76. Cosgrove, D. and M. Zallocchi, *Usher protein functions in hair cells and photoreceptors.* The International Journal of Biochemistry & Cell Biology, 2014. **46**: p. 80-89.
77. Sahly, I., et al., *Localization of Usher 1 proteins to the photoreceptor calyceal processes, which are absent from mice.* Journal of Cell Biology, 2012. **199**(2): p. 381-399.
78. Kiehart, D.P., et al., *Drosophila crinkled, Mutations of Which Disrupt Morphogenesis and Cause Lethality, Encodes Fly Myosin VIIA.* Genetics, 2004. **168**(3): p. 1337-1352.
79. Sallee, J.L., et al., *Mutations in Drosophila crinkled/Myosin VIIA disrupt denticle morphogenesis.* Developmental Biology, 2021. **470**: p. 121-135.
80. Caldwell, J.C. and D.F. Eberl, *Towards a molecular understanding of drosophila hearing.* Journal of Neurobiology, 2002. **53**(2): p. 172-189.
81. Ernest, S., et al., *Mariner is defective in myosin VIIA: a zebrafish model for human hereditary deafness.* Human Molecular Genetics, 2000. **9**(14): p. 2189-2196.
82. Self, T., et al., *Shaker-1 mutations reveal roles for myosin VIIA in both development and function of cochlear hair cells.* Development, 1998. **125**(4): p. 557-566.
83. Saw, J.D., K.P. Steel, and S.D.M. Brown, *Shaker Mice and a Peek into the House of Usher.* Experimental Animals, 1997. **46**(1): p. 1-9.
84. Jarvis, D.L., *Baculovirus–Insect Cell Expression Systems*, in *Methods in Enzymology*, R.R. Burgess and M.P. Deutscher, Editors. 2009, Academic Press. p. 191-222.
85. Sari, D., et al., *The MultiBac Baculovirus/Insect Cell Expression Vector System for Producing Complex Protein Biologics.* Adv Exp Med Biol, 2016. **896**: p. 199-215.
86. Pardee, J.D. and J.A. Spudich, *Purification of Muscle Actin*, in *Methods in Cell Biology*, L. Wilson, Editor. 1982, Academic Press. p. 271-289.
87. Guzik-Lendrum, S., et al., *Mammalian Myosin-18A, a Highly Divergent Myosin.* Journal of Biological Chemistry, 2013. **288**(13): p. 9532-9548.
88. Burgess, W.H., D.K. Jemiolo, and R.H. Kretsinger, *Interaction of calcium and calmodulin in the presence of sodium dodecyl sulfate.* Biochimica et Biophysica Acta (BBA) - Protein Structure, 1980. **623**(2): p. 257-270.

89. Young, G., et al., *Quantitative mass imaging of single biological macromolecules.* Science, 2018. **360**(6387): p. 423-427.
90. Wu, D. and G. Piszczek, *Standard protocol for mass photometry experiments.* European Biophysics Journal, 2021. **50**(3): p. 403-409.
91. Alexander, C.G., et al., *Novel microscale approaches for easy, rapid determination of protein stability in academic and commercial settings.* Biochimica et Biophysica Acta (BBA) - Proteins and Proteomics, 2014. **1844**(12): p. 2241-2250.
92. Jerabek-Willemsen, M., et al., *MicroScale Thermophoresis: Interaction analysis and beyond.* Journal of Molecular Structure, 2014. **1077**: p. 101-113.
93. Bird, J.E., et al., *Chaperone-enhanced purification of unconventional myosin 15, a molecular motor specialized for stereocilia protein trafficking.* Proc Natl Acad Sci U S A, 2014. **111**(34): p. 12390-5.
94. Jiang, F., et al., *The ATPase mechanism of myosin 15, the molecular motor mutated in DFNB3 human deafness.* J Biol Chem, 2021. **296**: p. 100243.
95. Yang, Y., et al., *A FERM domain autoregulates Drosophila myosin 7a activity.* Proceedings of the National Academy of Sciences, 2009. **106**(11): p. 4189-4194.
96. Rhyner, J.A., et al., *Characterization of the human calmodulin-like protein expressed in Escherichia coli.* Biochemistry, 1992. **31 51**: p. 12826-32.
97. Umeki, N., et al., *The tail binds to the head–neck domain, inhibiting ATPase activity of myosin VIIA.* Proceedings of the National Academy of Sciences, 2009. **106**(21): p. 8483-8488.
98. Senften, M., et al., *Physical and functional interaction between protocadherin 15 and myosin VIIa in mechanosensory hair cells.* J Neurosci, 2006. **26**(7): p. 2060-71.
99. Lumpkin, E.A. and A.J. Hudspeth, *Regulation of Free Ca2+ Concentration in Hair-Cell Stereocilia.* The Journal of Neuroscience, 1998. **18**(16): p. 6300-6318.
100. Beurg, M., et al., *Calcium Balance and Mechanotransduction in Rat Cochlear Hair Cells.* Journal of Neurophysiology, 2010. **104**(1): p. 18-34.
101. Rogers, M.S. and E.E. Strehler, *The Tumor-sensitive Calmodulin-like Protein Is a Specific Light Chain of Human Unconventional Myosin X*.* Journal of Biological Chemistry, 2001. **276**(15): p. 12182-12189.
102. Toyoshima, Y.Y., et al., *Myosin subfragment-1 is sufficient to move actin filaments in vitro.* Nature, 1987. **328**(6130): p. 536-539.
103. Sabry, J., et al., *Studies on the Dynamic Localization of GFP-Myosin During Cytokinesis in Live Cells.* Microscopy and Microanalysis, 1997. **3**(S2): p. 129-130.
104. Tobin, M., et al., *Stiffness and tension gradients of the hair cell's tip-link complex in the mammalian cochlea.* Elife, 2019. **8**.
105. Nal, N., et al., *Mutational spectrum of MYO15A: the large N-terminal extension of myosin XVA is required for hearing.* Human Mutation, 2007. **28**(10): p. 1014-1019.
106. Fang, Q., et al., *The 133-kDa N-terminal domain enables myosin 15 to maintain mechanotransducing stereocilia and is essential for hearing.* eLife, 2015. **4**.

107. Mattila, P.K. and P. Lappalainen, *Filopodia: molecular architecture and cellular functions.* Nature Reviews Molecular Cell Biology, 2008. **9**(6): p. 446-454.
108. Khurana, S. and S.P. George, *The role of actin bundling proteins in the assembly of filopodia in epithelial cells.* Cell Adhesion & Migration, 2011. **5**(5): p. 409-420.
109. Houdusse, A. and M.A. Titus, *The many roles of myosins in filopodia, microvilli and stereocilia.* Current Biology, 2021. **31**(10): p. R586-R602.
110. Bartles, J.R., *Parallel actin bundles and their multiple actin-bundling proteins.* Current Opinion in Cell Biology, 2000. **12**(1): p. 72-78.
111. Krementsova, E.B., et al., *Small teams of myosin Vc motors coordinate their stepping for efficient cargo transport on actin bundles.* Journal of Biological Chemistry, 2017. **292**(26): p. 10998-11008.
112. Jiang, M., et al., *Microtubule motor transport in the delivery of melanosomes to the actin-rich apical domain of the retinal pigment epithelium.* Journal of Cell Science, 2020. **133**(15): p. jcs242214.
113. Futter, C.E., et al., *The Role of Rab27a in the Regulation of Melanosome Distribution within Retinal Pigment Epithelial Cells.* Molecular Biology of the Cell, 2004. **15**(5): p. 2264-2275.
114. Meleppat, R.K., et al., *In vivo multimodal retinal imaging of disease-related pigmentary changes in retinal pigment epithelium.* Scientific Reports, 2021. **11**(1): p. 16252.

JBC RESEARCH ARTICLE

Molecular regulatory mechanism of human myosin-7a

Received for publication, June 23, 2023, and in revised form, September 1, 2023 Published, Papers in Press, September 9, 2023,
https://doi.org/10.1016/j.jbc.2023.105243

Alexandra Holló[1,2], Neil Billington[1,3,4], Yasuharu Takagi[1], András Kengyel[2,5], James R. Sellers[1,*], and Rong Liu[1,3,*]

From the [1]Laboratory of Molecular Physiology, National Heart, Lung, and Blood Institute, National Institutes of Health, Bethesda, Maryland, USA; [2]Department of Biophysics, University of Pécs Medical School, Pécs, Hungary; [3]Department of Biochemistry & Molecular Medicine, School of Medicine, and [4]Microscope Imaging Facility, West Virginia University, Morgantown, West Virginia, USA; [5]Institute for Biophysical Chemistry, Hannover Medical School, Hannover, Germany

Reviewed by members of the JBC Editorial Board. Edited by Enrique De La Cruz

Myosin-7a is an actin-based motor protein essential for vision and hearing. Mutations of myosin-7a cause type 1 Usher syndrome, the most common and severe form of deafblindness in humans. The molecular mechanisms that govern its mechanochemistry remain poorly understood, primarily because of the difficulty of purifying stable intact protein. Here, we recombinantly produce the complete human myosin-7a holoenzyme in insect cells and characterize its biochemical and motile properties. Unlike the *Drosophila* ortholog that primarily associates with calmodulin (CaM), we found that human myosin-7a utilizes a unique combination of light chains including regulatory light chain, CaM, and CaM-like protein 4. Our results further reveal that CaM-like protein 4 does not function as a Ca^{2+} sensor but plays a crucial role in maintaining the lever arm's structural–functional integrity. Using our recombinant protein system, we purified two myosin-7a splicing isoforms that have been shown to be differentially expressed along the cochlear tonotopic axis. We show that they possess distinct mechanoenzymatic properties despite differing by only 11 amino acids at their N termini. Using single-molecule *in vitro* motility assays, we demonstrate that human myosin-7a exists as an autoinhibited monomer and can move processively along actin when artificially dimerized or bound to cargo adaptor proteins. These results suggest that myosin-7a can serve multiple roles in sensory systems such as acting as a transporter or an anchor/force sensor. Furthermore, our research highlights that human myosin-7a has evolved unique regulatory elements that enable precise tuning of its mechanical properties suitable for mammalian auditory functions.

The myosin superfamily plays a fundamental role in many forms of cellular motility and cytoskeletal organization (1). Myosin-7a is expressed in actin-rich membrane protrusions of the inner ear and retina. More specifically, it is found in the hair bundles and synapses of the inner ear hair cells, in photoreceptors, and in the retinal pigment epithelium. In mammals, defects in myosin-7a lead to deafness and retinal degeneration known as the type 1B Usher syndrome (2–4).

The full-length myosin-7a consists of a motor domain, followed by a neck region containing 5 IQ motifs, which serves as binding sites for calmodulin (CaM) family member light chains. Its tail contains two MyTH4-FERM (myosin tail homology; band 4.1/ezrin/radexin/moesin homology) domains separated by an SH3 domain (5).

Unconventional myosins are known to bind CaM, CaM-like proteins, regulatory light chains (RLCs), or essential light chains (ELCs) (6). To date, myosin-7a has been coexpressed with CaM only (7). Previous research has demonstrated the potential of the human myosin-7a IQ motifs to bind RLC and ELC, but no in-depth analysis has been carried out to describe the precise light chain composition (8). The possibility of myosin-7a binding to other light chains was raised by the recent identification of CaM-like protein 4 (CALML4) as the endogenous light chain for myosin-7b (9, 10).

Recent studies reveal that the cochlea expresses two myosin-7a isoforms, differing by a short N-terminal extension (11). The canonical long isoform, with an 11 amino acid extension, is predominantly expressed in the inner hair cells, whereas in outer hair cells (OHCs), its expression varies in a tonotopic manner. Its level increases from the base to the apex of the cochlea. The expression pattern of the short isoform, which lacks the 11 amino acid N-terminal extension, is expected to inversely correlate to the canonical myosin-7a (3, 11).

Several studies have demonstrated that the short putative coiled-coil sequence found in the tail of myosin-7a is insufficient to form a dimer. Instead, it is predicted to form a stable single alpha-helix known as the SAH domain (8, 12). Dimerization can potentially be mediated by binding partners. One such binding partner, MyRIP (myosin and Rab interacting protein, also known as exophilin-8/Slac-2c), has been shown to promote movement of myosin-7a in the cellular environment. MyRIP functions as a linker between Rab27a and myosin-7a, and the resulting tripartite complex is hypothesized to be involved in melanosome transport in the retinal pigment epithelium (13, 14).

In this study, we show that a combination of intramolecular and intermolecular regulatory mechanisms are employed to tune the conformation, activity, and oligomeric state of human

* For correspondence: James R. Sellers, sellersj@nhlbi.nih.gov; Rong Liu, rong.liu@hsc.wvu.edu.

myosin-7a. Alternative splicing in the motor domain creates variants with distinct kinetic properties, allowing the mechanical output to be controlled by varying the proportion of fast and slow isoforms. Myosin-7a remains monomeric and therefore unprocessive in isolation. In contrast, it makes long duration processive runs on actin in the presence of binding partners such as MyRIP.

Results

Production of full-length human myosin-7a holoenzyme

In our efforts to recombinantly produce a human myosin-7a from baculovirus-infected *Sf*9 cells, we first attempted to coexpress the full-length myosin-7a (isoform 1, NM_000260.4) with CaM. This approach did not produce soluble intact protein, and instead, we observed the presence of many proteolytic fragments following chromatography over a FLAG-affinity column. Previous studies showed that truncated myosin-7a IQ motifs can bind to RLC and ELC (8). In addition, a small EF-hand protein CALML4 has recently been discovered as a critical light chain for myosin-7b in mammalian gut brush border, and it can interact with myosin-7a in pull-down assays (9, 15). Intriguingly, CALML4 is also identified as a candidate gene for Usher syndrome (USH1H) (16). In view of these observations, we hypothesized that multiple light chain components may be required for producing intact human myosin-7a protein.

To determine the exact light chain composition of the holoenzyme, we coexpressed full-length myosin-7a heavy chain with baculoviruses encoding RLC, ELC, CaM, and CALML4. We selected the short isoform of CALML4 for our studies as it was shown to be the dominant variant in the tissues (gut epithelium) analyzed to date (9). Furthermore, we included a baculovirus expressing both human UNC45B and human HSP90AA1 (Fig. S1*A*), as previous studies have shown that these chaperones can facilitate the folding of myosin-15, a close family member of myosin-7a found in hair cell stereocilia (17, 18). Using these methods, we were able to observe protein bands consistent with the size of full-length myosin-7a in elution fractions from anti-FLAG resin. Mass spectrometric analyses identified that RLC, CaM, and CALML4 were co-purified with myosin-7a but not ELC.

To further optimize the production, we adopted the MultiBac system (19) to coexpress myosin-7a heavy chain, RLC, CaM, and CALML4 *via* a single baculovirus backbone along with the chaperone-containing baculovirus. This approach ultimately resulted in high-yield and purified myosin-7a holoenzyme, with the heavy chain and three types of light chains clearly visible on the gel (Fig. 1, *A* and *B*). CaM and CALML4 have very similar molecular weights but were resolved on 16% SDS gels. The presence of CALML4 was further confirmed by immunoblotting (Fig. S1*B*).

Coexpression of myosin-7a subfragment-1 (M7a-S1) containing only the motor domain and the first IQ motif with multiple light chain candidates revealed that only RLC co-purified with the heavy chain. This observation suggests that the first IQ motif preferentially binds to RLC (Fig. 1*B*).

Human myosin-7a is monomeric and adopts an evolutionarily conserved autoinhibitory conformation

To gain insight into the biophysical properties of human myosin-7a, we first utilized mass photometry to determine its oligomeric states. Mass photometry analysis of M7a-S1 showed a single peak at the mass of 103 kDa, consistent with the molecular weight of one M7a-S1 (∼89 kDa) plus one light chain (RLC, ∼20 kDa) (Fig. 1*C*). The mass photometry profile of full-length myosin-7a resulted in a major mass peak at 325 kDa, which matches the molecular weight of one full-length myosin-7a heavy chain (∼255 kDa) plus four light chains (RLC: ∼20 kDa; CaM and CALML4: ∼17 kDa). It should be noted, however, that the mass photometry is unlikely to resolve multiple populations differing by the mass of one or two light chains. Hence, in scenarios where the myosin contains a mixture of light chain occupancies (*e.g.*, four and five light chains), we are not able to resolve the exact proportion of each. Nevertheless, the peak of the distribution corresponds best to a lever with four light chains bound. The total mass also indicates that the full-length myosin is a monomer. The smaller peaks observed in the ∼50 to 150 kDa range were attributed to proteolytic fragments, which were also detected in SDS gels (Fig. 1*B*). No distinct peak was observed at a position that would correspond to dimer (or other multimers) (Fig. 1*D*).

Using negative-stain electron microscopy, we observed a bent conformation of human myosin-7a at low ionic strength, in which the tail region folds back to contact the motor domain (Fig. 1*E*). The size of the particles was consistent with a monomeric myosin as predicted by the mass photometry. The contour from the probable motor domain-lever junction to the bend point measures 20.7 ± 1.9 nm. This is consistent with the expected length of the lever with 5IQ motifs (∼19 nm) (20). Since the SAH domain is expected to add an additional ∼9 nm to the lever arm, we conclude that the SAH domain does not contribute to the length of the structure leading up to the bend but rather forms part of the return leg, along with the rest of the tail domain motifs. The results from mass photometry suggest weak occupancy at one of the IQ domains (Fig. 1*D*). One possibility is that lack of the light chain at the fifth IQ can contribute to the bending of the tail (Fig. S2). Indeed, it is known that the fifth IQ-SAH region can undergo changes in CaM binding depending on Ca^{2+} concentration (20). However, previous studies have relied on only partial lever fragments in which the context of other light chains is lost. Higher resolution structures of the intact molecule would be needed to further determine this.

The autoinhibition of *Drosophila* myosin-7a was shown to be regulated *via* electrostatic interactions facilitated by charged amino acids within the second FERM domain (21). Increased salt concentration also led to an open conformation of human myosin-7a, suggesting an evolutionarily conserved autoinhibitory mechanism (Fig. 1*F*). The interaction of the tail with the motor domain results in suppression of the enzymatic function. Actin-activated steady-state activity was measured by a NADH-coupled assay. The maximum extrapolated ATPase rate (v_{max}) of the full-length protein was 0.2 ± 0.11 s^{-1} with an

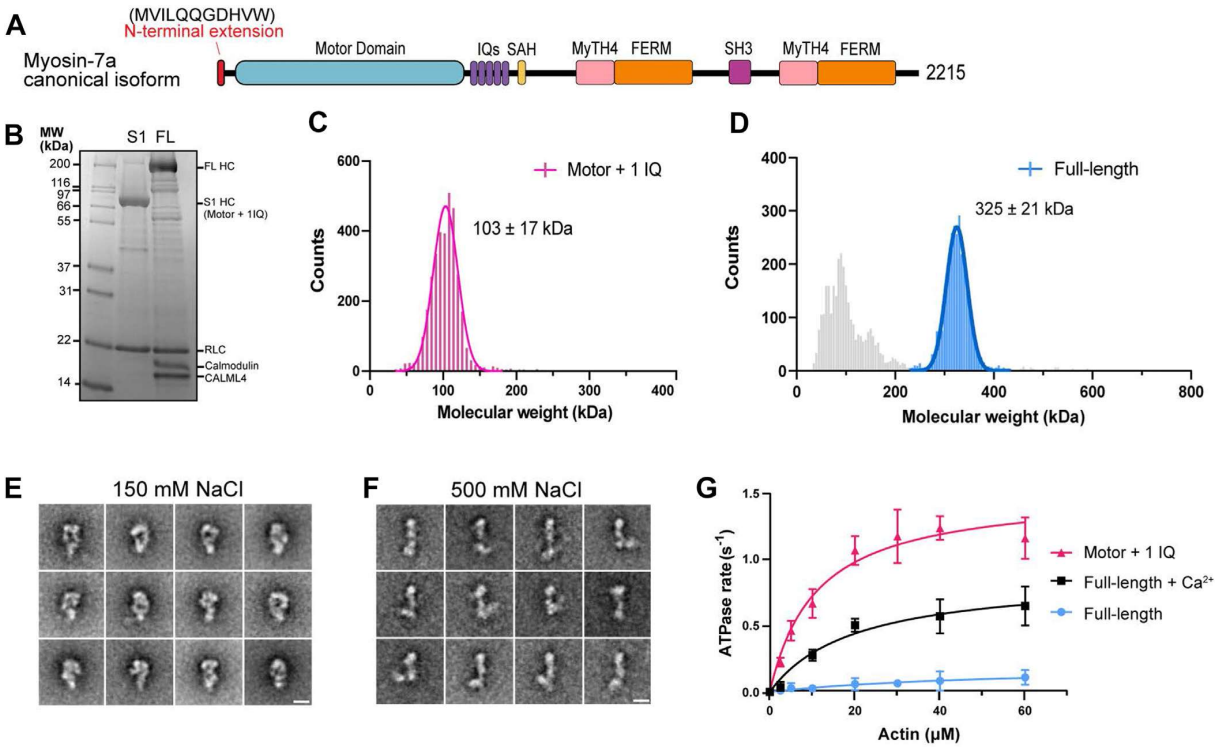

Figure 1. Purified full-length human myosin-7a requires multiple light chains and adopts the autoinhibited conformation at physiological conditions. *A*, domain organizations of human myosin-7a. (Schematics are in scale with the length of their primary sequences). *B*, SDS-PAGE analysis of purified human myosin-7a proteins. Lane 1: molecular mass marker (Mark12; Invitrogen); lane 2, FLAG-affinity purified myosin-7a-S1 consisting of an 86 kDa heavy chain and 20 kDa RLC light chain; lane 3, FLAG-affinity purified myosin-7a-FL consisting of a 255 kDa heavy chain, 20 kDa RLC, and 17 kDa calmodulin and CALML4 light chains. *C* and *D*, single-molecule mass photometry assays. Histograms of the molecular weights of individual particles with a bin width of 5 kDa for the particular protein (*C*: myosin-7a motor + 1IQ, *D*: myosin-7a-FL). *Lines* are the Gaussian fit to the data yielding the molecular weight of the samples. *E* and *F*, class averages from negative-stain electron microscopy images of myosin-7a in (*E*) in 150 mM salt buffer and (*F*) in 500 mM salt buffer in the presence of ATP. Myosin-7a in low salt conditions exhibits a compact autoinhibited conformation, whereas in high salt conditions, the myosin exhibits a more extended conformation. Scale bars represent 10 nm. *G*, actin activated ATPase activity of subfragment 1 (*pink triangle*) (v_{max} = 1.5 ± 0.1 s^{-1}, K_{ATPase} = 11 ± 2.6 μM) and full-length myosin-7a in the absence (*blue circle*) (v_{max} = 0.2 ± 0.11 s^{-1}, K_{ATPase} = 54 ± 4.5 μM) and in the presence of calcium (*black square*) (v_{max} = 0.98 ± 0.27 s^{-1}, K_{ATPase} = 27 ± 7 μM). Values are mean ± SD from four independent experiments. CALML4, calmodulin-like protein 4; RLC, regulatory light chain.

apparent actin affinity (K_{ATPase}) of 54 ± 4.5 μM. In contrast, S1 that lacks the tail domain exhibited a ∼7.5-fold higher maximum ATPase rate at 1.5 ± 0.1 s^{-1} and ∼5-fold higher actin affinity at 11 ± 2.6 μM (Fig. 1*G*). The autoinhibition can be alleviated by calcium ions, and following the addition of calcium, the maximum extrapolated ATPase rate of myosin-7a-FL increased to 0.98 ± 0.27 s^{-1} (Fig. 1*G*, Table 1).

CALML4 and CaM display distinct Ca^{2+}-regulation properties

Calcium influences many CaM-like and other EF-hand containing proteins *via* their calcium-binding sites (22). CaM and CALML4 are 44% identical, allowing their sequences to be aligned and any putative calcium-binding sites examined. When the amino acid sequence of CALML4 is compared with that of CaM, it is evident that the crucial amino acids required for Ca^{2+} chelation are absent in each of the EF-hands of CALML4 (Fig. 2*A*). The presence of some conserved amino acids in the fourth EF-hand suggests it might retain the ability to bind calcium. We therefore performed an electrophoretic mobility shift assay using purified CaM and CALML4 to assess CALML4's calcium-binding capability. CaM exhibited altered electrophoretic mobility upon incubation with Ca^{2+} because of calcium-dependent conformational changes that are known to be detectable in SDS-PAGE as increased mobility (23). In contrast, under the same conditions, the mobility of the CALML4 samples remained unchanged following addition of calcium (Fig. 2*B*). Consistently, microscale thermophoresis (MST) studies show that while CaM binds to Ca^{2+} in the tested concentration range, CALML4 does not bind with calcium under the same conditions (Fig. 2*C*) (Fig. S3). These findings collectively suggest that CALML4 is an EF-hand protein that has lost the ability to bind to Ca^{2+}.

Table 1
Steady-state ATPase activity of myosin-7a constructs

Parameter	FL	FL (+Ca^{2+})	S1
v_{max}	0.2 ± 0.11 s^{-1}	0.98 ± 0.27 s^{-1}	1.5 ± 0.1 s^{-1}
K_{ATPase}	54 ± 4.5 μM	27 ± 7 μM	11 ± 2.6 μM

Abbreviation: FL, full length.

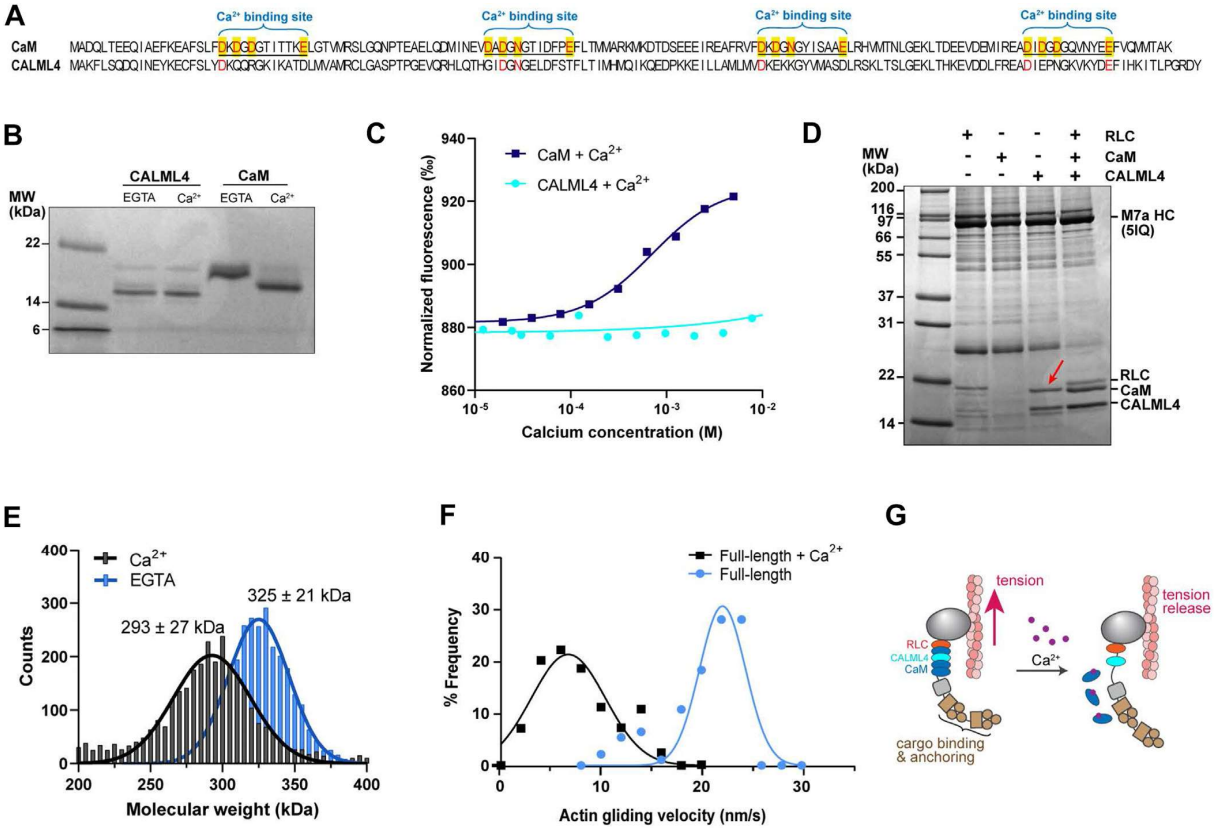

Figure 2. The molecular details of light chain binding to myosin-7a reveal a Ca^{2+}-dependent regulatory mechanism *A*, amino acid comparison of human calmodulin and CALML4. Amino acids critical for calcium binding are highlighted. *B*, electrophoretic mobility shift assay of purified human calmodulin and CALML4. Samples were incubated in the presence of $CaCl_2$ or EGTA and then run on 16% Tris–glycine gel. *C*, normalized fluorescence plotted against calcium concentration of CALML4 (*light blue*, *circles*) and calmodulin (*dark blue*, *squares*). *D*, SDS-PAGE analysis of purified myosin-7a 5IQ S1 constructs coexpressed with indicated light chains. *Red arrow*: endogenous *Sf*9 calmodulin. *E*, interferometric single-molecule mass photometry assay demonstrating the effect of calcium on full-length myosin-7a proteins. The samples were incubated in the presence of $CaCl_2$ (*black*) or EGTA (*blue*). Histograms show the molecular weights of individual particles with a bin width of 5 kDa. *Lines* are the Gaussian fit to the data yielding the molecular weight of the samples. *F*, *in vitro* motility actin gliding assay of full-length long N-terminal myosin-7a in the presence (*black square*) (v = 6.7 ± 3.7 nm/s) and the absence (*blue circle*) (v = 22.1 ± 2.3 nm/s) of calcium. *G*, graphical representation of myosin-7a during mechanoelectrical transduction. The increase in intracellular calcium level initiates light chain dissociation from the heavy chain, which results in releasing the tension as the rigidity of the neck region changes. CALML4, calmodulin-like protein 4.

Interestingly, despite its inability to respond to Ca^{2+} signals, CALML4 appears to be crucial for maintaining the structural–functional integrity of human myosin-7a. In our initial purification attempts, we found that the yield and integrity of full-length myosin-7a was significantly improved when coexpressed with CALML4. Furthermore, we discovered that CaM copurified with our 5IQ S1 constructs only when CALML4 was present, implying that CALML4 may stabilize the interaction of the light chain–binding region with CaM (Fig. 2*D*). This hypothesis is supported by the recruitment of endogenous *Sf*9 CaM by CALML4 as detected on SDS-PAGE after purification when no CaM was coexpressed (Fig. 2*D*, *arrow*).

Light chain binding of myosin-7a is calcium dependent

Using mass photometry, we were also able to visualize effects of calcium on the subunit composition of the purified holoenzyme. In EGTA conditions, the full-length myosin-7a construct exhibited a major mass of 325 ± 21 kDa, corresponding to one heavy chain and four light chains (Fig. 1*D*). Upon the addition of calcium, we observed a shift toward a smaller mass peak at 293 ± 25 kDa, which corresponds to one heavy chain plus an extra 38 kDa. Given that RLC and CALML4 are inert to calcium, we attribute this 38 kDa mass to the combined presence of one RLC and one CALM4 (Fig. 2*E*). The mass photometer does not detect proteins less than 25 kDa, and thus, any dissociated free light chains in this experiment are not detected.

We carried out *in vitro* actin gliding assays to examine the impact of this calcium-induced light chain detachment on the myosin's mechanical activity. The full-length myosin-7a is in an "open" conformation when attached to the surface as the autoinhibition is disrupted, hence it is able to glide actin. Surface-bound myosin moved the fluorescently labeled actin at 22.1 ± 2.3 nm/s. However, in the presence of calcium, the gliding velocity decreased to 6.7 ± 3.7 nm/s (Fig. 2*F*),

suggesting that the myosin's motility is compromised as a result of CaM dissociation from the holoenzyme even though free CaM was present in the assay.

The short N-terminal extension of myosin-7a influences the motor activity

Two isoforms of myosin-7a, termed long and short, are expressed in mammalian cochlea. They are generated *via* alternative splicing with varying translation start sites and only differ by 11 amino acids at the N terminus preceding the motor domain (Fig. 3*A*). Myosin-7a is believed to directly control the tip link resting tension and thereby regulate the open probability of the mechanoelectrical channel (11). Intriguingly, recent studies on hair bundle mechanics have revealed a tonotopic variation in the tip-link tension of OHCs, wherein the tension gradually increases toward the base (24) (Fig. 3*A*). These observations collectively suggest that the two myosin-7a isoforms may have distinct mechanochemistry that contributes to the tonotopic gradients of the tip link tension.

To explore this hypothesis further, we purified the two isoforms and examined the role of the N-terminal extension in the function of myosin-7a. In addition, the common use of an N-terminal GFP tag on myosin-7a (8, 25–27) raises questions about its potential impact on the regulation by the N-terminal extension. We therefore also engineered a long N-terminal construct that includes a GFP moiety before the N terminus (Fig. 3*A*). In addition to the full-length proteins, we engineered constructs containing the motor domain and the 5IQ motifs (M7a-5IQ S1) but no tail to avoid the complication of tail-dependent autoinhibition (Fig. 3*A*).

Steady-state ATPase assays reveal that the long N-terminal 5IQ S1 isoform has a maximal actin-activated ATPase activity of approximately 0.83 ± 0.14 s^{-1}, which is comparable to the activity of the mammalian myosin-7a motor, as measured both in our studies (Fig. 1*G*, Table 2) and in previous work conducted by other groups (7, 28). In contrast, we observed a significant reduction in ATPase activity (~0.1 s^{-1}) in the absence of the N-terminal extension (0.13 ± 0.06 s^{-1}) (Fig. 3*B*, Table 2). *In vitro* actin gliding assays show that the long N-terminal isoform moves actin filaments at a speed of approximately 22 and 5 nm/s for the full-length and 5IQ S1 constructs, respectively (Figs. 2*E* and 3*C*). We reason that the faster actin movement produced by the full-length molecule is in part because of the presence of the SAH domain, which results in a longer lever arm, and therefore longer step-size, compared with the 5IQ S1 constructs (20). The slower motility rates for the 5IQ S1 fragment likely are due in part to its attachment to the nitrocellulose surface, which may compromise the length of its power stroke. It has been well known that full-length myosin and longer myosin-2 fragments such as HMM move actin filaments faster than S1 (29). For the 5IQ S1 fragment, the lack of SAH domain added to the fact that some of the lever is bound to the surface, resulting in compromised motility rates. The short N-terminal isoform exhibited slower gliding speed (~3 nm/s) (Fig. 3*C*).

Interestingly, the GFP-tagged long 5IQ S1 isoform also had a significant reduction in ATPase activity (0.1 ± 0.07 s^{-1}) (Table 2) and exhibited gliding speed (~3 nm/s) similar to the short 5IQ S1 isoform. The N-terminal GFP fusion of the full-length myosin-7a caused a similar reduction in gliding speed compared with that of the untagged version (Fig. 3*C*).

Human myosin-7a moves processively along actin upon dimerization

Drosophila myosin-7a has been shown to dimerize in a cargo-dependent manner and move processively along actin filaments (30). To investigate whether this mechanism is conserved in the human homolog, we engineered a construct to induce artificial dimerization by adding a leucine zipper motif to the myosin-7a-5IQ + SAH sequence (Fig. 4*A*). This construct also contains an N-terminal GFP tag for single-molecule imaging. A major mass species of approximately 406 kDa was detected by mass photometry, matching the sum of two heavy chains (141 kDa each) plus six to eight light

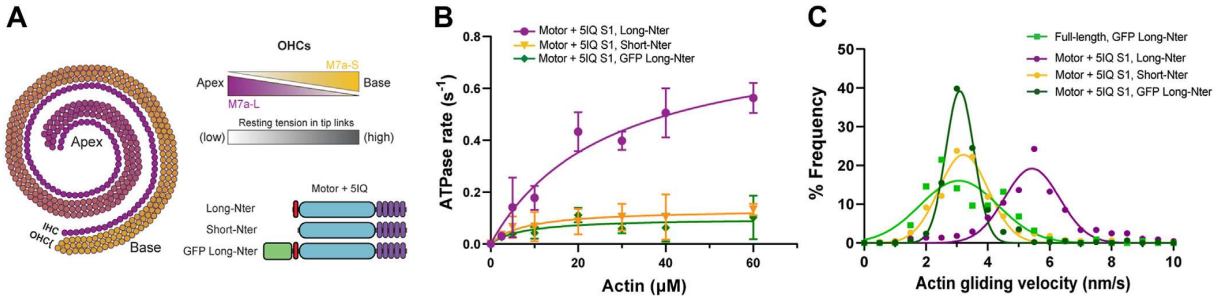

Figure 3. The short N-terminal extension of myosin-7a regulates the myosin enzymatic activity. *A*, graphical illustration of the expression pattern of the two different myosin-7a isoforms in the outer hair cells of the cochlea (11). As the expression of the short isoform increases, so does the tension within the hair cells stereocilia (24). Domain organizations of myosin-7a-5IQ S1 constructs used in the experiments described in *B* and *C*. *B*, steady-state ATPase assay of myosin-7a-5IQ S1 constructs yielding the kinetic parameters: long N-terminal (*purple*) isoform v_{max} = 0.83 ± 0.14 s^{-1}, K_{ATPase} = 27 ± 5 μM; short N-terminal (*yellow*) isoform v_{max} = 0.13 ± 0.06 s^{-1}, K_{ATPase} = 8 ± 1.1 μM; GFP-tagged long N-terminal (*green*) isoform v_{max} = 0.1 ± 0.07 s^{-1}, K_{ATPase} = 8 ± 5.5 μM. Values plotted are mean ± SD from four independent experiments. *C*, *in vitro* motility actin gliding assay of different motor + 5IQ S1 myosin-7a yielding the kinetic parameters: long N-terminal motor + 5IQ S1 (*purple*) isoform v = 5.4 ± 0.9 nm/s; short N-terminal motor + 5IQ S1 (*yellow*) isoform v = 3 ± 0.9 nm/s; GFP-tagged long N-terminal motor + 5IQ S1 (*green*) isoform v = 3.1 ± 0.5 nm/s; GFP-tagged long N-terminal full-length (*light green*) isoform v = 3.1 ± 1.3 nm/s.

Table 2
Steady-state ATPase activity and actin gliding velocity of human myosin-7a-5IQ S1 constructs

Parameter	Long N-terminal	Short N-terminal	GFP-Long N-terminal
v_{max}	0.83 ± 0.14 s^{-1}	0.13 ± 0.06 s^{-1}	0.1 ± 0.07 s^{-1}
K_m	27 ± 5 μM	8 ± 1.1 μM	8 ± 5.8 μM
Actin gliding velocity	5.4 ± 0.9 nm/s	3 ± 0.9 nm/s	3.1 ± 0.5 nm/s

chains (Fig. 4*B*). Using the single-molecule *in vitro* motility assay, where actin filaments bound to the coverslip surface serve as tracks for the motors, we were able to observe the processive movements of individual fluorescently labeled myosin molecules (Fig. 4*C*). In the presence of 150 mM NaCl and ATP, artificially dimerized myosin-7a moved slowly (4.3 ± 1.5 nm/s) along the surface-bound actin filaments (Fig. 4, *D* and *E*), with a characteristic run length of 378 nm (Fig. 4*F*) and duration time of 137 s (Fig. 4*G*).

We next tested binding protein–mediated processivity in human myosin-7a. MyRIP, a known myosin-7a binding partner, has been shown to induce processivity of myosin-7a when the two proteins are cotransfected in cells (25). We expressed and purified mCherry-tagged MyRIP in *Sf*9 cells (Fig. S4). To characterize the motility of the motor–adaptor complex, we performed single-molecule *in vitro* assays using equimolar concentration of purified mCherry-MyRIP preincubated with full-length myosin-7a that had no tag at the N terminus. A GFP tag was fused to RLC to visualize myosin-7a under total internal reflection fluorescence (TIRF) microscopy. We observed processive movement of myosin-7a–MyRIP complex (Fig. 4*H*). Simultaneous two-color imaging reveals that MyRIP and myosin-7a comigrate (Fig. 4*I*). The complex moves slowly on actin filaments (7.8 ± 4.2 nm/s) (Fig. 4*J*), with a characteristic run length of 552 nm (Fig. 4*K*) and average time of attachment of 113 s (Fig. 4*L*).

Discussion

The regulation of myosin-7a has been a focus of research for several years because of its importance in human sensory functions (2, 31). Despite this, many questions remain unanswered because of the challenges in obtaining a high-quality holoenzyme. The present study demonstrates a method for purifying intact human myosin-7a. We show that mammalian myosin-7a has evolved multiple unique regulatory elements, enabling a stringent control of its mechanical function. We propose that this adaptation allows myosin-7a to fulfill its varied roles in cochlear hair cells, such as cargo transport and dynamic gating of mechanoelectrical channels.

The light chain composition and calcium regulation of human myosin-7a

Using the baculovirus/*Sf*9 system, we demonstrate that human myosin-7a copurifies with RLC, CaM, and CALML4. Although copurification does not directly confirm their roles as native light chains, it is worth noting that RLC, CaM, and CALML4 have all been identified in hair cell stereocilia according to previous mass spectrometry (MS) analyses (32, 33). Our results further demonstrate that the first IQ motif of myosin-7a preferentially binds to RLC. This finding is reminiscent of a previous report on myosin-15, another stereociliar MyTH4-FERM myosin, which was also shown to bind RLC at its first IQ motif (17). Earlier studies using purified IQ segments showed that the third IQ motif of myosin-7a does not bind to either CaM or RLC (8). Recently, Choi *et al.* (http://rave.ohiolink.edu/etdc/view?acc_num=toledo1532947508319487) used pull-down experiments to show that CALML4 only associated with the neck region when the third IQ motif was present. Our mass photometry results suggest that in the presence of calcium, while CaM dissociates, myosin-7a maintains its stable association with one RLC and one CALML4. Taken together, we propose a model for the spatial configuration of the light chains along the lever arm: RLC and CALML4 binds to the first and third IQ motifs of myosin-7a, respectively, independent of environmental Ca^{2+} concentrations. The remaining IQs motifs, on the other hand, are able to dynamically interact with CaM in a calcium-dependent manner, potentially serving as regulatory elements that modulate the mechanoactivity of myosin-7a in response to Ca^{2+} signaling (Fig. 2*G*). The third IQ of myosin-7a across a wide range of species (Fig. S5) is somewhat divergent from the classical IQxxxRGxxxR with the glycine and second arginine being absent. How this relates to the specificity of light chain binding is currently unclear, but it should be noted that this divergence likely occurred prior to the emergence of CALML4 in evolution (Fig. S5).

Previous structural studies on the CaM and IQ5-SAH complex show that increased Ca^{2+} concentration causes CaM to orientate toward the N terminus, resulting in a lever arm that is less rigid, as evidenced by increased structural flexibility of the IQ5-SAH segment (20). It was also shown that the Ca^{2+}-bound CaM does not dissociate but instead partially binds to the IQ4 region. The authors propose that the retained Ca^{2+}-bound CaM may play a role in maintaining the lever arm to be partially structured, thereby enabling a quicker restoration of motor function when Ca^{2+} concentrations return to resting levels (20). In line with this, our *in vitro* motility assays demonstrate that elevated Ca^{2+} concentration hampers the motor's ability to move actin filaments, indicating a compromised mechanical function. Intriguingly, we found that the reduced motor function is accompanied by dissociation of CaM. We reason that this observed difference may be due to the fact that our protein contains an intact neck region, which allows detection of light chain dissociation potentially triggered by the translocation. We further propose that the Ca^{2+}-insensitive CALML4 may serve to maintain the lever arm's structural integrity when cellular Ca^{2+} concentration rises. This hypothesis is supported by the observation that in the copurification experiments, the association of CaM with myosin-7a heavy chain is dependent on the presence of CALML4.

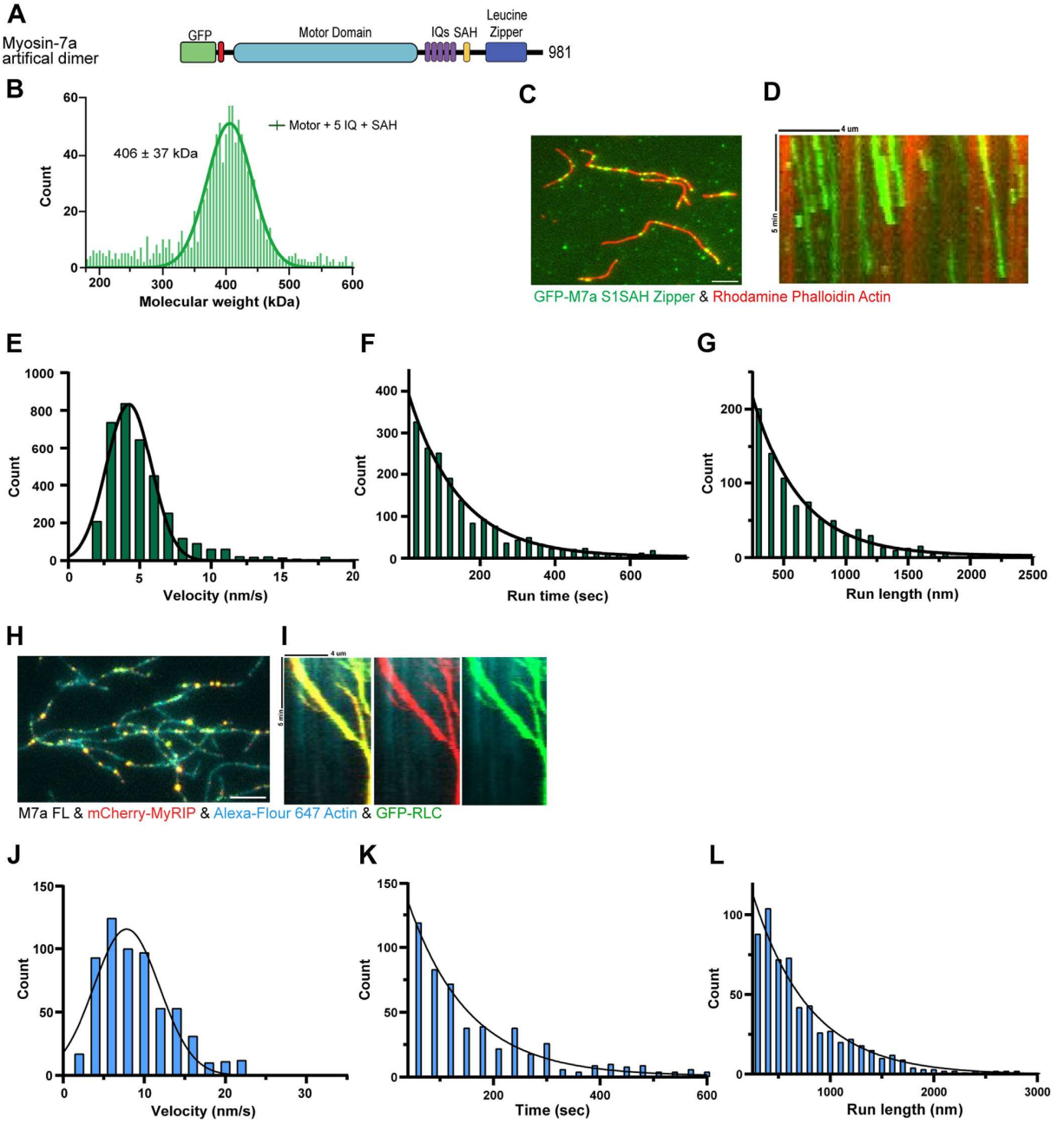

Figure 4. Human myosin-7a is a processive motor when dimerized. *A*, domain organization of human GFP-myosin-7a-S1-SAH-Zipper with an N-terminal GFP moiety. *B*, single-molecule mass photometry assay of GFP-myosin-7a-S1-SAH-Zipper proteins. Histograms show the molecular weights of individual particles with a bin width of 5 kDa. *Lines* are the Gaussian fit to the data yielding the molecular weight of the samples. *C*, a single time frame of GFP-myosin-7a-S1SAH-Zipper on immobilized actin filaments (labeled with rhodamine phalloidin, *red*). Scale bar represents 5 μm. *D*, kymograph analysis showing the processive movements (*diagonal lines*) of GFP-Myosin-7a-S1SAH-Zipper. *E–G*, frequency distribution histograms of the velocity (4.3 ± 1.5 nm/s) (*E*), characteristic run length (378 nm) (*F*), and characteristic run duration (137 s) (*G*), respectively, for the GFP-myosin-7a-S1SAH-Zipper. The *solid line* shows the best fit to a Gaussian or a single exponential equation as appropriate. *H*, a single time frame of myosin-7a-FL and mCherry-MyRIP (*red*) on immobilized actin filaments (labeled with Alexa-Flour 647, *blue*). Myosin-7a is visualized by GFP-RLC. Scale bar represents 5 μm. *I*, kymograph analysis reveals *diagonal lines* of GFP-RLC and mCherry-MyRIP are overlaid. *J–L*, frequency distribution histograms of the velocity (7.8 ± 4.2 nm/s) (*J*), characteristic run length (552 nm) (*K*), and characteristic run duration (113 s) (*L*), respectively, for the myosin-7a-FL. The *solid line* shows the best fit to a Gaussian or a single exponential equation. MyRIP, myosin and Rab interacting protein; RLC, regulatory light chain; SAH, SAH, stable single alpha-helix.

Mechanoregulation of human myosin-7a

Regulation of the mechanoenzymatic activity by the N-terminal extension

Recent studies reveal that mammalian cochlea expresses two myosin-7a splice isoforms, produced by alternative translation starting sites. Analysis of isoform-specific transgenic mouse models suggests that the two isoforms are expressed in opposing gradients along the tonotopic axis in OHCs, with the short variant being dominant at the cochlear base (11). Using purified proteins, we demonstrate that the short isoform possesses significantly slower mechanoenzymatic activity compared with the long isoform, characterized by an approximately eightfold decrease in both steady-state ATPase activity and actin gliding motility. These findings align with recent mechanical studies on hair cells, showing that the resting tension of single tip links also follows the tonotopic gradient, progressively increasing toward the base (24). We speculate that the slow ATP turnover of the short isoform may allow this variant to generate higher tension on the tip links at the base at a lower energy cost. To test this hypothesis, further kinetic studies will be needed to determine the parameters of kinetic intermediates within the actomyosin ATPase cycle of these isoforms. Furthermore, considering that their expression patterns correlate with the gradient of the tip link tension, we propose that OHCs may regulate their mechanosensitivity by adjusting the expression levels of the two myosin-7a isoforms. Examining the effect of mechanical load in optical trapping experiments could test this hypothesis.

N-terminal alternative splicing has been observed in multiple myosin classes as a mechanism to establish kinetic and functional diversity (34–36). Furthermore, it has been demonstrated that N-terminal extension prior to the motor domain can influence myosin motor activity (34, 37). One well-studied example is myosin-1b. Its N-terminal extension was shown to position near the converter-lever arm junction and can impact the myosin's force sensitivity and mechanical output (37–39). The structural basis for the regulation of the N-terminal extension in human myosin-7a is currently unknown. However, our findings suggest that this N-terminal segment plays a crucial role in accelerating the mechanoenzymatic activity of myosin-7a. When a GFP moiety is added prior to the N-terminal extension, the long isoform displayed kinetic and motile behavior similar to that of the short isoform, suggesting a potential disruption of the normal configuration and function of the N-terminal extension. These findings also suggest that caution should be exercised in the use of N-terminal-tagged GFP-myosin-7a in cellular studies. It is worth noting that this N-terminal extension splicing mechanism appears to be specific to mammals and does not exist in the *Drosophila* ortholog. Instead, *Drosophila* myosin-7a incorporates an SH3 domain prior to the motor domain (40), and the presence of an N-terminal tag does not seem to affect its mechanoenzymatic activity (30).

The processive motility of human myosin-7a

Myosin-7a is proposed to participate in cargo transport within hair cell stereocilia, in addition to maintaining the resting tension of the tip link (3, 41). We show that purified intact human myosin-7a is monomeric, adopting an evolutionarily conserved autoinhibited conformation (21). This indicates that for myosin-7a to move processively, dimerization or oligomerization is required. By adding a leucine zipper motif to the end of the lever arm, we demonstrate that dimerized myosin-7a can move processively along actin filaments. It is interesting to note that this construct contains an N-terminal GFP tag, which we show can alter the motor's enzymatic activity into short-isoform like. The observed processive motility indicates that the short isoform may also be able to transport cargoes, albeit slowly. This notion is supported by the observation that in the long-isoform specific knockout mice, the hair bundle morphology developed normally, and the putative myosin-7a cargo proteins remained present in the stereocilia (11).

We further tested the mechanism of binding protein–mediated myosin-7a processivity. We examined MyRIP, a known binding partner for myosin-7a and Rab27a, and that has been shown to activate the myosin *in vivo* (25). We show that MyRIP can bind to human myosin-7a as purified components, and the resulting motor–adaptor complex comigrates along actin filaments. While the exact mechanism of MyRIP-induced processivity is not the main focus of this study, our previous work has extensively characterized its *Drosophila* homolog M7BP and provided detailed mechanistic insights into its role in mediating myosin-7a processivity (Table S1) (30). Together, our results support the notion that human myosin-7a can move processively along actin upon dimerization and potentially serve as a cargo transporter in living cells.

Functional mechanisms of myosin-7a in mammalian cochlea

In summary, this work uncovers several regulatory mechanisms that appear to be unique for mammalian myosin-7a and its roles in the Organ of Corti. Our findings collectively support a model in which myosin-7a localizes to the tip ends of stereocilia through its processive motility and regulates the tip link's tension and hair cell mechanosensitivity. We propose that multiple myosin-7a splicing isoforms, each with distinct mechanoenzymatic properties, are employed to establish characteristic tip-link tension within the cochlear tonotopic map. The successful production of intact human myosin-7a protein provides a valuable tool for future investigations into the molecular details of human vision and hearing loss caused by myosin-7a defects.

Experimental procedures

Cloning and optimization of myosin-7a expression

Full-length human myosin-7a heavy chain (NM_000260.4) with a C-terminal FLAG purification tag, RLC (NM_001144944.1), CaM (NM_001329922.1), and CALML4 (NM_033429.3) sequences were cloned separately into pACEBac1 (Geneva Biotech) vectors. InFusion (TakaraBio) was used to ligate the PCR product and the EcoRI digested vector backbone. The separate gene cassettes were digested with BstXI and I-CeuI and then assembled with a BstXI

digested vector using T4 DNA ligase. *Sf*9 insect cells were coinfected with MultiBac baculovirus containing all four subunits of the myosin-7a holoenzyme and baculovirus expressing both human UNC45B and human HSP90AA1.

Purification of myosin-7a

Myosin-7a-FLAG recombinant protein was expressed in *Sf*9 insect cells, which were previously infected with the recombinant baculoviruses. The cells were centrifuged after 72 h expression, and the pellet was frozen in liquid nitrogen and stored at −80 °C until it was used. Every process of the purification was performed at 4 °C. The frozen pellet was thawed on ice, washed, and homogenized with buffer containing 10 mM MOPS, 500 mM NaCl, 10 mM $MgCl_2$, 1 mM EGTA, 0.3 mM NaN_3, 1 mM DTT, 0.1 mM PMSF, 4 μg/ml leupeptin, 5 mM ATP, Pierce protease inhibitor tablet (ThermoFisher) (pH 7.4). After sonication (with Misonix Xl2020 Ultra Sonic Processor, for 5 min, 5 s impulses with 3 s breaks, 60% amplitude), the cellular debris was removed by ultracentrifugation (48,000*g*, 30 min). Monoclonal anti-FLAG M2 resin (2 ml) (Sigma) was added to the supernatant and incubated for 1 h at 4 °C while shaking. After 1 h of gentle shaking, the resin was loaded into a column. The resin was then washed with 500 mM NaCl, 10 mM MOPS, 0.1 mM EGTA, 3 mM NaN_3, 0.1 mM DTT, 0.1 mM PMSF, 10 mM $MgCl_2$, 5 mM ATP, 4 μg/ml leupeptin (pH 7.4); followed by a washing with 10 mM MOPS, 0.1 mM EGTA, 3 mM NaN_3, 0.1 mM PMSF, 4 μg/ml leupeptin (pH 7.4). Myosin-7a was eluted with a FLAG protein containing buffer (500 mM NaCl, 2.5 mM MOPS, 25 μM EGTA, 0.75 mM NaN_3, 5 mg FLAG peptide [pH 7.4]). About 300 μl fractions was collected, then pooled, and dialyzed against a buffer containing 500 mM NaCl, 2 mM $MgCl_2$, 0.1 mM EGTA, 10 mM MOPS, and 1 mM DTT (pH 7.4).

Purification of other proteins

MyRIP (NM_001284423.2) with a C-terminal FLAG purification was expressed in *Sf*9 insect cells. The protein purification was carried out as described previously. CaM was purified according to previously published protocols (36).

CALML4-His was cloned into pET15b (Addgene, Plasmid #26092) plasmid and then expressed in KRX (Promega) cells. The cells were inoculated into an overnight starter culture and then diluted into 1 liter of LB (KD Medical). The expression was induced with the addition of 1 mM IPTG. The cells were harvested after 10 h expression, and the pellet was frozen in liquid nitrogen and stored at −80 °C until it was used. The frozen pellet was thawed on ice, washed, and homogenized with buffer (2× PBS). After sonication (5 min, 5 s impulses with 3 s breaks, 60% amplitude), the cellular debris was removed by ultracentrifugation (48,000*g*, 1 h). NEBExpress Ni Resin was added to the supernatant and incubated for 1 h at 4 °C while shaking. After 1 h, the resin was loaded into a column and allowed it to sediment. It was washed with a buffer (2× PBS, 5 mM imidazole). CALML4-His was eluted with 500 mM imidazole (in 2× PBS). Tobacco etch virus protease (Sigma) was added (1:100 dilution), and the sample was dialyzed overnight. After overnight dialysis, the sample was loaded into NEBExpress Ni Resin containing column, allowed it to sediment, then collected the flow through, and dialyzed against a buffer containing 500 mM NaCl, 2 mM $MgCl_2$, 0.1 mM EGTA, 10 mM MOPS, and 1 mM DTT (pH 7.4).

GFP-RLC was cloned into pFastBac1 plasmid and expressed in *Sf*9 insect cells. The cells were centrifuged after 72 h expression, and the pellet was frozen in liquid nitrogen and stored at −80 °C until it was used. Every process of the purification was performed at 4 °C. The frozen pellet was thawed on ice, washed, and homogenized with buffer containing 2 M urea, 25 mM Tris–HCl, 0.1 mM PMSF, 1 mM DTT, and 0.001% NaN_3 (pH 7.5). In the rest of this paragraph, we refer to this buffer. The cellular debris was removed by ultracentrifugation (48,000*g*, 1 h). The supernatant was applied to Q-Sepharose column, washed with buffer containing 200 mM NaCl, and eluted with buffer containing 300 mM NaCl. The eluant was diluted fourfold into buffer to reduce the ionic strength and applied to a DEAE–Sepharose column (Sigma). After washing with buffer, protein was eluted using buffer containing a salt gradient from 0 to 300 mM NaCl. The eluant was precipitated using ammonium sulfate in 5% increments, and precipitates were resuspended in PBS, followed by dialysis against PBS (+5 mM DTT). The fractions were assessed by SDS-PAGE, and the purest was applied to a Superdex 200 Increase 10/300 GL column (Sigma). Flow through was collected, then SDS-PAGE was used to assess the purest fractions, and these were drop frozen in liquid nitrogen.

Actin gliding motility assay

Flow chambers were prepared using No. 1.5 glass coverslips and glass slides. The coverslips were covered with 1% nitrocellulose solution in amyl acetate and then fixed on a cleaned slide with double-sided tape. Full-length myosin-7a was bound to the coverslip in low salt conditions (∼0.2 mg/ml myosin in 150 mM NaCl, 20 mM MOPS, 5 mM $MgCl_2$, 0.1 mM EGTA, pH 7.4). After thorough washing steps, rhodamine–phalloidin-labeled actin (20 nM) was flushed in the chamber. The actin motility was observed in the final assay buffer (150 mM NaCl, 20 mM MOPS, 5 mM $MgCl_2$, 0.1 mM EGTA, 50 mM DTT, 5 mM ATP, 2.5 mg/ml glucose, 100 μg/ml glucose oxidase, 2 μM GFP-RLC, 2 μM CaM, 2 μM CALML4, and 100 μM $CaCl_2$). Movies were collected on an inverted Nikon Eclipse Ti-E microscope with an H-TIRF module attachment, a CFI60 Apochromat TIRF 100× Oil Immersion Objective Lens (numerical aperture = 1.49, working distance = 0.12 mm), and an EMCCD camera (Andor iXon Ultra 888 EMCCD, 1024 × 1024 array, 13 μm pixel). The excitation light source was a Nikon LU-N4 Laser Unit equipped with four lasers (405, 488, 561, and 640 nm). Where required, movies were drift corrected using the ImageJ/FIJI plugin image stabilizer. Actin filament centroid positions were determined using a FIJI macro based on the ridge detector plugin. Detected centroid positions were converted to a new image with a circle representing each centroid, and the movement of these circles was then analyzed using the TrackMate plugin for ImageJ. TrackMate settings

were LoG detector (estimated blob diameter = 1 μm, threshold = not set), initial threshold = not set, view = HyperStack Displayer, filters on spots = not set, tracker = simple LAP tracker (linking maximum distance = 0.2 μm, gap-closing maximum distance = 0.2 μm, gap-closing maximum frame gap = 2), and filters on tracks: number of spots in track (above 5). Raw data were obtained from the analysis tab of the TrackMate plugin and imported into Prism 7 (GraphPad Software, Inc) for analysis. Track mean line speed was used as the output velocity. Gaussian fits of the velocity histograms were used to determine average velocity ($Y = Amplitude \times e^{(-0.5\times(X-mean/SD)^2)}$).

Single-molecule motility assay

Flow chambers were prepared using No. 1.5 glass coverslips and glass slides. The coverslips were repeatedly washed with 100% ethanol and distilled water and then thoroughly dried with a stream of filtered air and plasma cleaned (by Diener-Zepto Plasma Cleaner) for 3 min in argon (90%/ power). Biotin–PEG mixture (Laysan Bio) was added to the surface of the coverslip. After a 20 min incubation at 70 °C, the coverslips were rinsed thoroughly with distilled water and then fixed on a cleaned slide with double-sided tape. Biotin–phalloidin (ThermoFisher) actin (200 nM) was bound to the surface of the coverslip *via* NeutrAvidin (Fisher Scientific; 2 mg/ml). Myosin (∼0.01 mg/ml in 150 mM NaCl, 20 mM MOPS, 5 mM $MgCl_2$, 0.1 mM EGTA, [pH 7.4]) was added. The motility was observed in the final assay buffer (150 mM NaCl, 20 mM MOPS, 5 mM $MgCl_2$, 0.1 mM EGTA, 50 mM DTT, 5 mM ATP, 2.5 mg/ml glucose, 100 μg/ml glucose oxidase, 2 μM GFP-RLC, 2 μM CaM, and 2 μM CALML4).

Movies were collected as mentioned before. Where required, movies were drift corrected using the ImageJ/FIJI plugin Image Stabilizer. Processive runs were analyzed using the TrackMate plugin for ImageJ. TrackMate settings were LoG detector (estimated blob diameter = 0.5–0.7 μm, threshold = 40–100), initial threshold = not set, view = HyperStack Displayer, filters on spots = not set, tracker = simple LAP tracker (linking maximum distance = 0.2 μm, gap-closing maximum distance = 0.2 μm, gap-closing maximum frame gap = 2), filters on tracks: duration of track (above 30 s), and track displacement (above 0.4 μm). Raw data were obtained from the analysis tab of the TrackMate plugin and imported into Prism 7 for analysis. Track mean line speed was used as the output velocity. Gaussian fits of the velocity histograms were used to determine average velocity. Characteristic run lengths and run durations were determined *via* exponential fits of the corresponding histograms ($Y = (Y_0 - Plateau)\times e^{(-K\times X)} + Plateau$).

Single-molecule mass photometry

Mass photometry is a novel bioanalytical tool that allows us to measure the molecular mass of individual biomolecules (42, 43). Refeyn One MP mass photometer was used to acquire single-molecule landing data. Microscope slides were cleaned consecutively with water, ethanol, and isopropanol and then dried using a clean stream of nitrogen. A silicone gasket was cleaned with water, dried using a clean stream of nitrogen, and then positioned on a cleaned microscope slide. About 20 nM of each sample or mixture was loaded into a single gasket. Data were collected for 1 min. All measurements were carried out at room temperature (∼24 °C). Images were processed using manufacturer supplied software (Refeyn). The conversion between molecular mass and contrast was calibrated with protein standards of known molecular weight by manufacturer supplied software (Refeyn) as it was described earlier (44). For each sample, a histogram of mass distribution was plotted and fitted with a Gaussian fit.

Steady-state ATPase assay

Steady-state ATPase activities were measured in SpectraMax ID3 microplate reader (Molecular Devices, Inc) at 37 °C in buffers containing 10 mM MOPS, 1 mM ATP, 50 mM NaCl, 2 mM $MgCl_2$, 0.1 mM EGTA (pH 7.2). Data were collected with Softmax Pro 7.1 software (Molecular Devices) and plotted by Graphpad Prism 7.0. The buffers also contained an NADH-coupled ATP-regenerating system including 40 units/ml lactate dehydrogenase, 200 units/ml pyruvate kinase, 200 μM NADH, and 1 mM phosphoenolpyruvate. The rate of ATP hydrolysis was measured from the decrease in absorbance at 340 nm caused by the oxidation of NADH and calculated based on Michaelis–Menten kinetics ($Y = v_{max}\times X/(K_M + X)$).

MS

This MS analysis was done by Poochon Scientific. Samples were processed for trypsin/lys-C digestion followed by LC/MS/MS analysis. The MS raw file was analyzed using Proteome Discoverer 2.5 (Thermo Fisher Scientific) against human protein sequences database and host *Sf*9 protein sequences database.

Electrophoretic mobility shift assay

Ca^{2+}-dependent electrophoretic shift assay was performed using the method described previously (45) with some modifications. Purified CaM (1 μM) and CALML4 (1 μM) were incubated at room temperature for 20 min in the presence of 5 μM $CaCl_2$ or 1 μM EGTA. The samples were then subjected to 16% SDS-PAGE, which was run with a constant current of 30 mA in Tris–glycine buffer for 2 h at room temperature.

Immunoblotting and antibodies

SDS-PAGE was used for protein separation followed by the semidry transferring to nitrocellulose membrane (Bio-Rad). After transferring, the membrane was blocked using LI-COR Blocking Buffer for an hour at room temperature. The primary antibody (anti-CALML4: 1:5000 dilution; ProteinTech, catalog no.: 15894 1 AP; anti-M7a: 1:1000 dilution; Santa Cruz Biotechnology, catalog no.: Sc-74516; and anti-UNC45B: 1:500 dilution, Invitrogen, catalog no.: PA5 114191) was incubated overnight at 4 °C. After thorough washing with PBS, the secondary antibody (antimouse: 1:10,000 dilution, LI-COR, catalog no.: D10901 11; anti-rabbit: 1:10,000 dilution, LI-COR,

catalog no.: D11103 01) was incubated at room temperature for an hour. Imaging was done with Azure 600 (Azure Biosystems).

Negative-stain electron microscopy and image processing

Proteins were diluted in buffer containing 150 mM NaCl (500 mM NaCl was stated in the text), 10 mM MOPS, 2 mM $MgCl_2$, and 0.1 mM EGTA. Dilution buffer for myosin also contained 100 μM ATP (pH 7.0). Samples were applied to UV-treated and carbon-coated EM grids and stained immediately using 1% uranyl acetate. Micrographs were recorded on a JEOL 1200EX microscope using an AMT XR-60 CCD camera at a nominal magnification of 60,000×. Reference-free image alignments and K-means classification were conducted using SPIDER software (developed by Wadsworth Center, Albany, NY).

MST

MST measurements were carried out using a Monolith NT.115 instrument. CALML4-His and CaM-His (MilliporeSigma) were labeled with RED-Tris–NTA dye (Nanotemper) according to the manufacturer's instructions. A solution of 100 nM CALML4 or CaM was combined with 2 μM Ca^{2+} to perform a binding check. A calcium dilution series (5 mM–150 nM) combined with 100 nM CaM was performed using 16 capillaries. Measurements were carried out in buffer containing 20 mM HEPES (pH 7.4) and 0.02% Tween-20 using Monolith capillaries (Nanotemper). The MST laser power was set to 60%. Analysis of MST traces was completed using MO.Affinity Analysis software (Nanotemper) (46).

Data availability

All data are contained within the article and supporting information.

Supporting information—This article contains supporting information (30, 47).

Acknowledgments—We thank the Electron Microscopy and Biophysics Core Facilities of the National Heart, Lung and Blood Institute (NHLBI, National Institutes of Health) for their support and the use of facilities. We thank Fang Zhang for the help with reagent and actin preparation. We thank the Microscopy Imaging Facility and Visual Function and Morphology Core at West Virginia University for help with image analysis.

Author contributions—J. R. S. and R. L. conceptualization; A. H. and R. L. methodology; N. B. software; A. H. and N. B. formal analysis; A. H. investigation; A. H. writing–original draft; N. B., Y. T., A. K., J. R. S., and R. L. writing–review & editing; J. R. S. and R. L. supervision.

Funding and additional information—R. L. is a recipient of a postdoctoral fellowship from NHLBI (Lenfant Biomedical Fellowship) and the tenure-track startup funds from West Virginia University. R.L. and N.B. are supported by National Institute of General Medical Sciences (NIGMS) Visual Sciences Center of Biomedical Reserach Excellence (Vs-CoBRE) (P20GM144230). This work is also supported by the Intramural Research Program of the NHLBI (grant no.: HL004232; to J. R. S.). The content is solely the responsibility of the authors and does not necessarily represent the official views of the National Institutes of Health.

Conflict of interest—The authors declare that they have no conflicts of interest with the contents of this article.

Abbreviations—The abbreviations used are: CaM, calmodulin; CALML4, calmodulin-like protein 4; ELC, essential light chain; M7a-S1, myosin-7a subfragment-1; MS, mass spectrometry; MST, microscale thermophoresis; MyRIP, myosin and Rab interacting protein; NHLBI, National Heart, Lung and Blood Institute; OHC, outer hair cell; RLC, regulatory light chain; SAH, stable single alpha-helix; TIRF, total internal reflection fluorescence.

References

1. Berg, J. S., Powell, B. C., and Cheney, R. E. (2001) A millennial myosin census. *Mol. Biol. Cell* **12**, 780–794
2. Mathur, P., and Yang, J. (2015) Usher Syndrome: hearing loss, retinal degeneration and associated abnormalities. *Biochim. Biophys. Acta* **1852**, 406–420
3. Moreland, Z. G., and Bird, J. E. (2022) Myosin motors in sensory hair bundle assembly. *Curr. Opin. Cell Biol.* **79**, 102132
4. Matoo, S., Graves, M. J., Acharya, P., Choi, M. S., Storad, Z. A., Idris, R., *et al.* (2021) Comparative analysis of the MyTH4-FERM myosins reveals insights into the determinants of actin track selection in polarized epithelia. *Mol. Biol. Cell* **32**, ar30
5. Chen, Z.-Y., Hasson, T., Kelley, P. M., Schwender, B. J., Schwartz, M. F., Ramakrishnan, M., Kimberling, W. J., Mooseker, M. S., and Corey, D. P. (1996) Molecular cloning and domain structure of human myosin-VIIa, the gene product defective in Usher syndrome 1B. *Genomics* **36**, 440–448
6. Heissler, S. M., and Sellers, J. R. (2014) Myosin light chains: teaching old dogs new tricks. *Bioarchitecture* **4**, 169–188
7. Haithcock, J., Billington, N., Choi, K., Fordham, J., Sellers, J. R., Stafford, W. F., *et al.* (2011) The kinetic mechanism of mouse myosin VIIA. *J. Biol. Chem.* **286**, 8819–8828
8. Sakai, T., Jung, H. S., Sato, O., Yamada, M. D., You, D. J., Ikebe, R., *et al.* (2015) Structure and regulation of the movement of human myosin VIIA. *J. Biol. Chem.* **290**, 17587–17598
9. Choi, M. S., Graves, M. J., Matoo, S., Storad, Z. A., El Sheikh Idris, R. A., Weck, M. L., *et al.* (2020) The small EF-hand protein CALML4 functions as a critical myosin light chain within the intermicrovillar adhesion complex. *J. Biol. Chem.* **295**, 9281–9296
10. Kapustina, M., and Cheney, R. E. (2020) A new light chain for myosin-7. *J. Biol. Chem.* **295**, 9297–9298
11. Li, S., Mecca, A., Kim, J., Caprara, G. A., Wagner, E. L., Du, T. T., *et al.* (2020) Myosin-VIIa is expressed in multiple isoforms and essential for tensioning the hair cell mechanotransduction complex. *Nat. Commun.* **11**, 2066
12. Peckham, M., and Knight, P. J. (2009) When a predicted coiled coil is really a single α-helix, in myosins and other proteins. *Soft Matter* **5**, 2493–2503
13. Klomp, A. E., Teofilo, K., Legacki, E., and Williams, D. S. (2007) Analysis of the linkage of MYRIP and MYO7A to melanosomes by RAB27A in retinal pigment epithelial cells. *Cell Motil. Cytoskeleton* **64**, 474–487
14. Kuroda, T. S., and Fukuda, M. (2005) Functional analysis of Slac2-c/MyRIP as a linker protein between melanosomes and myosin VIIa. *J. Biol. Chem.* **280**, 28015–28022
15. Morgan, C. P., Krey, J. F., Grati, M., Zhao, B., Fallen, S., Kannan-Sundhari, A., *et al.* (2016) PDZD7-MYO7A complex identified in enriched stereocilia membranes. *Elife* **5**, e18312
16. Ahmed, Z. M., Riazuddin, S., Khan, S. N., Friedman, P. L., Riazuddin, S., and Friedman, T. B. (2009) USH1H, a novel locus for type I Usher syndrome, maps to chromosome 15q22-23. *Clin. Genet.* **75**, 86–91

17. Bird, J. E., Takagi, Y., Billington, N., Strub, M. P., Sellers, J. R., and Friedman, T. B. (2014) Chaperone-enhanced purification of unconventional myosin 15, a molecular motor specialized for stereocilia protein trafficking. *Proc. Natl. Acad. Sci. U. S. A.* **111**, 12390–12395
18. Jiang, F., Takagi, Y., Shams, A., Heissler, S. M., Friedman, T. B., Sellers, J. R., *et al.* (2021) The ATPase mechanism of myosin 15, the molecular motor mutated in DFNB3 human deafness. *J. Biol. Chem.* **296**, 100243
19. Sari, D., Gupta, K., Thimiri Govinda Raj, D. B., Aubert, A., Drncova, P., Garzoni, F., *et al.* (2016) The MultiBac baculovirus/insect cell expression vector system for producing complex protein Biologics. *Adv. Exp. Med. Biol.* **896**, 199–215
20. Li, J., Chen, Y., Deng, Y., Unarta, I. C., Lu, Q., Huang, X., *et al.* (2017) Ca(2+)-Induced rigidity change of the myosin VIIa IQ motif-single alpha helix lever arm extension. *Structure* **25**, 579–591.e574
21. Yang, Y., Baboolal, T. G., Siththanandan, V., Chen, M., Walker, M. L., Knight, P. J., *et al.* (2009) A FERM domain autoregulates Drosophila myosin 7a activity. *Proc. Natl. Acad. Sci. U. S. A.* **106**, 4189–4194
22. Rhyner, J. A., Koller, M., Durussel-Gerber, I., Cox, J. A., and Strehler, E. E. (1992) Characterization of the human calmodulin-like protein expressed in Escherichia coli. *Biochemistry* **31**, 12826–12832
23. Chinpongpanich, A., Wutipraditkul, N., Thairat, S., and Buaboocha, T. (2011) Biophysical characterization of calmodulin and calmodulin-like proteins from rice, Oryza sativa L. *Acta Biochim. Biophys. Sin. (Shanghai)* **43**, 867–876
24. Tobin, M., Chaiyasitdhi, A., Michel, V., Michalski, N., and Martin, P. (2019) Stiffness and tension gradients of the hair cell's tip-link complex in the mammalian cochlea. *Elife* **8**, e43473
25. Sakai, T., Umeki, N., Ikebe, R., and Ikebe, M. (2011) Cargo binding activates myosin VIIA motor function in cells. *Proc. Natl. Acad. Sci. U. S. A.* **108**, 7028–7033
26. Senften, M., Schwander, M., Kazmierczak, P., Lillo, C., Shin, J. B., Hasson, T., *et al.* (2006) Physical and functional interaction between protocadherin 15 and myosin VIIa in mechanosensory hair cells. *J. Neurosci.* **26**, 2060–2071
27. Grati, M., and Kachar, B. (2011) Myosin VIIa and sans localization at stereocilia upper tip-link density implicates these Usher syndrome proteins in mechanotransduction. *Proc. Natl. Acad. Sci. U. S. A.* **108**, 11476–11481
28. Heissler, S. M., and Manstein, D. J. (2012) Functional characterization of the human myosin-7a motor domain. *Cell. Mol. Life Sci.* **69**, 299–311
29. Toyoshima, Y. Y., Kron, S. J., McNally, E. M., Niebling, K. R., Toyoshima, C., and Spudich, J. A. (1987) Myosin subfragment-1 is sufficient to move actin filaments *in vitro*. *Nature* **328**, 536–539
30. Liu, R., Billington, N., Yang, Y., Bond, C., Hong, A., Siththanandan, V., *et al.* (2021) A binding protein regulates myosin-7a dimerization and actin bundle assembly. *Nat. Commun.* **12**, 563
31. Whatley, M., Francis, A., Ng, Z. Y., Khoh, X. E., Atlas, M. D., Dilley, R. J., *et al.* (2020) Usher syndrome: genetics and molecular links of hearing loss and directions for therapy. *Front. Genet.* **11**, 565216
32. Shin, J. B., Krey, J. F., Hassan, A., Metlagel, Z., Tauscher, A. N., Pagana, J. M., *et al.* (2013) Molecular architecture of the chick vestibular hair bundle. *Nat. Neurosci.* **16**, 365–374
33. Ebrahim, S., Avenarius, M. R., Grati, M., Krey, J. F., Windsor, A. M., Sousa, A. D., *et al.* (2016) Stereocilia-staircase spacing is influenced by myosin III motors and their cargos espin-1 and espin-like. *Nat. Commun.* **7**, 10833
34. Fujita-Becker, S., Tsiavaliaris, G., Ohkura, R., Shimada, T., Manstein, D. J., and Sutoh, K. (2006) Functional characterization of the N-terminal region of myosin-2. *J. Biol. Chem.* **281**, 36102–36109
35. Mansfield, G. S., Al-Shirawi, D. Y., Ketchum, A. S., Newbern, C. E., and Kiehart, D. P. (1996) Molecular organization and alternative splicing inzipper, the gene that encodes theDrosophilaNon-muscle myosin II heavy chain. *J. Mol. Biol.* **255**, 98–109
36. Guzik-Lendrum, S., Heissler, S. M., Billington, N., Takagi, Y., Yang, Y., Knight, P. J., *et al.* (2013) Mammalian myosin-18A, a highly divergent myosin. *J. Biol. Chem.* **288**, 9532–9548
37. Greenberg, M. J., Lin, T., Shuman, H., and Ostap, E. M. (2015) Mechanochemical tuning of myosin-I by the N-terminal region. *Proc. Natl. Acad. Sci. U. S. A.* **112**, E3337–E3344
38. Shuman, H., Greenberg, M. J., Zwolak, A., Lin, T., Sindelar, C. V., Dominguez, R., *et al.* (2014) A vertebrate myosin-I structure reveals unique insights into myosin mechanochemical tuning. *Proc. Natl. Acad. Sci. U. S. A.* **111**, 2116–2121
39. Mentes, A., Huehn, A., Liu, X., Zwolak, A., Dominguez, R., Shuman, H., *et al.* (2018) High-resolution cryo-EM structures of actin-bound myosin states reveal the mechanism of myosin force sensing. *Proc. Natl. Acad. Sci. U. S. A.* **115**, 1292–1297
40. Kiehart, D. P., Franke, J. D., Chee, M. K., Montague, R. A., Chen, T. L., Roote, J., *et al.* (2004) Drosophila crinkled, mutations of which disrupt morphogenesis and cause lethality, encodes fly myosin VIIA. *Genetics* **168**, 1337–1352
41. Houdusse, A., and Titus, M. A. (2021) The many roles of myosins in filopodia, microvilli and stereocilia. *Curr. Biol.* **31**, R586–R602
42. Young, G., Hundt, N., Cole, D., Fineberg, A., Andrecka, J., Tyler, A., *et al.* (2018) Quantitative mass imaging of single biological macromolecules. *Science* **360**, 423–427
43. Wu, D., and Piszczek, G. (2020) Measuring the affinity of protein-protein interactions on a single-molecule level by mass photometry. *Anal. Biochem.* **592**, 113575
44. Wu, D., and Piszczek, G. (2021) Standard protocol for mass photometry experiments. *Eur. Biophys. J.* **50**, 403–409
45. Burgess, W. H., Jemiolo, D. K., and Kretsinger, R. H. (1980) Interaction of calcium and calmodulin in the presence of sodium dodecyl sulfate. *Biochim. Biophys. Acta* **623**, 257–270
46. Jerabek-Willemsen, M., André, T., Wanner, R., Roth, H. M., Duhr, S., Baaske, P., *et al.* (2014) MicroScale Thermophoresis: interaction analysis and beyond. *J. Mol. Struct.* **1077**, 101–113
47. Sato, O., Komatsu, S., Sakai, T., Tsukasaki, Y., Tanaka, R., Mizutani, T., *et al.* (2017) Human myosin VIIa is a very slow processive motor protein on various cellular actin structures. *J. Biol. Chem.* **292**, 10950–10960